Analysis of the first data taken with the CMS–TOTEM Precision Proton Spectrometer (CT–PPS)

Ksenia Shchelina

A Dissertation
Presented to the Physics Faculty
of the Torino University
in Candidacy for the Degree
of Doctor of Philosophy

Adviser: prof. Michele Arneodo

January 2019

Abstract

The CMS-TOTEM Precision Proton Spectrometer (CT–PPS) started operations in 2016. CT–PPS measures forward scattered protons at the LHC. This thesis documents the analysis of the first 47 fb^{-1} of data collected with CT–PPS. The process $pp \to p\ell^+\ell^-p^{(*)}$, with $\ell^+\ell^-$ a muon or an electron pair produced at midrapidity with mass larger than 110 GeV, is observed for the first time at the LHC in pp collisions at $\sqrt{s} = 13$ TeV. One of the two scattered protons is measured in CT–PPS. The second proton either remains intact or is excited and then dissociates into a low-mass state p^*, which is undetected. The process is used to validate the alignment, the calibration and the general functioning of the spectrometer. The results demonstrate that CT–PPS performs according to the design specifications. In addition, the feasibility of measuring the reaction $pp \to pW^+W^-p$ with CT–PPS in the LHC Run 3 is discussed. An improvement by several orders of magnitude of the existing limits on the anomalous quartic gauge coupling parameter a_0^W/Λ^2 can be achieved.

Acknowledgements

The present study is a tribute to the hard work and profound competence of many people from both the CMS and TOTEM Collaborations – without them CT–PPS would not have been possible. I would like to thank all my CT–PPS colleagues for their help and feedback at various stages of my work, as well as for the friendly and stimulating environment.

I am deeply grateful to Michele Arneodo, my supervisor, who guided me during all these years with incredible dedication, wisdom and trust. Michele created the best possible atmosphere for my work and motivation. His comments greatly helped to improve the clarity of the manuscript.

I am happy to express my gratitude to Jonathan J. Hollar, for the joy of sharing the work on the CT–PPS analysis and the brainstorming sessions ever since I moved to CERN. I have learned an enormous amount of physics and analysis techniques through our discussions: it has been a pleasure to work together.

Fabrizio Ferro, Laurent Forthomme, Diego Figueiredo, Frici Nemes and Nicola Turini taught me many aspects of the CT–PPS software, hardware and reconstruction, and made me feel welcome at CERN. I express my sincere gratitude to them.

I would like to thank Roberta Arcidiacono and Fabrizio Ferro for taking the time to critically read the manuscript and providing valuable comments. I am also grateful to Margherita Obertino for accepting to participate to the PhD committee.

Robert Ciesielski supervised my Master's studies at Moscow State University before I moved to Italy to work on my PhD. The way Robert trained me at the very beginning of my involvement in CMS, along with his enthusiasm, helped me make my first steps. Thank you Robert.

Sasha Proskuryakov (1954–2014) introduced me to the world of experimental particle physics. This thesis is dedicated to his memory.

Contents

List of Tables

List of Figures

Chapter 1

Introduction

Tagging protons scattered at very small angles in collider experiments is challenging. The first reason is machine safety: detectors have to approach the beam at a very small distance without affecting machine operation. The possible complications include magnet quenches, beam losses, showers and detector overheating. At the same time, detectors must be able to sustain high radiation doses. In addition, the reconstruction of the tracks requires complete and precise knowledge of the machine parameters, notably the magnetic field traversed by the scattered protons from the interaction point all the way to the detectors, and the apertures of all the beamline elements.

Over the past decades, experiments at ISR [1, 2], the SPS [3], HERA [4, 5], the TEVATRON [6, 7] and RHIC [8] operated forward proton taggers with low-intensity beams. Information on the scattered protons contributed to the development of diffractive physics, leading to important results on the proton structure, the discovery of hard diffraction, and helping the theoretical understanding of exclusive reactions. The CMS-TOTEM Precision Proton Spectrometer (CT–PPS) [9] (along with the AFP project [10] of ATLAS) starts the next generation of forward proton taggers. For the first time, a forward proton spectrometer is designed and built to operate at high luminosity.

CT–PPS opens a new window on the study of central exclusive production (CEP), $p + p \rightarrow p \oplus \mathrm{X} \oplus p$, where $\oplus$ indicates "rapidity gaps" (regions devoid of final state particles) adjacent to the state X. The state X, which may be a particle or a more complex object, is measured in the CMS central detector and the scattered protons, which carry a large fraction of the incoming proton momentum, are detected in CT–PPS. This allows complete closure of the event kinematics. CEP events provide a unique method to access a variety of topics, such as new physics via anomalous production of W and Z boson pairs, high transverse momentum (p_T) jet production, and possibly the production of new resonances. These studies can be carried out in particularly clean experimental conditions thanks to the absence of proton remnants. The detection of the two final state protons, scattered at almost zero degrees, in very forward near-beam detectors, provides a striking signature. The measurement of the leading protons allows to fully determine the kinematics of the central system. Well defined final states in the CMS central detector matching the protons kinematics can then be selected and precisely reconstructed.

The exclusive two-photon production of pairs of photons, W and Z bosons provides a novel and unique testing ground for the electroweak gauge boson sector. The virtualities of the exchanged photons are on average very small, which makes the LHC a quasi-real photon collider with center-of-mass energy approaching 1 TeV — a region so far unexplored. The detection of $\gamma\gamma \rightarrow W^+W^-$ events allows to measure the quartic gauge coupling $WW\gamma\gamma$, with better sensitivity to anomalous quartic gauge couplings than at LEP [11–18] and TEVATRON [19].

CT–PPS is also potentially instrumental in understanding the Quantum Chromodynamics (QCD) mechanisms involved in CEP. Exclusive di-jet production with $M(jj)$ up to about 700-800 GeV allows the study of pure gluon jet samples with small contamination of quark jets and the investigation of the generalized/skewed parton distributions of the proton.

1.1 Two-photon collisions

As mentioned above, the LHC is also a photon-photon collider, in which the photons are emitted from the incoming protons. The luminosity is lower than that of an e^+e^- collider but the energy range is unique, $\sqrt{s_{\gamma\gamma}}$ up to about 1 TeV, higher than that of the International Linear Collider (ILC) [20]. The photon energies are measured by CT–PPS via the momentum loss of the scattered protons, so $\sqrt{s_{\gamma\gamma}}$ is known on an event-by-event basis with resolution of order 10 GeV.

In the high mass region accessible to CT–PPS with both protons detected, the most relevant final states are $X = e^+e^-$, $\mu^+\mu^-$, and W^+W^- (Fig. 1.1). Hadronic final states from $\gamma\gamma \to q\bar{q}$ are not visible because of the very large backgrounds from $gg \to hadrons$. In the case of the dilepton final states, these backgrounds are not present. The main background is from other events in the same bunch-crossing (pile-up), with protons in CT–PPS unrelated to the central system X. These can be largely suppressed by matching the kinematics of X as measured in the central CMS apparatus and that from the forward protons, and by requiring small charged multiplicity associated to the dilepton vertex.

At large $\sqrt{s_{\gamma\gamma}}$, the two-photon process $\gamma\gamma \to W^+W^-$ has a higher cross section than $\gamma\gamma \to l^+l^-$. This provides a window on physics beyond the Standard Model, since it is sensitive to triple and quartic gauge boson couplings [21]. CT–PPS is expected to improve the limits by at least two orders of magnitude, or perhaps observe a deviation from the SM prediction, as the measurement of the protons provides kinematic constraints and reduces significantly the backgrounds.

Exclusive $\gamma\gamma \to ZZ$ and $\gamma\gamma \to \gamma\gamma$ provide unique measurements of quartic gauge couplings with only neutral particles [22, 23]. The $\gamma\gamma \to ZZ$ and $\gamma\gamma \to \gamma\gamma$ processes are only allowed through loops in the SM resulting in ab-range cross sections within the CT–PPS mass acceptance, so even a few observed events may indicate a new physics discovery.

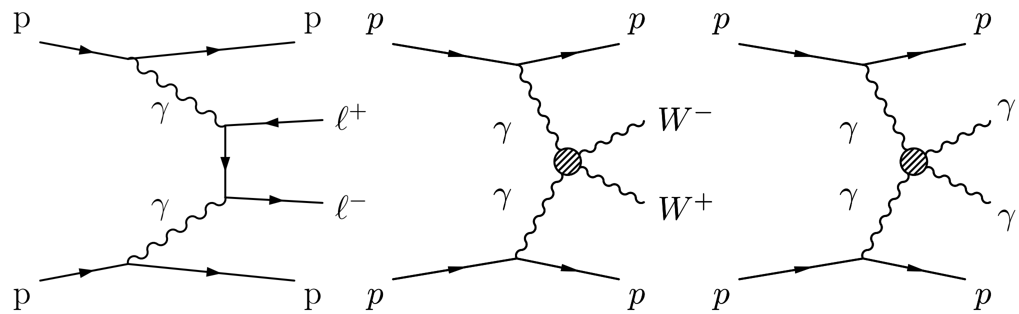

Figure 1.1: Central exclusive production of lepton pairs (left), W boson pairs (middle) and photon pairs (right) in pp collisions.

1.2 Tests of QCD

Normally, in gluon-guon interactions the color exchange results in multi-hadron production. However in multi-jet (two-, three-, or four-jet) exclusive production (Fig. 1.2), a third gluon of opposite color is exchanged and a color string does not form. This may result in one or more rapidity gaps unless other soft parton-parton interactions occur. The probability that this does not happen and the gap is preserved is called the "rapidity gap survival probability" S^2. The overall suppression relative to inclusive jj production is about 10^{-5} for $M(X)$ about 350 GeV. In low-Q^2 interactions, including elastic scattering and diffractive excitation, this color-singlet gluon pair is the leading order description of the Pomeron.

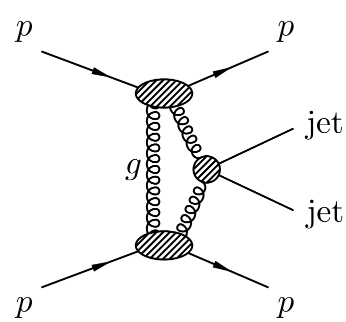

Figure 1.2: Central exclusive dijet production in pp collisions.

CEP of high-E_T jets will shed light on a number of aspects of the proton structure and the strong interaction. On the one hand, the two-gluon proton vertex measures the (skewed) unintegrated gluon parton distribution function of the proton, in a region never explored before. On the other hand, the experimental investigation of the rapidity gap survival probability opens up a new window on the study of soft multiple parton interactions.

Finally, to a very good approximation, the final state obeys a $J_Z = 0$, C-even, P-even selection rule [24]. Here J_Z is the projection of the total angular momentum along the proton beam axis. This selection rule readily permits a clean determination of the quantum numbers of any new resonance. In other words, if a new state were to be produced in CEP, not only could its mass be determined precisely from the scattered protons momenta, independent of the decay mode, but also its J^{PC} numbers would immediately be known.

1.3 Structure of this thesis

CT–PPS was successfully commissioned in 2015 and started data taking in standard LHC runs in 2016. This thesis documents the analysis of the data collected over the course of 2016 and 2017. The analysis had two main goals: first, that of making sure that all detector components operate correctly and that the reconstruction of the proton kinematics is correct. Beyond this, the analysis led to the first observation of (semi)exclusive $\gamma\gamma$ collisions at the electroweak scale.

Two datasets are studied; the first was collected in 2016, right after the commissioning phase. The results of this analysis led to a CMS–TOTEM paper [25]. The second was collected over the course of 2017, after a major upgrade of the CT–PPS tracking system.

Furthermore, a study is presented of the feasibility to measure exclusive W^+W^- events to search for anomalous quartic gauge couplings in the LHC Run 3 (foreseen in 2021-2023).

This thesis is organized as follows:

- Chapter 2 gives a description of CMS and CT–PPS, including an overview of the detector electronics and the data acquisition system of CT–PPS.

- The proton reconstruction techniques are discussed in Chapter 3, along with the details of the optics and alignment corrections.

- The analysis of the first CT–PPS data taken in 2016 on dilepton production is the subject of Chapter 4.

- The results on dilepton production with the 2017 dataset are presented in Chapter 5.

- Finally, the feasibility of measuring exclusive W^+W^- production in the fully hadronic channel with CT–PPS is discussed in Chapter 6.

Chapter 2

The CMS detector and CT-PPS

2.1 The CMS detector

2.1.1 Introduction

The Compact Muon Solenoid (CMS) is a general-purpose particle physics detector operating at the Large Hadron Collider (LHC) at CERN. It was conceived to study proton-proton (and lead-lead) collisions at a center of mass energy up to 14 TeV (5.5 TeV nucleon-nucleon) and at luminosities up to 10^{34} cm^{-2}s^{-1} (10^{27} cm^{-2}s^{-1}) [26].

The CMS detector is comprised of a silicon tracking system, an electromagnetic and a hadronic calorimeter, and a muon system, designed to measure the energy and momentum of collision products. A superconducting solenoid magnet provides a magnetic field of 3.8 T over the full volume of the tracker. The CMS detector is 22 m long and has a diameter of 15 m. Figure 2.1 presents a schematic view of the detector.

CMS is complemented by a forward proton spectrometer, the CMS-TOTEM Precision Proton Spectrometer, described later in the chapter.

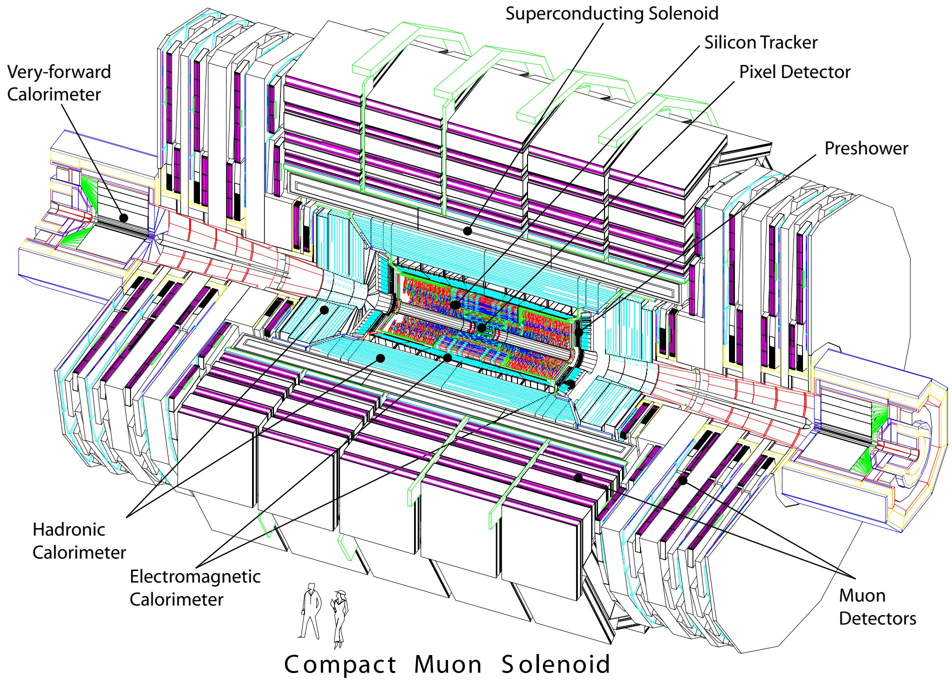

Figure 2.1: A schematic view of the CMS detector.

2.1.2 Coordinate system

The CMS coordinate system is oriented such that the x-axis points south to the center of the LHC ring, the y-axis points vertically upward and the z-axis is in the direction of the beam to the west. The azimuthal angle ϕ is measured from the x-axis in the xy plane; the radial coordinate in the xy plane is denoted by r. The polar angle θ is defined in the rz plane and the pseudorapidity is $\eta = -\ln \tan(\theta/2)$. The momentum component transverse to the beam direction, denoted by p_T, is computed from the x- and y-components, while the transverse energy is defined as $E_T = E \times \sin\theta$.

2.1.3 Magnet

The CMS magnet consists of two main parts: the yoke and the coil. The coil is an indirectly cooled, aluminum stabilized, four-layer superconducting solenoid. The solenoid is 12.5 m long, has a free inner diameter of 6 m and generates a uniform magnetic field of 3.8 T. The inner coil radius is large enough to accommodate the inner tracker and part of the calorimeters. The magnetic flux is returned through a 10,000 t iron yoke in which the muon detector chambers are integrated.

2.1.4 Tracker

The inner tracking system of CMS is designed to provide a precise and efficient measurement of the trajectories of charged particles emerging from the LHC collisions, as well as a precise reconstruction of secondary vertices. It surrounds the interaction point and has a length of 5.8 m and a diameter of 2.5 m. The tracking detector is divided into a pixel detector close to the interaction region and a strip detector covering radii between 0.2 and 1.2 m.

The CMS tracker is composed of a pixel detector with three barrel layers at radii between 4.4 cm and 10.2 cm and a silicon strip tracker with 10 barrel detection layers extending outwards to a radius of 1.1 m. Each system is completed by endcaps that consist of 2 disks in the pixel detector and 3 plus 9 disks in the strip tracker on each side of the barrel, extending the acceptance of the tracker up to a pseudorapidity of $|\eta| < 2.5$.

A schematic drawing of the CMS tracker is shown in Fig. 2.2. At radii of 4.4, 7.3 and 10.2 cm, three cylindrical layers of hybrid pixel detector modules surround the interaction point. They are complemented by two disks of pixel modules on each side. The pixel detector delivers three high precision space points on each charged particle trajectory. In total the pixel detector covers an area of about 1 m^2.

The radial region between 20 cm and 116 cm is occupied by the silicon strip tracker. It is composed of three different subsystems. The Tracker Inner Barrel and Disks (TIB/TID) extend in radius up to 55 cm and are composed of 4 barrel layers, supplemented by 3 disks at each end. TIB/TID delivers up to 4 $r - \phi$ measurements on a trajectory using 320 μm thick silicon micro-strip sensors with their strips parallel to the beam axis in the barrel and radial on the disks. The strip pitch is 80 μm on layers 1 and 2 and 120 μm on layers 3 and 4 in the TIB, leading to a single point resolution of 23 and 35 μm, respectively. In the TID the mean pitch varies between 100 and 141 μm. The TIB/TID is surrounded by the Tracker Outer Barrel (TOB). It has an outer radius of 116 cm and consists of 6 barrel layers of 500 μm thick micro-strip sensors with strip pitches of 183 μm on the first 4 layers and 122 μm on layers 5 and 6. It provides another 6 $r - \phi$ measurements with single point resolutions of 53 and 35 μm, respectively.

The TOB extends between ±118 cm in z. Beyond this z range the Tracker End-Caps (TEC+ and TEC-, where the sign indicates the location along the z axis) cover the region 124 cm $< |z| <$ 282 cm and 22.5 cm $< |r| <$ 113.5 cm. Each TEC is composed of 9 disks, carrying up to 7 rings of silicon micro-strip detectors (320 μm thick on the inner 4 rings, 500 μm thick on rings 5-7) with radial strips of 97 to 184 μm average pitch. Thus, they provide up to 9 ϕ measurements per trajectory.

In addition, the modules in the first two layers and rings, of TIB, TID, and TOB respectively, as well as rings 1, 2, and 5 of the TECs carry a second micro-strip detector module that is mounted back-to-back with a stereo angle of 100 mrad in order to provide a measurement of the second co-ordinate (z in the barrel and r on the disks). The achieved single point resolutions of this measurement are 230 μm and 530 μm in TIB and TOB, respectively, and varies with pitch in TID and TEC. This tracker layout ensures at least $\approx$ 9 hits in the silicon strip tracker in the full range of $|\eta| < 2.4$ with at least $\approx$ 4 of them two-dimensional measurements. The acceptance of the tracker ends at $|\eta| \approx 2.5$.

2.1.5 Electromagnetic calorimeter

The electromagnetic calorimeter of CMS (ECAL) is a hermetic homogeneous calorimeter made of 61 200 lead tungstate ($PbWO_4$) crystals mounted in the central

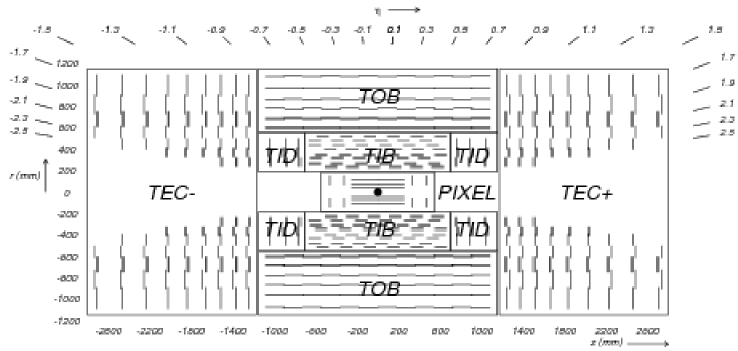

Figure 2.2: Schematic cross section through the CMS tracker. Each line represents a detector module. Double lines indicate back-to-back modules that deliver stereo hit.

barrel part, closed by 7 324 crystals in each of the two endcaps. A preshower detector is placed in front of the endcap crystals. Avalanche photodiodes (APDs) are used as photodetectors in the barrel and vacuum phototriodes (VPTs) in the endcaps. The use of high density crystals has allowed the design of a calorimeter that is fast, has fine granularity and is radiation resistant.

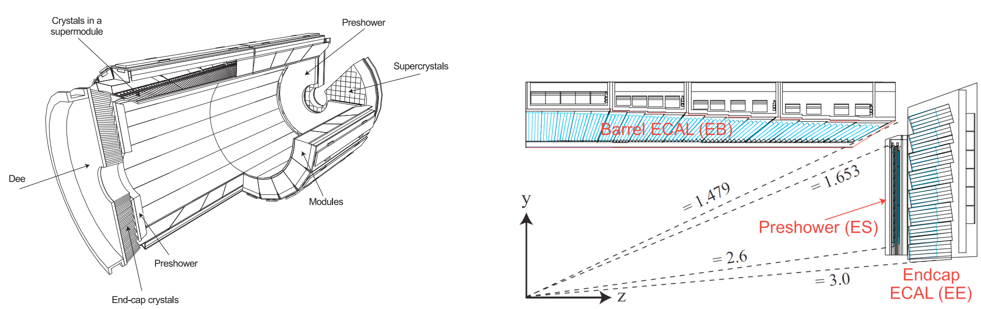

Figure 2.3: Schematic layout of the CMS electromagnetic calorimeter, presenting the arrangement of barrel supermodules, endcaps and the preshower in front (left). Geometric view of one quarter of the ECAL (right).

Figure 2.3 illustrates the ECAL layout. The barrel part of the ECAL (EB) covers the pseudorapidity range $|\eta| < 1.479$. Its crystals are mounted in a quasi-projective geometry to avoid cracks aligned with particle trajectories. The centers of the front faces of the crystals are at a radius 1.29 m. The crystals are contained in a thin-walled alveolar structure made of an aluminum layer, facing the crystal, and two layers of glass fibre-epoxy resin.

The endcaps (EE) cover the rapidity range $1.479 < |\eta| < 3.0$. The longitudinal distance between the interaction point and the endcap envelope is 315.4 cm, taking account of the estimated shift toward the interaction point by 1.6 cm when the 4-T magnetic field is switched on. The endcap consists of identically shaped crystals grouped in mechanical units of 5×5 crystals consisting of a carbon-fibre alveolar structure. Each endcap is divided into 2 halves ("Dees").

A preshower detector is placed in front of the endcaps ($1.653 < |\eta| < 2.6$) to guarantee a reliable discrimination of single photons and photons produced in pairs in neutral pion decays. It also helps the identification of electrons against minimum ionizing particles, and improves the position determination of electrons and photons with high granularity. The preshower is a sampling calorimeter with two layers: lead radiators initiate electromagnetic showers from incoming photons/electrons whilst silicon strip sensors placed after each radiator measure the deposited energy and the transverse shower profiles. The total thickness of the preshower is 20 cm.

The energy resolution of the electromagnetic calorimeter can be parametrized by the following expression:

$$\left(\frac{\sigma}{E}\right)^2 = \left(\frac{S}{\sqrt{E}}\right)^2 + \left(\frac{N}{E}\right)^2 + C^2,$$

where S is the stochastic term, N the noise term and C the constant term.

Typical values of the parameters determined by an electron test beam measurement are $S = 0.028$ GeV$^{1/2}$, $N = 0.12$ GeV and $C = 0.003$.

2.1.6 Hadronic calorimeter

The energy measurement of the ECAL is complemented by the measurement of the hadronic calorimeter (HCAL). The HCAL is a sampling calorimeter using alternating layers of absorber and fluorescent scintillator materials that produce a rapid light pulse when the particle passes through. HCAL consists of four subparts: hadron barrel (HB), endcap (HE), outer (HO) and forward (HF) calorimeters.

The HCAL layout is illustrated in Fig. 2.4. The hadron calorimeter barrel and endcaps sit behind the tracker and the electromagnetic calorimeter as seen from the interaction point. The HB is a sampling calorimeter covering the pseudorapidity range $|\eta| < 1.3$. The HB is divided into two half-barrel sections, each half-section being inserted from either end of the barrel cryostat of the superconducting solenoid and subsequently hung from rails in the median plane.

In the central pseudorapidity region, the combined stopping power of EB plus HB does not provide sufficient containment for hadron showers. To ensure adequate sampling depth for $|\eta| < 1.3$, the hadron calorimeter is extended outside the solenoid with a tail catcher called the HO or outer calorimeter. The HO utilises the solenoid coil as an additional absorber with $1.4/\sin\theta$ interaction lengths and is used to identify late-starting showers and to measure the shower energy deposited after HB.

The hadron calorimeter barrel is radially restricted between the outer face of the electromagnetic calorimeter (R = 1.77 m) and the inner face of the magnet coil (R = 2.95 m). This constrains the total amount of material that can be put in to absorb the hadronic shower. Therefore, an outer hadron calorimeter or tail catcher is placed outside the solenoid complementing the barrel calorimeter.

The hadron calorimeter endcaps (HE) cover a substantial portion of the rapidity range, $1.3 < |\eta| < 3$ (13.2% of the solid angle).

Beyond $|\eta| = 3$, the forward hadron calorimeters (HF) placed at 11.2 m from the interaction point extend the pseudorapidity coverage down to $|\eta| = 5.2$ by means of a Cherenkov-based, radiation-hard technology.

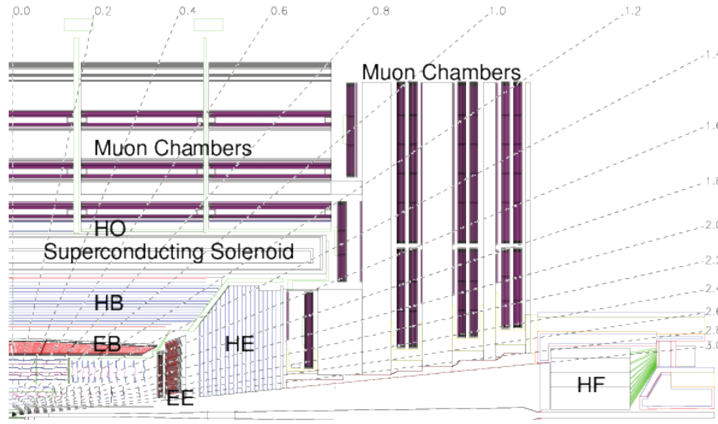

Figure 2.4: Longitudinal view of the CMS detector showing the locations of the hadron barrel (HB), endcap (HE), outer (HO) and forward (HF) calorimeters, as well as the muon detectors.

2.1.7 Muon system

The CMS muon system is designed to have the capability of reconstructing the momentum and charge of muons over the entire kinematic range available at the LHC. The muon system has three functions: muon identification, momentum measurement, and triggering. Good muon momentum resolution and trigger capability are enabled by the high-field solenoidal magnet and its flux-return yoke. The latter also serves as a hadron absorber for the identification of muons.

The muon system has a cylindrical, barrel section and two planar endcap regions, as illustrated in Fig. 2.4.

In the barrel region, where the neutron-induced background is small, the muon rate is low, and the magnetic field is uniform and mostly contained in the steel yoke, drift chambers with standard rectangular drift cells are used. The barrel drift tube (DT) chambers cover the pseudorapidity region $|\eta| < 1.2$ and are organized into 4 stations interspersed among the layers of the flux return plates. The first 3 stations each contain 8 chambers, in 2 groups of 4, which measure the muon coordinate in the $r - \phi$ bending plane, and 4 chambers that provide a measurement in the z direction, along the beam line. The fourth station does not contain the z-measuring planes.

In the two endcap regions of CMS, where the muon rates and background levels are high and the magnetic field is large and non-uniform, the muon system uses cathode strip chambers (CSC). With their fast response time, fine segmentation, and radiation resistance, the CSCs identify muons between $|\eta|$ values of 0.9 and 2.4. There are 4 stations of CSCs in each endcap, with chambers positioned perpendicular to the beam line and interspersed between the flux return plates. The cathode strips of each chamber run radially outward and provide a precision measurement in the $r - \phi$ bending plane. The anode wires run approximately perpendicular to the strips and are also read out in order to provide measurements of η and the beam-crossing time of muons. Each 6-layer CSC provides robust pattern recognition for rejection of non-muon backgrounds and efficient matching of hits to those in other stations and in the CMS inner tracker.

Because of multiple-scattering in the detector material before the first muon station, the offline muon momentum resolution of the standalone muon system is about 9% for small values of η and momentum for transverse momenta up to 200 GeV. At 1 TeV the standalone momentum resolution varies between 15% and 40%, depending on $|\eta|$. A global momentum fit using also the inner tracker improves the momentum resolution by an order of magnitude at low momenta. At high momenta (1 TeV) both detector parts together yield a momentum resolution of about 5%. The Level-1 trigger p_T resolution is about 15% in the barrel and 25% in the endcap.

A complementary, dedicated trigger system consisting of resistive plate chambers (RPC) was added in both the barrel and endcap regions. The RPCs provide a fast, independent, and highly-segmented trigger with a sharp p_T threshold over a large portion of the rapidity range ($|\eta| < 1.6$) of the muon system. The RPCs are double-gap chambers, operated in avalanche mode to ensure good operation at high rates. They produce a fast response, with good time resolution but coarser position resolution than the DTs or CSCs. They also help to resolve ambiguities from multiple hits in a chamber. A total of 6 layers of RPCs are embedded in the barrel muon system, 2 in each of the first 2 stations, and 1 in each of the last 2 stations. The redundancy in the first two stations allows the trigger algorithm to work even for low-p_T tracks that may stop before reaching the outer two stations. In the endcap region, there is a plane of RPCs in each of the first three stations in order for the trigger to use the coincidences between stations to reduce background, to improve the time resolution for bunch crossing identification, and to achieve a good p_T resolution.

2.1.8 Trigger

The LHC provides proton-proton and heavy-ion collisions at high interaction rates. For protons the beam crossing interval is 25 ns, corresponding to a crossing frequency of 40 MHz. Since it is impossible to store and process the large amount of data associated with the resulting high number of events, a drastic rate reduction has to be achieved. This task is performed by the trigger system, which is the start of the physics event selection process.

The rate is reduced in two steps called Level-1 (L1) Trigger and High-Level Trigger (HLT), respectively. The Level-1 Trigger consists of custom-designed, largely programmable electronics, whereas the HLT is a software system implemented in a filter farm of about one thousand commercial processors. The rate reduction capability is designed to be at least a factor of 10^6 for the combined L1 Trigger and HLT. The L1 Trigger uses coarsely segmented data from the calorimeters and the muon system, while holding the high-resolution data in pipelined memories in the front-end electronics. The HLT has access to the complete read-out data and can therefore perform complex calculations similar to those made in the analysis offline software. The architecture of the CMS Level-1 trigger is illustrated in Fig. 2.5.

The L1 Trigger has local, regional and global components. At the bottom end, the Local Triggers, also called Trigger Primitive Generators (TPG), are based on

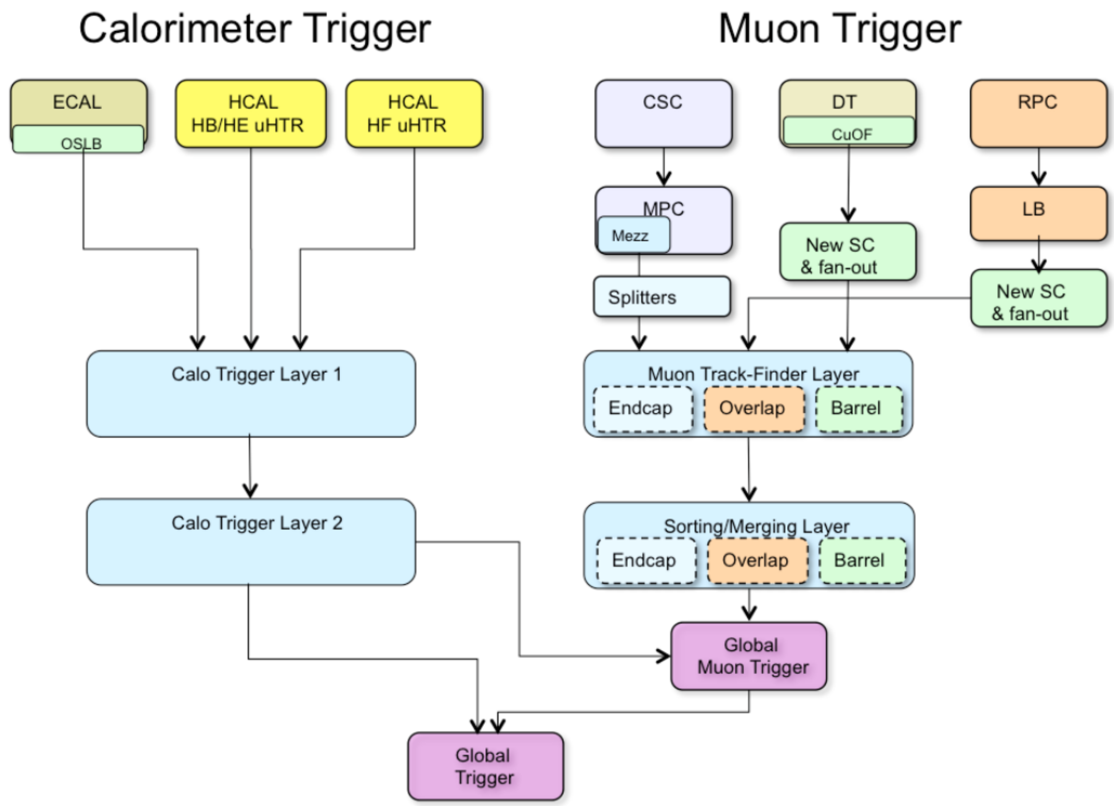

Figure 2.5: Architecture of the CMS trigger.

energy deposits in calorimeter trigger towers and track segments or hit patterns in muon chambers, respectively. Regional Triggers combine their information and use pattern logic to determine ranked and sorted trigger objects such as electron or muon candidates in limited spatial regions. The rank is determined as a function of energy or momentum and quality, which reflects the level of confidence attributed to the L1 parameter measurements, based on detailed knowledge of the detectors and trigger electronics and on the amount of information available. The Global Muon Trigger and Layer 2 of Calo Trigger determine the highest-rank muon and calorimeter objects across the entire experiment and transfer them to the Global Trigger, the top entity of the Level-1 hierarchy. The latter takes the decision to reject an event or to accept it for further evaluation by the HLT. The Level-1 Accept (L1A) decision is communicated to the sub-detectors through the Timing, Trigger and Control (TTC) system.

2.2 The CT–PPS detector

The CMS-TOTEM Precision Proton Spectrometer (CT–PPS) [9] adds precision proton tracking and timing detectors in the very forward region on both sides of CMS at about 200 m from the interaction point (IP).

The CT–PPS detector consists of a silicon tracking system to measure the position and direction of the scattered protons, and a set of timing counters to measure their arrival time. The detector planes are inserted horizontally into the beam pipe by means of "Roman Pots" (RPs), i.e. movable near-beam devices that allow the detectors to be brought very close (down to a few mm) to the beam without affecting the vacuum, the beam stability, or other aspects of the accelerator operation. CT–PPS makes use of the LHC magnets between the IP and detector stations to bend protons that have lost a small fraction of their momentum out of the beam envelope so that their trajectories can be measured. This allows the reconstruction of the mass and momentum of the centrally produced system, as well as of the z coordinate of the primary vertex.

The layout of the beam line from the IP to the 210 m $r$egion on one of the two sides of CMS is shown in Fig. 2.6. The two sides are referred to as "arms" in the following. The arms to the left (positive z direction) and to the right of CMS when looking from the center of the LHC correspond to LHC sectors 45 and 56 on the two sides of interaction point 5 where CMS is located, respectively. In each arm there are two tracking units, referred to as "210 NEAR" (210N) and "210 FAR" (210F), which are located at 203.8 m and 212.6 m from the IP, respectively. The timing detectors are housed in low-impedance, cylindrical RPs specially built for CT–PPS, located at 215.7 m from the IP.

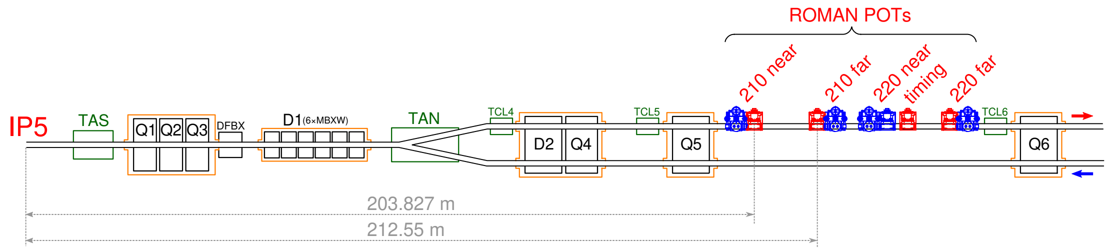

Figure 2.6: Schematic layout (not to scale) of the beam line as seen from above between the interaction point (IP5) and the region where the RPs are located in LHC sector 56. Dipole magnets (D1, D2) of single- (MBXW) and twin-aperture, quadrupoles (Q1Q6), collimators (TCL4TCL6), absorbers (TAS, TAN), and quadrupole feedboxes (DFBX) are shown. The 210 near and 210 far units are indicated, along with the timing RPs. The 220 near and 220 far units (not used here) are also shown. The RPs indicated in red are the horizontal CT–PPS ones; those in blue are part of the TOTEM experiment. The red (blue) arrow indicates the outgoing (incoming) beam. In the CMS coordinate system, the z axis points to the left. The arm in the opposite LHC sector 45 (not shown) is symmetric with respect to the IP.

2.2.1 Roman Pots

The Roman Pot is a device introduced at the ISR for the detection of protons from elastic or diffractive scattering that remain inside the beam pipe. Roman Pots have been successfully employed at the SPS, the TEVATRON, RHIC and HERA. Detectors are placed inside a secondary vacuum vessel, called pot, and moved into the primary vacuum of the machine through vacuum bellows. In this way the detectors are physically separated from the primary vacuum, which is thus protected from an outgassing of the detector materials.

The CT–PPS detectors are housed inside the Roman Pots previously used for the TOTEM experiment. The Pots are made of 316LN grade stainless steel with a box shape of dimensions 50×124 mm^2, and 2 mm wall thickness. A Ultra-High Vacuum (UHV) flange is welded to the box by electron beam welding. The bottom side of the flange is connected to bellows, to seal the machine vacuum. The opposite side is connected to the pot itself equipped with the detectors, which seals the secondary vacuum volume.

Since it is crucial to reduce the amount of insensitive material close to the beam, the RPs are equipped with a thin window of 150 μm thickness located at the bottom of the pot, on the side facing the beam. To satisfy the requirements of flatness better than 50 μm, UHV leak tightness, and capability to stand the limit pressure of 1.5 bars, a brazing assembling procedure was chosen to realize the thin window. The first step consists of brazing a thin window in stainless steel (316L) on the bottom part of the RP. Successively, the milling of the lateral sides is carried out, leading to a 0.5 mm window.

The TOTEM Roman Pots operated mainly in special runs with low beam intensities and luminosities. Neither collision debris showers nor beam impedance effects were an issue. However, in the case of operation during the standard, high-intensity LHC runs, these effects become important. Because of the presence of resonant cavities inside the TOTEM RPs, their insertion close to the beams at high luminosity would cause impedance heating of the pots, resulting in outgassing and vacuum degradations that finally would generate losses leading to beam dumps [27].

To mitigate this effect, all RPs intended for high-luminosity use were optimized: the old TOTEM RPs were equipped with ferrite RF shields minimizing cavity resonances, and the newly added pots housing the timing detectors were designed already with a cylindrical shape that minimizes impedance.

The RP layout featuring the shields, as shown in Fig. 2.7, was first implemented in the tracking stations at 203 and 214 m in 2016. For the 2017 running, the same modification was made to the TOTEM horizontal pot at 220 m.

A cylindrical RP was designed to house timing detectors, optimized with respect to material budget and RF interference with the LHC beam as discussed above. A cylindrical profile provides the necessary space for all potential technologies of timing detectors and at the same time reduces the beam coupling impedance by minimizing resonant cavities. In this design, the ferrite is integrated as a ring in the flange rather

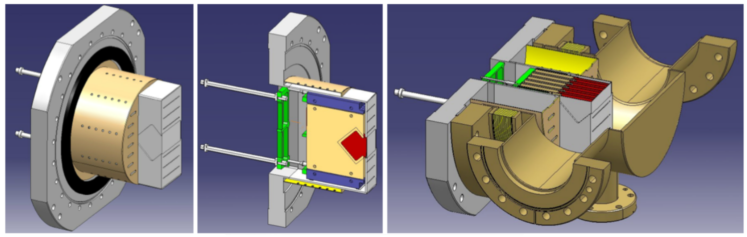

Figure 2.7: Schematic layout of the box-shaped horizontal RP with the cylindrical RF shield, with the tracking detector packages installed inside. The ferrite shielding is mounted on the moving detector housing.

than mounted on the moving detector housing. All vacuum-side surfaces of the RP stations have a 2 μm thick Non-Evaporative Getter (NEG) coating to reduce the outgassing and hence improve the LHC vacuum stability. As for the box-shaped RP, also the cylindrical one has a thin window (300 μm thick) to minimize the amount of material traversed by the scattered protons. The layout of the cylindrical vessel is shown in Fig. 2.8. One cylindrical RP station has been installed at $\sim$215 m from the IP on each side of CMS.

Figure 2.9 illustrates the layout of all CT–PPS detector stations in the LHC tunnel.

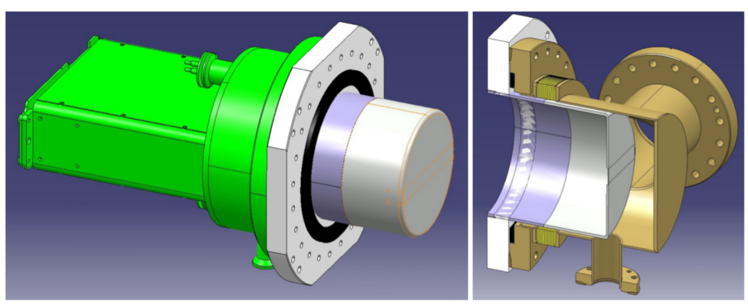

Figure 2.8: Schematic layout of the cylindrical detector housing designed to accommodate timing detectors. The ferrite shielding is integrated as a ring in the flange.

2.2.2 Tracking silicon strip detectors

Silicon strips were used for the tracking during the exploratory phase of the project (2016). The tracking RPs were instrumented with 10 planes of edgeless silicon strip

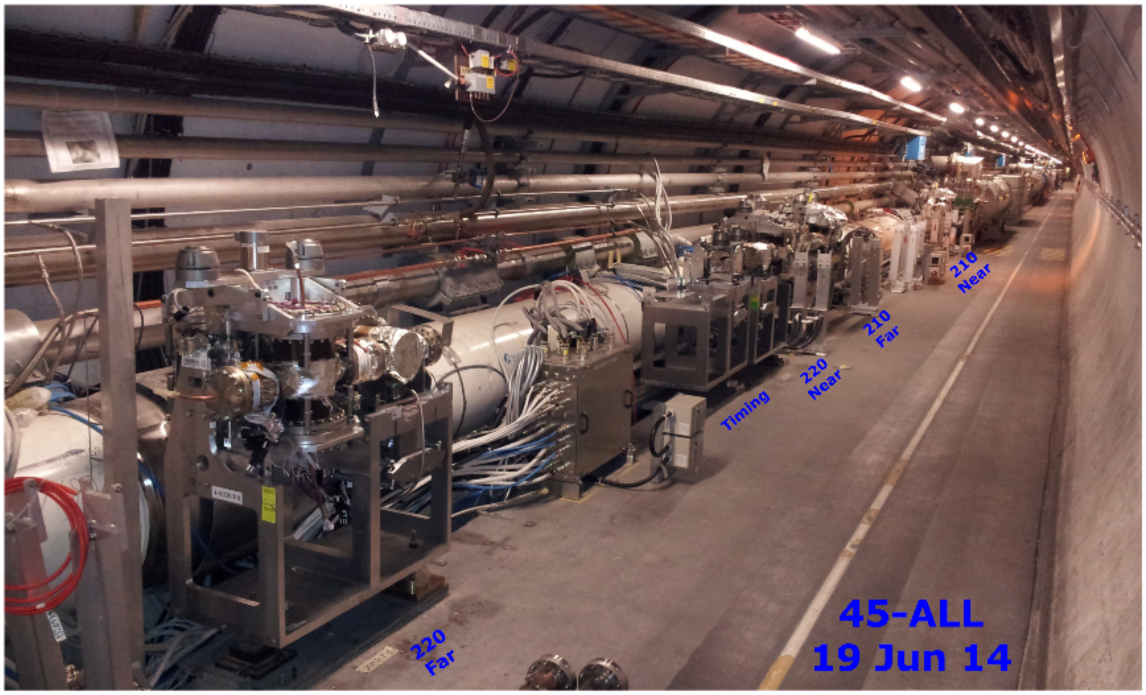

Figure 2.9: The beamline in Sector 4-5 with the RPs installed.

sensors each, providing a spatial resolution of about 12 μm. Five of these planes were oriented with the silicon strips at a $+45^{\circ}$ angle with respect to the bottom of the RP, while the other five had the strips at a -45° angle. In total each RP silicon detector plane contained 512 individual strips, with a pitch of 66 μm. A schematic diagram of the silicon strip sensors, indicating their orientation relative to the LHC beam, is shown in Fig. 2.10.

The hit efficiency per plane was estimated to be >97% before the effect of radiation damage to the sensors. The signal from the silicon detectors was contained within one 25 ns bunch crossing of the LHC. The data were read out by means of a VFAT chip [28], and recorded through the standard CMS data acquisition system. The sensors have been extensively used by the TOTEM experiment. The TOTEM silicon strip sensors were not designed to sustain exposure to the high radiation doses of the standard high-luminosity LHC fills. As expected, a first set of such planes suffered severe radiation damage after about 10 fb^{-1}, and was replaced by a set of spares.

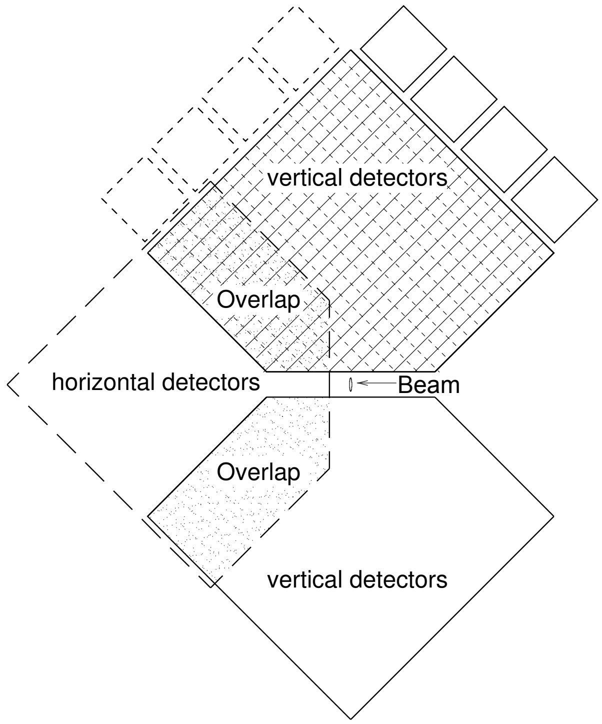

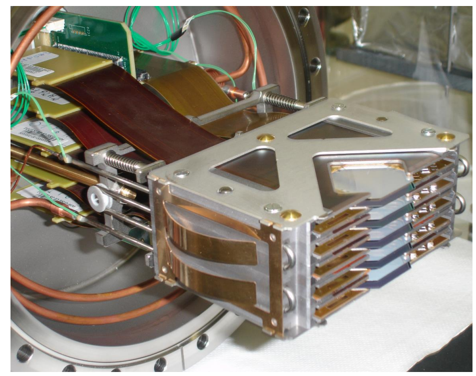

Figure 2.10: Left: schematic layout of the silicon strip detectors in one RP station. Both the horizontal RP and the vertical RPs, which are used only for special low-luminosity calibration fills, are shown. In the top RP, the silicon strips oriented at $+45^{\circ}$ and -45° angles are indicated by the diagonal lines. Tracks in the overlap region, indicated by the shaded area, are used to perform the relative alignment of the RPs in the calibration fills. Right: strip detector module mounted in RP.

2.2.3 Tracking pixel detectors

The CT–PPS tracking was upgraded with 3D pixel sensors in the course of the 2016-2017 end-of-the-year shutdown. Two detector stations per arm (horizontal RPs at 210 and 220 m from IP5) were equipped with six 3D silicon pixel-sensor modules [29] each.

The main feature of 3D sensors is a column shape electrode perpendicular to the surface, instead of on the surfaces, as in the planar technology. This results in decoupling the sensor thickness from the distance between electrodes. The main advantages are lower depletion voltage, faster charge collection and high charge collection efficiency after irradiation.

The sensors used for CT–PPS were built by CNM [30]. A double-sided non-passing-through technology was used, meaning that n^+ and p^+ electrodes are etched from opposite surfaces of the wafer, and stop before reaching the other surface (see Fig. 2.11). The sensors were built on a 230 μm thick wafer and the columns are 200 μm deep. A 200 μm slim edge is implemented with p-type column fences surrounding the sensitive area, allowing to minimize the size of the "dead region". By increasing the bias voltage, the inefficient edge can be reduced down to 50 μm.

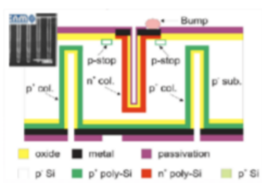

(a) CNM 3D cross section.

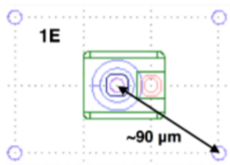

(b) 1E pixel layout.

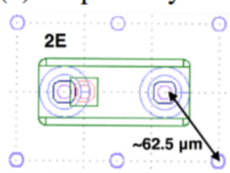

(c) 2E pixel layout.

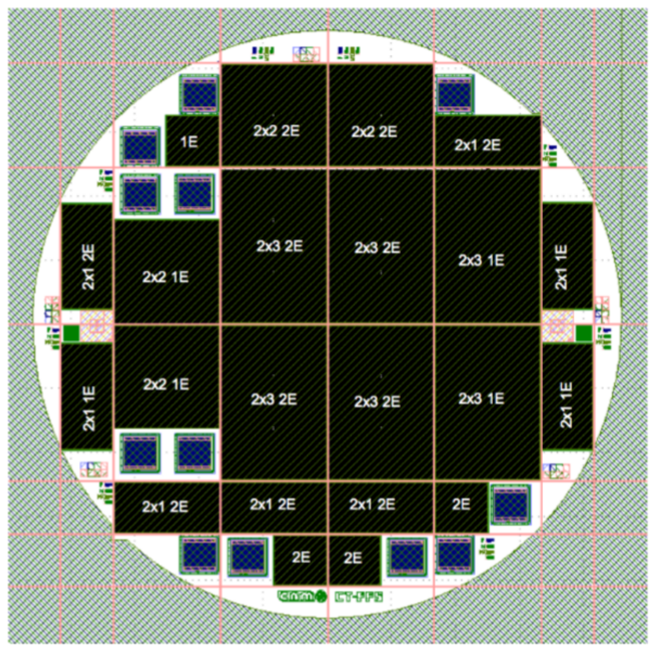

(d) Wafer layout for the CT-PPS 3D sensors produced at CNM.

Figure 2.11: Characteristics of the CNM 3D sensor for CT–PPS.

The sensors are designed to be read out by the PSI46dig ReadOut Chip (ROC), the same used for the CMS Phase I pixel detector. It consists of a 52×80 matrix of pixels with size 150 × 100 μm^2 . The baseline design for CT–PPS is a 2E pixel configuration (two readout columns for every pixel as shown in Fig. 2.11) and 2×3 sensor modules, which means readout by 6 ROCs. However, also 1E (one readout column for every pixel as shown in Fig. 2.11) and 2×2 sensor modules are included in the wafer design as a backup. In the wafer layout also single-ROC sensors are present and are used for test purposes.

Each tracking station is composed of 6 planes (Fig. 2.12) tilted by 18.4° in order to increase the charge sharing and therefore improve the resolution. Each plane is made of a 3D module glued on a Thermal Pyrolithic Graphite (TPG) layer that provides the thermal contact to the cooling circuit. The module is wire-bonded to a flex circuit that allows the connection to the so-called RPix portcard (Fig. 2.13). The board is derived from the TOTEM Si strip detector portcard with the components of the CMS Phase I pixel upgrade, and interfaces the modules to the back-end electronics, which is identical to the one of the CMS pixel detector.

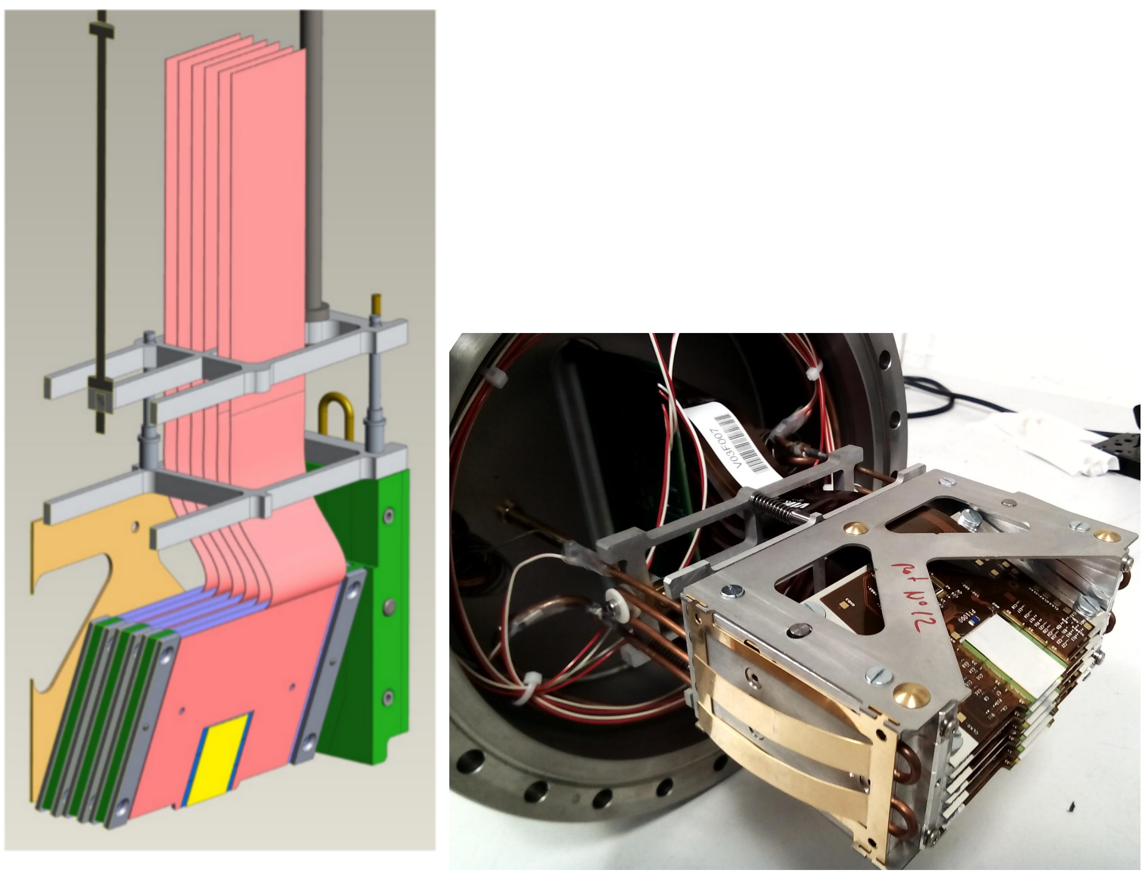

Figure 2.12: Left: Schematic layout of the pixel detector modules mounted in each RP station. The TPG layer is in contact with the aluminum structures in which the cooling lines are inserted. Right: photo of the assembled pixel detector modules.

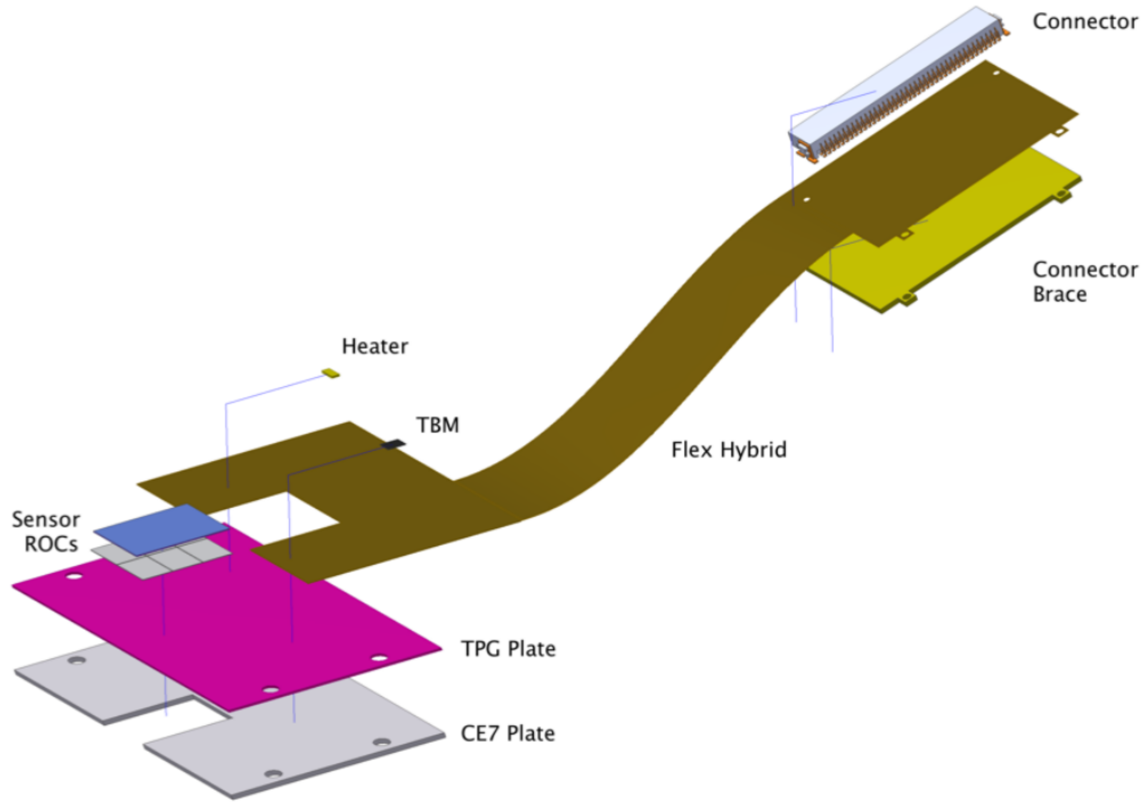

Figure 2.13: Exploded view of a RPix module. The support plate consists of two layers: the first one is made of aluminum while the second one is made of Thermal Pyrolithic Graphite (TPG). A long kapton flexible hybrid circuit is glued on top of the TPG layer. The circuit hosts the silicon sensor with the ROCs and the TBM, and provides the connections to the readout board.

2.2.4 Timing detectors

CT–PPS has to operate at high luminosity with up to 50 pile-up interactions per bunch crossing. It is therefore crucial to associate the protons measured with CT–PPS with the vertex reconstructed in CMS, especially in the cases in which the central detector does not reconstruct all the final-state products (neutrinos or beyond standard model objects) and the kinematic cuts constraining the central system and the proton are less effective. In order to achieve this, a “z-by-timing” method is used, based on the measurement of the difference of arrival times of the two protons in opposite directions. In particular, with a 10 ps timing resolution, a vertex position resolution of $\sigma_z \sim 2$ mm can be obtained, which would allow to strongly suppress the pile-up induced backgrounds.

Each timing station is equipped with four planes of timing detectors. While in 2016 only diamond detectors were used, in 2017 each station included three diamond and one Ultra-Fast Silicon Detector (UFSD) planes. The pressure in the timing RPs is set between 100 and 110 mbar to avoid discharging and the temperature of the cooling circuit is set to 15° C. The diamond and UFSD detectors are described in the following sections.

To measure precisely the arrival times of the protons and their difference, it is necessary to send a common, picosecond range, precision time reference signal to the detectors. The present detector has two different systems that can provide the precise clock: the Universal Picosecond Timing System based on an optical network and an RF-feedback with low-loss coaxial cable. Both systems have comparable figures of merit.

2.2.5 Diamond detector

Each diamond plane is made of four $4{\times}4$ mm^2 single crystals produced by chemical vapor deposition (Fig. 2.14). The diamond sensors were grown to a thickness of 500 μm. Each of the four crystals of the plane has a different segmentation along the x direction in order to equalize the channel occupancy, and hence smaller pads are present closer to the beam. Crystals with different shape and size are glued in a different order on all planes (Fig. 2.15) to improve the x-resolution to $\sim$150 μm and allow a rough track reconstruction. The timing resolution measured in a test beam is $\sim$80 ps per plane [31]. Since the technology is intrinsically radiation hard, the sensors should be able to withstand the whole proton flux CT–PPS is expected to be exposed to.

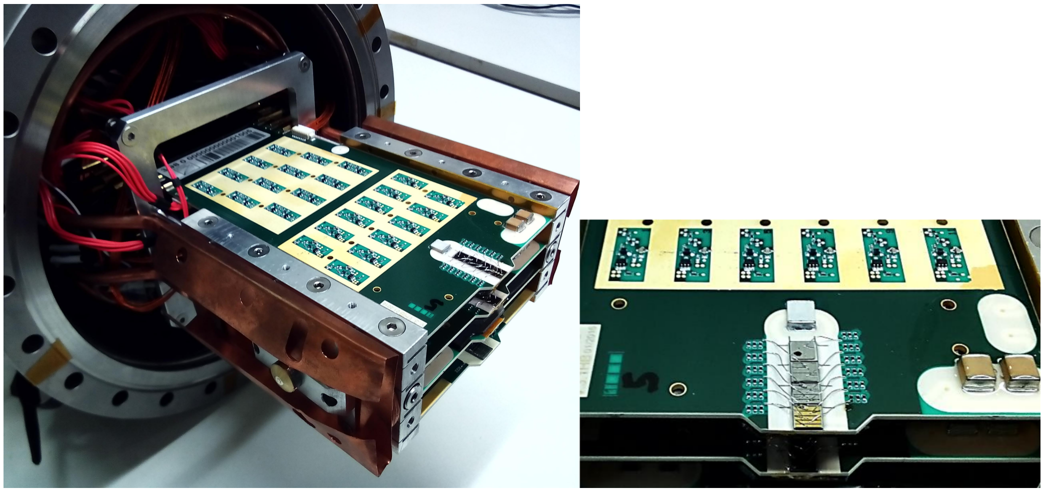

Figure 2.14: Left: diamond detector package consisting of four diamond planes connected to readout in a RP. Right: close-up of one of the diamond planes with crystals mounted.

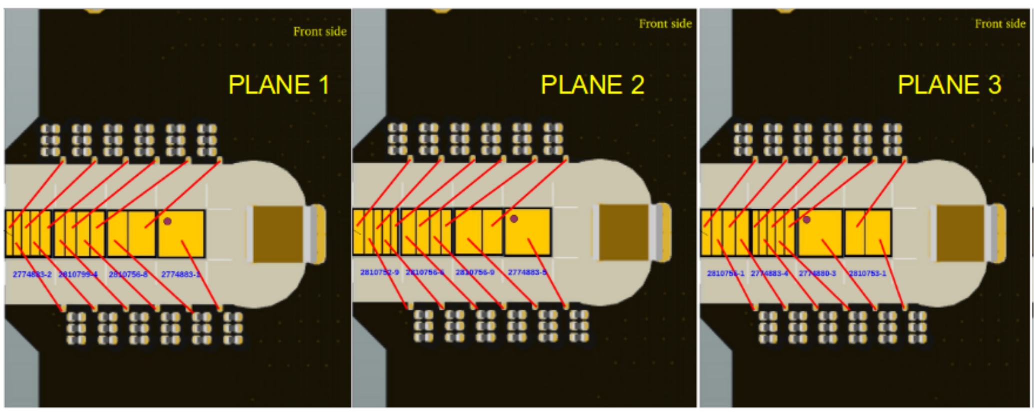

Figure 2.15: A schematic picture of the layout of the three diamond detector planes. The crystals with different segmentation are glued in a different order on each plane to improve the detector resolution.

2.2.6 UFSD detector

The UFSD sensors installed in CT–PPS [32] were produced at CNM. Each sensor (Fig. 2.16) has an active area of 12×6 mm^2 and a thickness of 50 μm. The sensor pads are organized in a matrix of 16 columns and 2 rows. Within the pad the pixel size varies as a function of the distance from the beam: the 8 pads for each column closer to the RP edge have a dimension $\sim$ 2 mm^2, the remaining have an area of $\sim$ 3 mm^2 .

The expected resolution for the UFSD technology from a test beam is ∼ 35 ps [33].

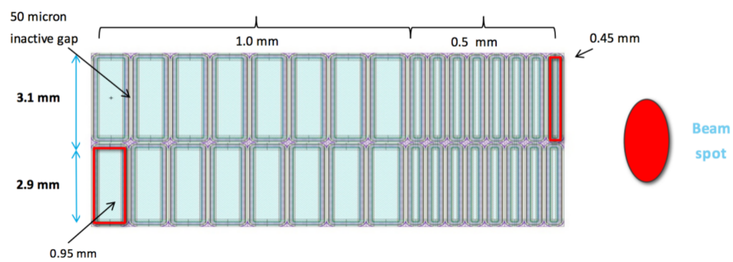

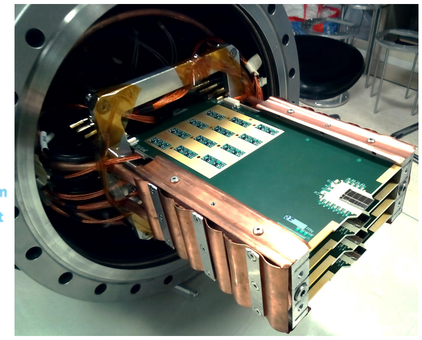

Figure 2.16: Left: Schematic layout of the UFSD sensors on a plane. Right: photo of the assembled timing detector module with UFSD plane installed.

2.2.7 CT–PPS readout

The CT–PPS strip detectors are integrated into the existing TOTEM DAQ [34]. The TOTEM Roman Pot Motherboard (RPMB) [35] is used to interface the hybrids with silicon detectors and front end chips in the Roman Pots, and the outside world. The RPMB is glued on the vacuum flange that separates the vacuum chamber containing the detector hybrids, and forms the feed-through between vacuum and atmosphere. The hybrids have a flexible part for connection to the motherboard. The motherboard is equipped with connectors to the detector from one side and a panel with connectors to the patch panel from the other side.

The data sent by the VFAT2 [36] front end chips upon a level 1 trigger signal is converted from LVDS (Low Voltage Differential Signaling interface standard [37]) to CMOS on the RPMB and then presented to the gigabit optical hybrids (GOH) modules, which serialize and convert the electrical data to optical for transmission to the Data Acquisition (DAQ) system in the counting room.

The design of the front-end electronics and of the DAQ for the CT–PPS pixel detector is based on that developed for the Phase 1 upgrade of the CMS silicon pixel detectors. The complete readout chain of one CT–PPS detector package is shown in Fig. 2.17.

Each RPix module consists of a flexible hybrid circuit hosting: the silicon sensor, six PSI46dig ROCs bump-bonded to the silicon sensor, and one Token Bit Manager (TBM) chip. ROCs are responsible for charge collection, charge discrimination and data buffering, while the TBM reads out the six ROCs of the module using a token ring protocol and serializes the data over a single output line.

The flexible circuit with the detector module is glued on top of a TPG layer, a low density material consisting of stacked graphite sheets and with extremely high thermal conductivity. Since it is a very fragile material, an aluminum encapsulation is needed for a proper handling. An exploded view of a module is shown in Fig. 2.13.

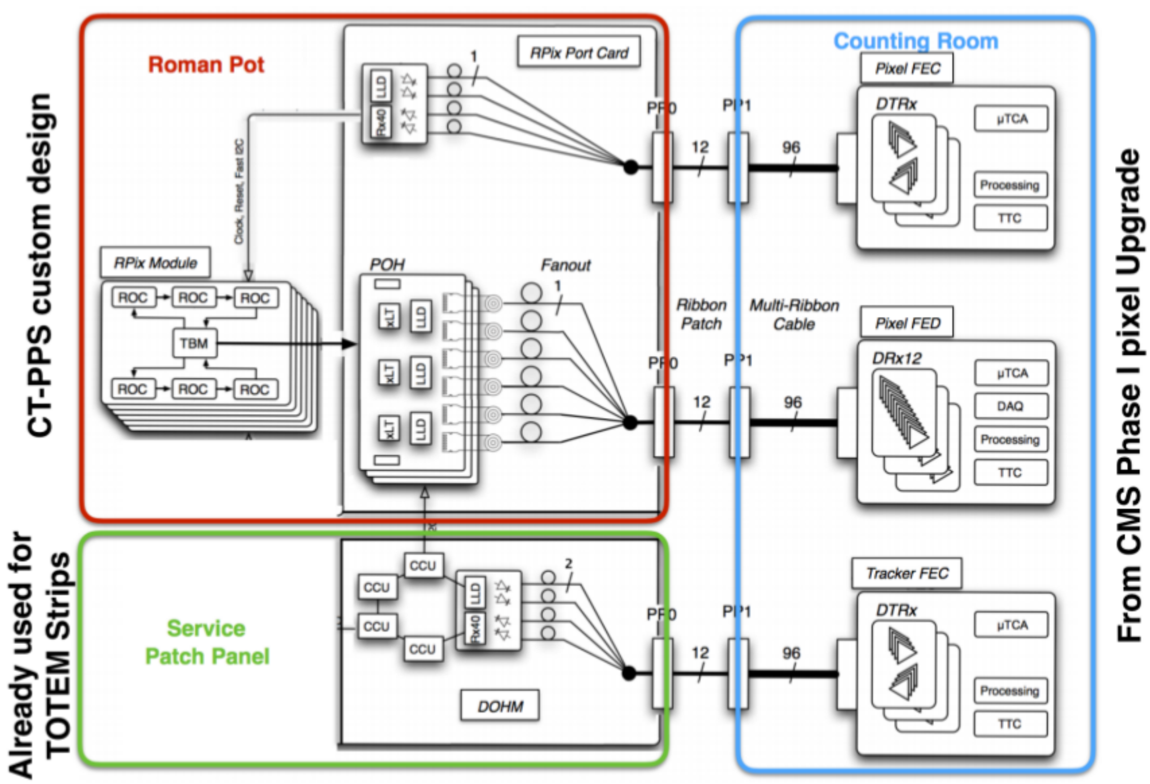

Figure 2.17: Detector readout blocks. The RPix modules and the RPix portcards are located inside the RP, the DOH Mezzanine (DOHM) is installed inside the service patch pannel in the LHC tunnel, and the FEDs and FECs are hosted in the counting room.

The RPix portcard is custom-designed, based on the TOTEM portcard that fits inside the Roman pot, but with most of the components of the Phase I central pixel detector. The board receives the output data from the six RPix modules and transmits them on six optical fibres towards the Pixel Front-End Driver (FED) DAQ module, using a POH7 opto-electrical converter mezzanine card [38].

The portcard also receives fast configuration commands from the Pixel Front-End Controller (FEC) via optical fibers, translates these signals using Detector Optical Receivers (DOH) and dispatches them to the modules. Moreover the RPix portcard integrates other components such as the radiation sensors, part of the TOTEM DCS (Detector Control System) radiation monitoring, and the CMS Tracker Optical Control Link components.

For the back-end DAQ and control systems, composed of a FED and two FECs, μTCA crates are used. These crates, developed for the Phase 1 Pixel Upgrade project, replace the VME standard used earlier for the CMS and TOTEM DAQ. Crates are located in the service cavern of CMS in order to be also accessible during data taking.

For the diamond and UFSD readout electronics, illustrated in Fig. 2.18, already available components have been chosen: the amplifier-discriminator NINO and the time-to-digital converter HPTDC, as shown in Fig. 2.18. NINO is an 8-channel amplifier and discriminator implemented in CMOS 250 nm technology [39]. Each channel is a fully differential ultra fast ($\leq$ 1 ns peaking time) preamplifier-discriminator. The NINO output is a voltage pulse. The output pulse width is equal to the time-over-threshold, and therfore is a function of the input pulse amplitude. The intrinsic time resolution of the NINO chip was measured to be below 10 ps (RMS). The LVDS output of the NINO is fed into the HPTDC. The time base for the TDC measurement is a Delay Locked Loop (DLL) with 32 delay elements and a clock synchronous counter, both driven by the same clock reference. The clock reference can be taken directly from the clock input of the TDC chip or can come from an on-chip Phase Locked

Loop (PLL). The interface between the HPTDC and the timing FEC and FED is an FPGA in the front-end board installed in the tunnel.

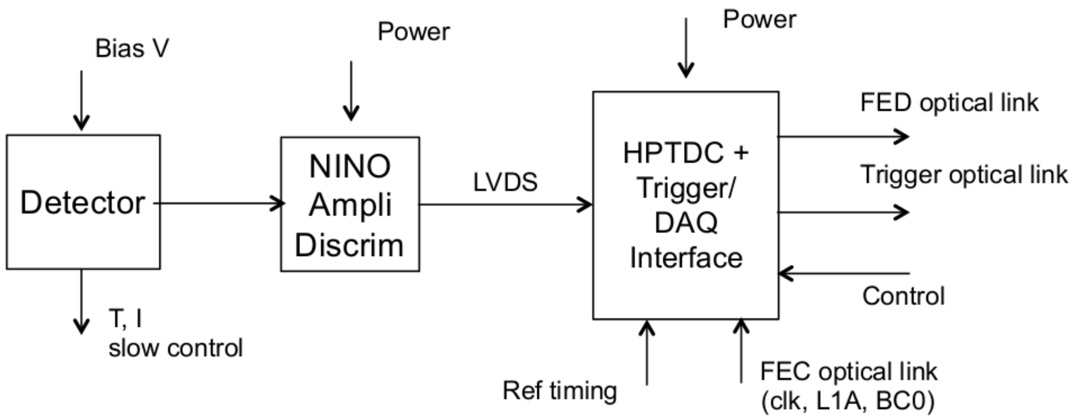

Figure 2.18: Diagram of of the timing readout system.

Chapter 3

CT–PPS proton reconstruction

3.1 Introduction

Precise reconstruction of the scattered proton kinematics with CT–PPS is based on two crucial components: alignment and optics. "Aligning" the spectrometer amounts to determining the relative position of the detector with respect to one another, the beam and the rest of CMS. Evaluating the optics corresponds instead to determining the integral of the magnetic fields traversed by the scattered proton.

The corresponding corrections allow to compute the fraction of momentum lost by the beam proton in the interaction as a function of the proton impact point in the RP detectors. The proton momentum (p) loss ($\xi = /p$) is a key variable as it constrains the kinematics of the central system produced in the proton-proton collision.

The contents of this chapter apply to both the 2016 and 2017 data taking periods, with the exception of Sec. 3.3.2, which specifically refers to the 2016 set-up.

3.2 Alignment of the CT–PPS tracking detectors

An overview of the procedure is given here; more details are available in Ref. [40].

The alignment consists of two conceptually distinct parts:

- Alignment in a special, low-luminosity calibration fill ("alignment fill"), where RPs are inserted very close to the beam.
- Transfer of the alignment information to the standard, high-luminosity physics fills.

3.2.1 Alignment fill

The first step is the beam-based alignment, the purpose of which is to establish the position of the RPs with respect to the LHC collimators and the beam. It takes place only once per LHC optics setting. In this procedure, the TOTEM vertical RPs [41] (cf. Fig. 2.7) are used together with the horizontal CT–PPS RPs. The beam is first scraped with the collimators so that it develops a sharp edge. Then each RP is moved in small (approximately 10 μm) steps until it is in contact with the edge of the beam, which generates a rapid increase in the rate observed in the beam-loss monitors close to CT–PPS. At this point, each RP is at the same distance (in units of σ, the standard deviation of the spatial distribution of the beam in the transverse direction) as the collimators, i.e. the RP is at the edge of the shadow cast by the collimators. The necessity to get very close to the beam stems from the need of having the TOTEM vertical and the CT–PPS RPs overlap. Data are then taken in this configuration, with the horizontal and vertical RPs at 8 and 5 σ, respectively.

The second step consists of determining the relative position of all the sensors in each arm using the data from the alignment fill. This is achieved by minimizing the residuals between hit positions and fitted tracks. The position (shift perpendicular to the beam) and rotation (about the beam axis) of each sensor are thereby determined. While no event selection is necessary (since the method assumes that the tracks are linear, which is the case as there are no magnets at the RP location), the most valuable events are those with tracks reconstructed when the RP detectors overlap, which allow the relative alignment of the RPs to be determined. The method is applied to several data subsamples in order to verify the stability of the results.

Finally, the alignment of CT–PPS with respect to the beam is performed, again with data from the alignment fill. A sample of several thousand elastic scattering events, $pp \rightarrow pp$, is used for that purpose. The LHC optics causes the elastic hit distribution in any vertical RP to have an elliptical shape centered on the beam position. This symmetry is exploited to determine the position of the RP with respect to the beam.

The uncertainties in the results of the procedure just discussed are 5 mrad for rotations, 50 μm for the horizontal positions, and 75 μm for the vertical positions.

3.2.2 Physics fills

Since the RPs move, and the beam position can change, the position of CT–PPS with respect to the beam needs to be redetermined for each fill. The physics fills are characterized by high intensity with only the horizontal RPs inserted at much larger distances (about $15\,\sigma$) from the beam than in the alignment fill, and therefore a different procedure is employed.

The horizontal alignment is based on the assumption that the scattered protons from a pp collision at the IP have the same kinematic distributions in all fills. The stability of the LHC conditions (RP positions, collimator setting, magnet currents, and beam orbit) reflects on the spatial distributions of the track impact points observed in the RPs. The alignment is then achieved by matching these distributions from a physics fill to those from the alignment fill. An example of this procedure is shown in Fig. 3.1. For this method to work, it is important to suppress the background due to secondary interactions taking place between the IP and the RPs. To this end, the correlation between the coordinates of the horizontal hit positions in the near and far RPs is used. The total uncertainty of the horizontal alignment is about 150 μm.

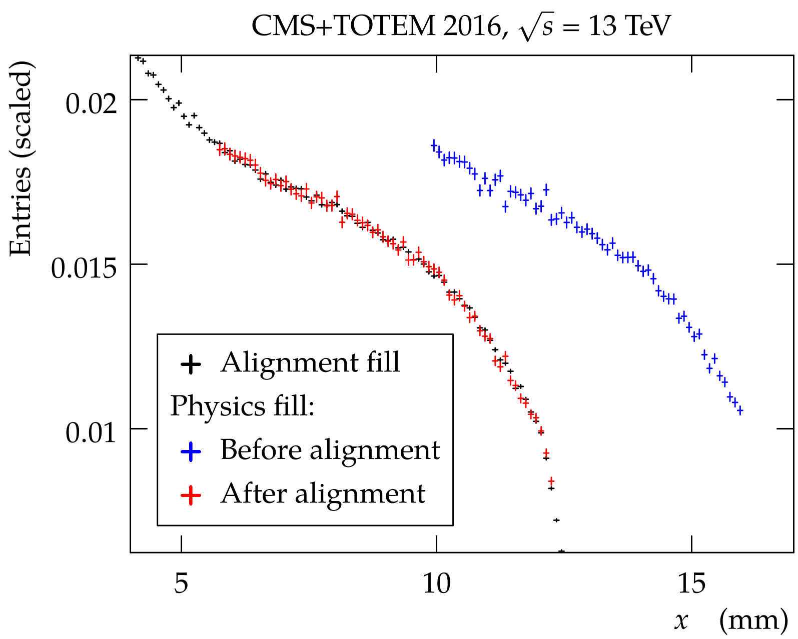

Figure 3.1: Distribution of the track impact points as a function of the horizontal coordinate for the alignment fill (black points), a physics fill before alignment (blue points), and after alignment (red points). The beam center is at $x = 0$ for the black and red points; the x axis origin is undefined for the blue points. In the alignment procedure the overall normalization of the histogram is irrelevant; the histograms from different fills are therefore rescaled to compare their shapes.

The beam vertical position with respect to the sensors is determined by fitting a straight line to the y coordinates of the maximum of the track impact point distribution as a function of x (horizontal beam position). The fitted function is then extrapolated to $x = 0$. This procedure can be applied since, unlike for the horizontal case, the maximum of the vertical distribution is within the acceptance of the horizontal RPs. Here again, the resulting uncertainty is of the order of 150 μm.

3.3 Proton reconstruction

3.3.1 The LHC beam optics

The reconstruction of the scattered proton momentum from the tracks measured in the RPs requires precise knowledge of the magnetic fields traversed by the proton from the IP to the RPs [42]. As mentioned earlier, this is normally parametrized in terms of the "beam optics", in which the elements of the beam line are treated as optical lenses. The proton trajectory is described by means of transport matrices, which transform the kinematics of protons scattered at the IP to the kinematics measured at the RP position. The trajectory of the protons produced at the IP (denoted by the superscript '*') with transverse vertex position (x^*, y^*) and horizontal and vertical components of scattering angle (Θ_x^*, Θ_y^*) is described approximately by:

$$\mathbf{d}(s) = T(s, \xi)\mathbf{d}^*, \tag{3.1}$$

where s indicates the distance from the IP along the nominal beam orbit, and $\mathbf{d} = \big(x, \Theta_x, y, \Theta_y, \xi\big)$, with $\xi = \Delta p/p$, and p and Δp the nominal beam momentum and the proton longitudinal momentum loss, respectively. The symbol $T(s, \xi)$ denotes the single-pass transport matrix, whose elements are the optical functions. The leading term in the horizontal plane is:

$$x = D_x(\xi)\xi, \tag{3.2}$$

where the dispersion D_x has a mild dependence on ξ. In the vertical plane, the leading term reads:

$$y = L_y(\xi)\Theta_y^*, \tag{3.3}$$

where $L_y(\xi)$ is the vertical effective length. The ξ dependence of L_y is shown in Fig. 3.2. At any location s in the RP region there is a value of ξ, ξ_0, where L_y vanishes and hence the values of y concentrate around zero. Consequently, the distribution of the track impact points exhibits a 'pinch' at $x_0 \approx D_x\xi_0$, cf. Fig. 3.3. The horizontal dispersion D_x is then estimated as:

$$D_x \approx \frac{x_0}{\xi_0}. \tag{3.4}$$

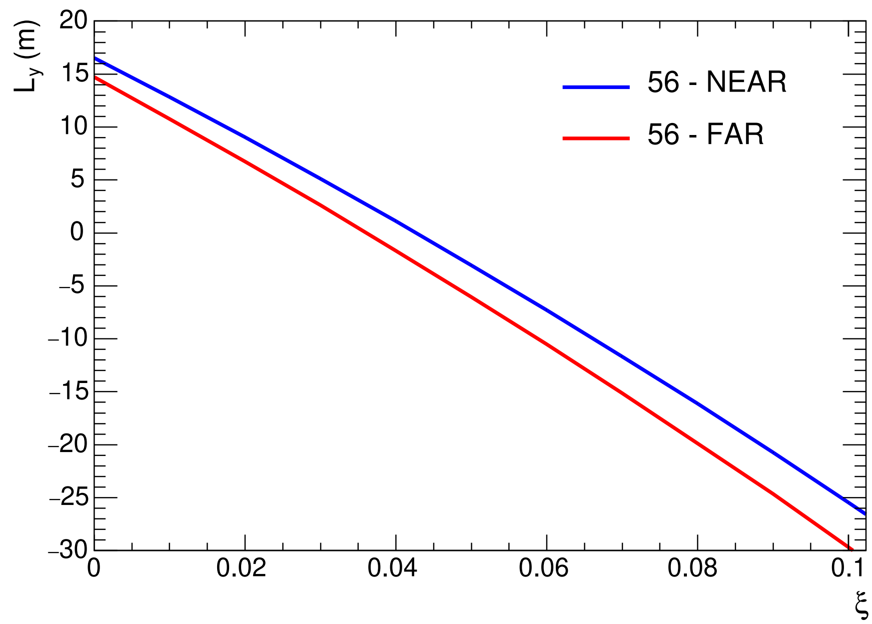

Figure 3.2: Vertical effective length L_y (in meters) as a function of the proton relative momentum loss ξ at two (near and far) RPs calculated with the beam line optics simulation program MAD-X [43].

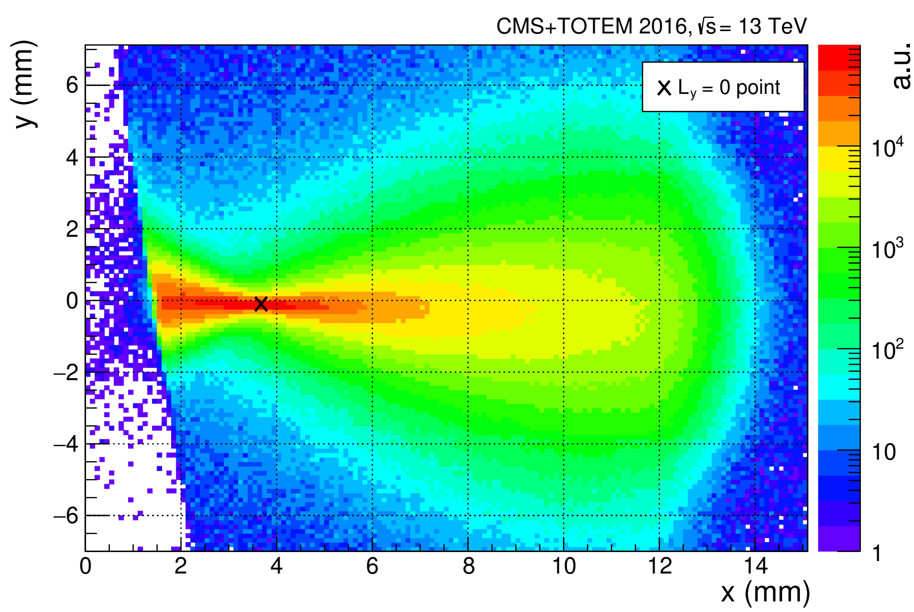

Figure 3.3: Distribution of the track impact points measured in RP 210F, in sector 45, for the alignment fill. The point where $L_y = 0$ is shown with a cross. The beam center is at $x = y = 0$. The edge of the distribution is slanted because the RP shown has a rotation of 8° with respect to the vertical.

The subleading terms neglected in this approximation are treated as systematic uncertainties.

An independent estimate of the difference of the dispersions in the two LHC beams, ΔD_x, is obtained by varying ΔD_x to find the best match between the ξ distributions reconstructed from the two arms. This estimate agrees with the one discussed above within the uncertainties.

These two horizontal dispersion measurements and the beam position values constrain the LHC optics between the IP and the RPs, including the nonlinearities of the proton transport matrices and their dependence on ξ. The optical functions are extracted with the methods originally developed for the analysis of elastic scattering data [44].

3.3.2 Proton track reconstruction

Since there is no significant magnetic field in the region of the CT–PPS RPs, the trajectory of the particles passing through the silicon strip detectors is a straight line. In each RP (RP hereinafter refers to the particle detector contained in the pot), track reconstruction therefore starts with a search for linear patterns along z among the hits detected in the 10 planes, as described in Chapter 3 of Ref. [45]. The search is performed independently in each of the two strip orientations (with angles of $+45^\circ$ and -45° with respect to the bottom of the RP); hits in at least 3 out of 5 planes are required. If only one pattern is found in both orientations, the patterns can be uniquely associated and a track fitted, yielding a “track impact point” evaluated at the center of the RP along z. Figure 3.4 shows a typical distribution of the track impact points in the (x, y) plane for a RP at $15\,\sigma$ from the beam. When there is more than one pattern in any strip orientation, a unique association is not possible and no track is reconstructed. The inefficiency due to multiple tracks depends on the pileup, and ranges between 15 and 40% in the 2016 data collected with Si strips used in the next chapter. For the 2016 data, multiple tracks inefficiency and the ξ- and time-dependent effects of radiation damage to the sensors are the dominant sources of inefficiency. Other reconstruction effects, such as those due to showers within the detector material, are estimated to contribute ≈3% to the efficiency for finding proton tracks.

The tracking CT–PPS upgrade with 3D pixel technology before the 2017 data taking allowed multiple track reconstruction, thereby drastically reducing the inefficiency.

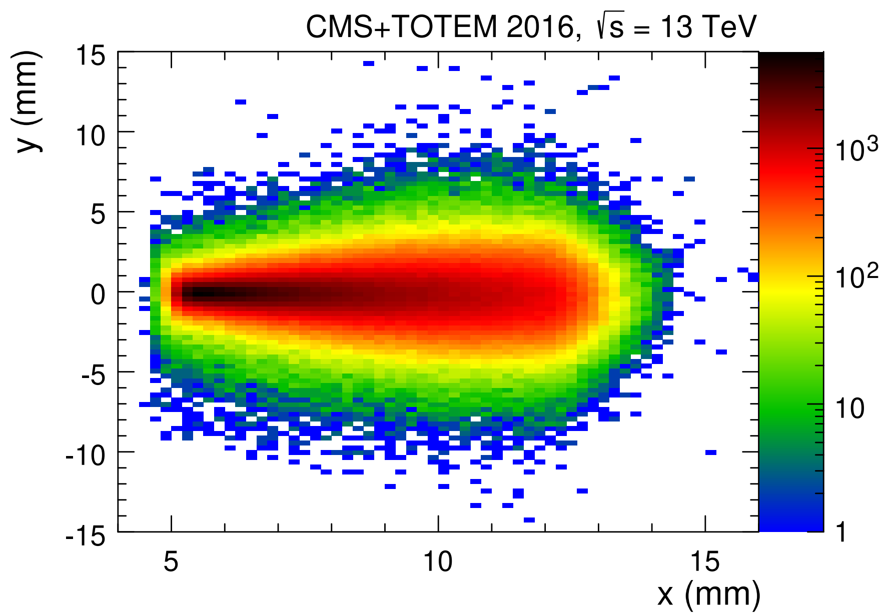

Figure 3.4: Example of track impact point distribution (in the x, y plane) measured in RP 210F, sector 45, at $15\,\sigma$ from the beam in the x direction. The beam center is at $x = y = 0$. The track selection includes a matching requirement with RP 210N, which suppresses noise and beam backgrounds, but slightly reduces the acceptance for low values of the position x, given the different acceptance of the near and far RPs.

3.3.3 Determination of ξ

The fractional momentum loss of a proton, ξ, can be determined from the track impact point in a single RP. This is advantageous in regions where the other RP of the sector does not have sufficient acceptance or is inefficient. In practice, ξ is reconstructed by inverting Eq. (3.2). This method ignores subleading terms in the proton transport (notably the one proportional to the horizontal scattering angle); their effect is included in the systematic uncertainties.

The main uncertainties are:

- dispersion calibration: relative uncertainty in D_x of about 5.5%;
- horizontal alignment: approximately 150 μm;
- neglected terms in Eq. (3.2).

For values of $\xi \gtrsim 0.04$, the leading uncertainty comes from the dispersion, and from the neglected terms related to Θ_x^* in Eq. (3.2).

Having reconstructed ξ, Eq. (3.3) can then be used to determine the vertical scattering angle from the curves presented in Fig. 3.2. The scattering angle can, in turn, be related to the vertical component of the proton transverse momentum.

Chapter 4

Analysis of the first CT–PPS data: (semi)exclusive dilepton production with proton tag

4.1 Introduction

Proton–proton collisions at the LHC provide for the first time the conditions to study the production of particles with masses at the electroweak scale via photon–photon fusion [23, 46]. Although the production of high-mass systems in photon–photon collisions has been observed by the CMS and ATLAS experiments [47–49], no such measurement exists so far with the simultaneous detection of the scattered protons. This chapter describes the measurement of the process $pp \to p\ell^+\ell^-p^{(*)}$ in pp collisions at $\sqrt{s} = 13$ TeV, where a pair of leptons ($\ell = e$, μ) with mass $m(\ell^+\ell^-) > 110$ GeV is reconstructed in the central CMS apparatus, one of the protons is detected in the CMS–TOTEM precision proton spectrometer, and the second proton either remains intact or is excited and then dissociates into a low-mass state, indicated by the symbol p^*, and escapes undetected. Such a final state receives contributions from exclusive,

$pp \to p\ell^+\ell^-p$, and semiexclusive, $pp \to p\ell^+\ell^-p^*$, processes (Fig. 4.1 left, and center). Central exclusive dilepton production is interesting because deviations from the theoretically well-known cross section may be an indication of new physics [50–52], whereas central semiexclusive processes constitute a background to the exclusive reaction when the final-state protons are not measured.

(Semi)exclusive dilepton production has been previously studied at the Fermilab TEVATRON, as mentioned above, and at the CERN LHC, but at lower masses and never with a proton tag [53–58].

Central dilepton production is dominated by the diagrams shown in Fig. 4.1, in which both protons radiate quasi-real photons that interact and produce the two leptons in a t-channel process. The left and center diagrams result in at least one intact final-state proton, and are considered as signal in this analysis. The CT–PPS acceptance for detecting both protons in "exclusive" $pp \to p\ell^+\ell^-p$ events (the left diagram) starts only above $m(\ell^+\ell^-) \approx 400$ GeV, where the standard model cross section is small. By selecting events with only a single tagged proton, the sample contains a mixture of lower mass exclusive and single-dissociation ($pp \to p\ell^+\ell^-p^*$, "semiexclusive") processes with higher cross sections. The right diagram of Fig. 4.1 is considered background, and contributes if a proton from the dissociating system is detected, or if a particle detected in CT–PPS from another interaction in the same bunch crossing (pileup), or from beam-induced background is wrongly associated with the dilepton system. A pair of leptons from a Drell–Yan process can also mimic a signal event if detected in combination with a pileup proton.

In central (semi)exclusive events, the kinematics of the dilepton system can be used to determine the momentum of the proton, and hence its fractional momentum loss ξ. Comparison of this indirect measurement of ξ with the direct one obtained with CT–PPS can be used to suppress backgrounds, as well as to provide proof of the correct functioning of the spectrometer.

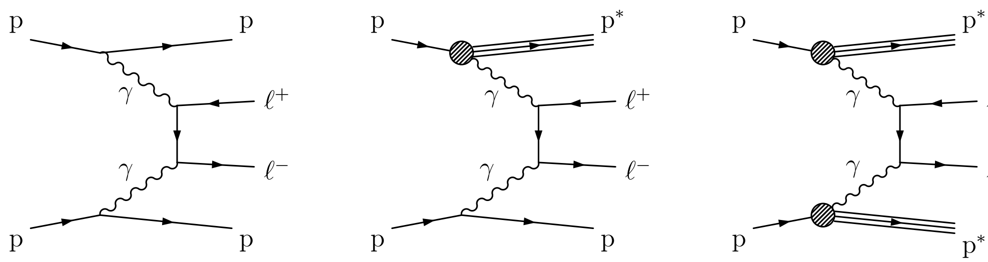

Figure 4.1: Production of lepton pairs by $\gamma\gamma$ fusion. The exclusive (left), single proton dissociation or semiexclusive (middle), and double proton dissociation (right) topologies are shown. The left and middle processes result in at least one intact final-state proton, and are considered signal in this analysis. The rightmost diagram is considered to be a background process.

The CT–PPS detector [9, 59] operated for the first time in 2016 and in this year collected a total integrated luminosity of $\sim$15 fb^{-1} in standard, high-luminosity runs of the LHC. The average number of pileup interactions per bunch crossing during 2016 was 27. For the present analysis, a sample of 9.4 fb^{-1} is used; the remaining (unused) data set was taken after September 2016, when the LHC collided protons with a different crossing angle.

4.2 Samples

4.2.1 Data

The CT–PPS data analyzed here were collected during the period May–September 2016; they correspond to an integrated luminosity of 9.4 fb^{-1}. In the same period, CMS collected a total of 15.6 fb^{-1}. For the present data, the beam amplitude function β^* at the IP was 0.4 m and the crossing angle α_x of the beams was 370 μrad. After about a month, the silicon strip detectors suffered heavy radiation damage. After new silicon strip detectors were installed in September, the LHC implemented a smaller crossing angle for collisions at the CMS IP, which resulted in different optics parameters and therefore changed the CT–PPS acceptance. These later data are not used in the present analysis.

4.2.2 Monte Carlo simulation

One way to extract information from an experiment is to compare observations with the predictions of an existing physics model. A fully analytical approach to derive predictions for such comparison is impracticable for two reasons: first, there in principle is no complete understanding of the physics, and second, the large produced multiplicities as well as the complexity of modern detectors would require enormous amounts of computational power for an analytical calculation. This calls for use of probabilistic modelling methods, usually based on Monte Carlo algorithms [60, 61] in high energy physics.

The Monte Carlo event generators are designed to generate sets of events as detailed as could be observed by a perfect detector. To predict the scattering cross section it is necessary to integrate the probability density, given by a quantum mechanical matrix element-squared, over the phase space of the process. Monte Carlo techniques are used to select all relevant variables according to the desired probability distributions, and thereby ensure (quasi-)randomness in the final events [62]. The event generation is performed sequentially: first the hard subprocess described by matrix elements is simulated. Next, the involved partons, as well as any newly produced particles with color radiate virtual gluons, which can themselves emit further gluons or produce quark-antiquark pairs, leading to the formation of parton showers. Once the simulation of the parton showers reaches the cutoff energy scale, the perturbative description of QCD evolution can no longer be used – the hadronization takes over from the parton showering, combining the particles produced during showering into hadrons, which can be either stable or decay further. In hadron-hadron collisions, the other constituent partons of the incoming hadrons undergo multiple interactions which produce the so-called underlying event.

To compare the properties of the resulting simulated events with these of the real events it is necessary to pass them through the detector simulation. Specific program packages (e.g. [63]) are designed to simulate the propagation of the final state particles through the detector, taking into account the geometry and physical properties of its material, as well as producing the detector response in terms of electric current and voltage signals. Reconstruction algorithms identical to those used for the data are then applied to the simulated detector measurements. The distributions of the resulting reconstructed physics quantities can finally be used for comparison with the data.

For the present analysis, the simulated signal samples of exclusive ($\mathrm{pp} \to \mathrm{p}\ell^+\ell^-\mathrm{p}$) and single proton dissociative ($\mathrm{pp} \to \mathrm{p}\ell^+\ell^-\mathrm{p}^*$) events proceeding via photon fusion $\gamma\gamma \to \ell^+\ell^-$ are generated with the LPAIR code [64,65] (version 4.2). LPAIR is also used to produce $\gamma\gamma \to \ell^+\ell^-$ samples with both protons exciting and dissociating, that is $\mathrm{pp} \to \mathrm{p}^*\ell^+\ell^-\mathrm{p}^*$. These three topologies are illustrated in Fig. 4.1. LPAIR accounts for the two-photon interaction process by computing the full matrix element for the $\mathrm{pp} \to \mathrm{p}\ell^+\ell^-\mathrm{p}$ diagram. The hadronic structure of the proton is then effectively taken into account by multiplying the proton charge by appropriate form factors or structure functions. For the purpose of proton dissociation into a hadronic system, LPAIR is interfaced with the Jetset library of PYTHIA 6 [66] in order to compute the kinematics of the final-state particles. Depending on the chosen structure function, the low-mass system can decay into Δ^+ and Δ^{++} resonances while the high-mass system can decay into larger multiplicity states with Δ, η, and K resonances [67]. The survival probability correction is not simulated by LPAIR (c.f Sec. 1.2 and the next section), and thus the cross section predictions should be rescaled by the factors corresponding to each process.

Background from the Drell–Yan process, $pp \rightarrow \gamma^*/Z^* \rightarrow \ell^+\ell^- + X$, is simulated with MadGraph5_aMC@NLO [68, 69], interfaced with the PYTHIA 8.212 [62] event generator using the CUETP8M1 tune [70] for parton showering, underlying event, and hadronization. At the core of MadGraph5_aMC@NLO lies the capability of computing tree-level and one-loop amplitudes for arbitrary processes. Such computations are then used to predict physical observables with different perturbative accuracies, including QCD and EW corrections to SM processes. The events for this analysis are generated at leading order, and normalized to the next-to-next-to-leading order cross section prediction [71].

The central detector information is passed through the standard GEANT4 [63] simulation of the CMS detector and reconstructed in the same way as the collision data. Conversely, only generator-level forward proton information is used, which is sufficient for the present analysis.

4.2.2.1 Rapidity gap survival probability

The characteristic signature of central production via $\gamma\gamma$ fusion is the presence of large rapidity intervals adjacent to the scattered protons devoid of particles (the so-called large rapidity gaps, LRG) in the final state. Rapidity gaps can be filled by particles originating from extra soft interactions that occur between the colliding protons. These soft interactions produce extra final-state particles, and thereby suppress the visible exclusive cross section. The factor quantifying the fraction of events in which no extra soft interactions occurred is called rapidity gap survival probability, S^2 [72]. Survival probability has to be applied to theoretical predictions neglecting soft processes in order to describe the observed yields. The S^2 values used for the present analyses are based on a recent study [73], with numerical values of 0.89 (elastic), 0.76 (single dissociation), and 0.13 (double dissociation).

4.3 Event selection and comparison of data and simulation

4.3.1 Trigger

Events were selected online [74] by requiring the presence of at least two muon or electron candidates of any charge. No requirement on forward protons was imposed online.

The dimuon candidates were triggered by the unprescaled HLT path which requires two muons with $p_T > 38$ GeV with no particle identification (ID, [75]), isolation, nor vertex requirements[1].

The dielectron candidates were triggered by the unprescaled HLT path requiring two electrons with $p_T > 33$ GeV passing loose ID criteria based on the electron candidate energy measured by the calorimeters[2] [76]. No isolation nor vertex requirements are imposed at the trigger level.

4.3.2 Central variables

Offline, the two highest-p_T leptons in the event are fitted to a common vertex using a Kalman fitter [77]. The fit is required to converge, with a vertex position consistent with collisions in CMS ($|z| < 15$ cm) and a vertex fit $\chi^2 < 10$ ($P = 0.16\%$ for 1 degree of freedom with 2 tracks). The leptons are further required to have $p_T > 50$ GeV, and to be of opposite charge. In addition the standard CMS lepton quality criteria are imposed: the muons should pass the tight muon ID, and the electrons are required to pass a multivariate electron identification (MVA) ID with 90% efficiency working point [76, 78]. No explicit isolation is required for the leptons; however, nonprompt

[1] HLT_DoubleMu38NoFiltersNoVtx_*

[2] HLT_DoubleEle33_CaloIdL_MW_*

leptons (from heavy and light hadron decays in flight) are heavily suppressed by the track multiplicity selection criteria described below.

In order to select a sample enriched in $\gamma\gamma \to \ell^+\ell^-$ events, a procedure similar to that of the TEVATRON [53, 54, 79] and Run 1 LHC analyses [47–49, 55, 57] is used.

The event is accepted if no additional tracks are found in the region within the veto distance around the dilepton vertex. No explicit requirement is imposed on the p_T or on the quality of these extra tracks. In addition, the dilepton acoplanarity ($a = 1 - \Delta\phi(\ell^+\ell^-)/\pi$) is required to be consistent with the two leptons being back-to-back in azimuth ϕ. The dilepton acoplanarity versus the distance between the closest extra track and the dilepton vertex is shown in Fig. 4.2 for muons (left) and electrons (right), for the simulated signal (blue and green dots), as well as the double-dissociation and Drell–Yan backgrounds (red and yellow dots).

In the simulation, a track veto distance of 1 mm is sufficient to keep almost all elastic and single-dissociation $\gamma\gamma \to \ell\ell$ events. However, in Run 1 analyses, it was observed that the distribution of primary vertices in z was significantly narrower in data than in the simulation. This led to an underestimated pileup density, and an underestimated probability for finding spurious tracks near the dimuon vertex. In the 2016 data a similar effect is observed (Fig. 4.3). Therefore the signal region cuts are chosen to be looser than indicated by the MC, with an extra track veto region distance of 0.5 mm. The acoplanarity requirement is chosen to be $(1 - |\Delta\phi(\mu\mu)|/\pi) < 0.009$ for the muons and $(1 - |\Delta\phi(ee)|/\pi) < 0.006$ for the electrons. This gives an expected signal/background ratio > 1 at the level of the central detector cuts (Fig. 4.4).

Finally, the invariant mass of the leptons is required to be $m(\ell\ell) > 110$ GeV. This requirement suppresses the large Z-peak region, which is expected to be dominated by Drell-Yan production (production of a massive spin-1 boson via $\gamma\gamma \to Z$ is forbidden).

Figures 4.5 and 4.6 show the distributions of the extra tracks multiplicity and acoplanarity after cuts on all central detector variables except the one plotted. Fig-

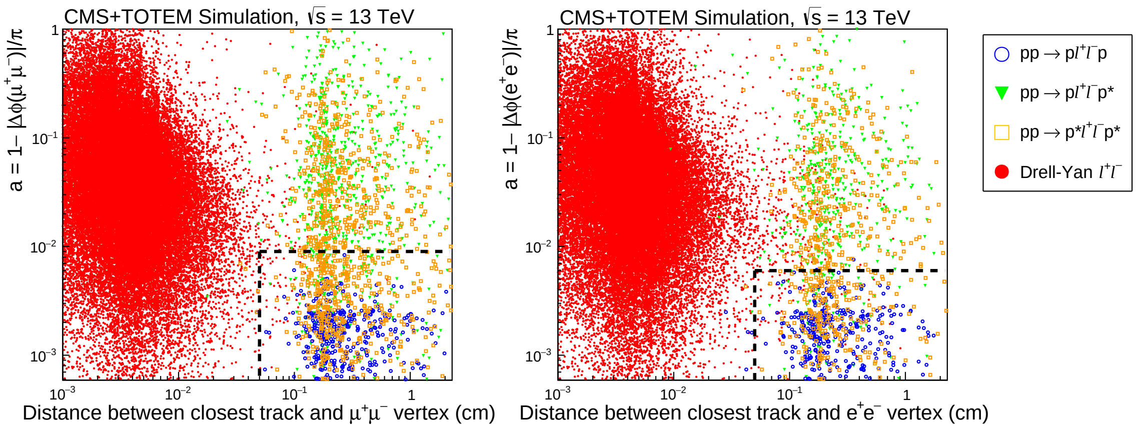

Figure 4.2: Dimuon (left) and dielectron (right) acoplanarity versus the distance between the closest extra track and the dilepton vertex for simulated signal and backgrounds. The points represent the Drell–Yan (red), exclusive $\gamma\gamma \to \ell^+\ell^-$ (blue), single-dissociative $\gamma\gamma \to \ell^+\ell^-$ (green), and double-dissociative $\gamma\gamma \to \ell^+\ell^-$ (yellow) processes. The dashed lines indicate the region selected for the analysis. The number of points for each physics process does not reflect its cross section.

ures 4.7 and 4.8 show the distributions of the dimuon and dielectron invariant mass, pair rapidity and p_T, after all central detector cuts but with no requirement on the forward protons. The simulation is normalized to the total integrated luminosity. The plots for the dimuon channel are shown with and without the "survival probability" correction factor illustrated in Sec. 4.2.2.1, which is expected to heavily suppress the double dissociation component, with a smaller suppression of the single dissociation and elastic components. As discussed earlier, the correction factors are based on Ref. [73], with numerical values of 0.89 (elastic), 0.76 (single dissociation), and 0.13 (double dissociation). There is no correction for the underestimated pileup density in the simulation, which leads to an overestimate of the track veto efficiency. Significantly fewer events are found in the data than predicted by the simulation without including these two effects in the regions with the highest expected contribution of $\gamma\gamma$ induced production (high mass, high rapidity, low p_T).

The discrepancies between the data and MC apparent in Figs. 4.5- 4.8 are not a problem for the present analysis, as the the MC is not used directly: the selection

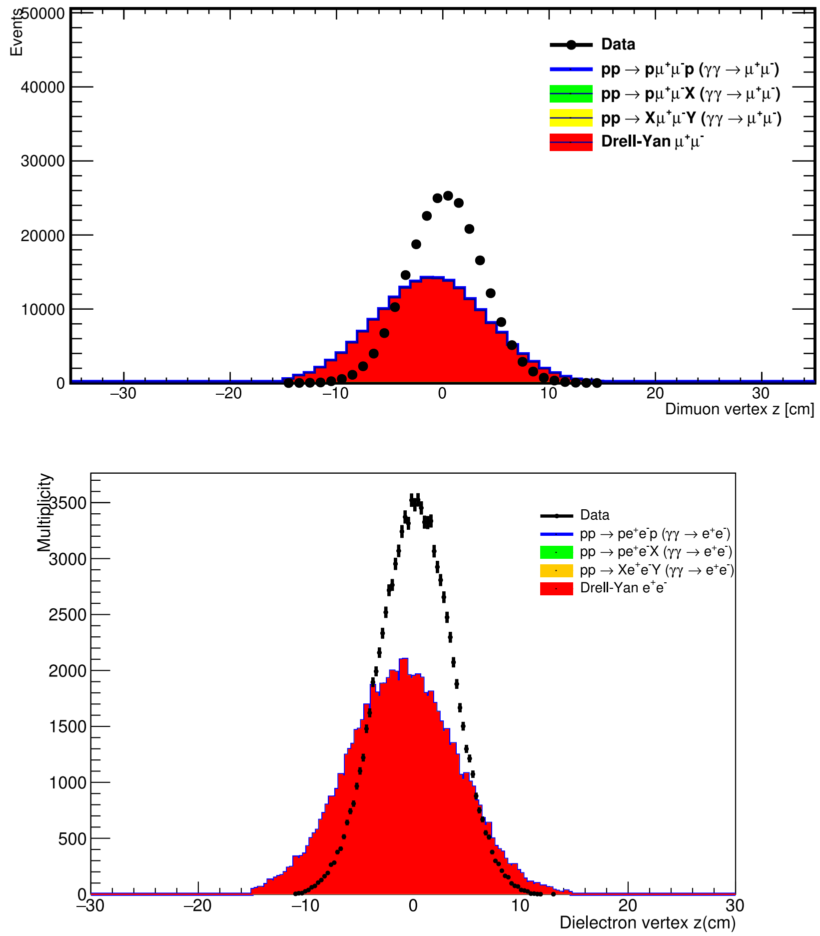

Figure 4.3: The z position of the dilepton vertex at preselection level for the dimuon sample (top) and dielectron sample (bottom).

is tuned for the pileup density observed in the data, and the background estimate is data-driven, relying only on the relative scaling factors obtained from the MC. The corresponding uncertainties are taken as contributions to the systematic uncertainty.

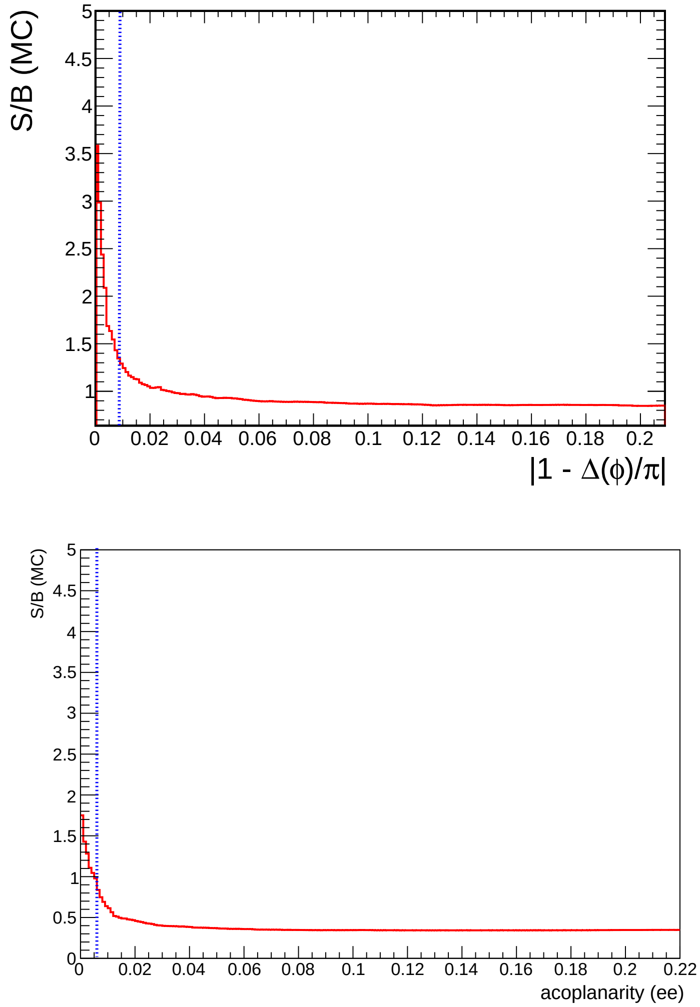

Figure 4.4: Signal/background ratio in simulation as a function of the cut on acoplanarity, with all other central detector cuts applied for the dimuon channel (top) and the dielectron channel (bottom). The vertical lines indicate the values used in the analysis.

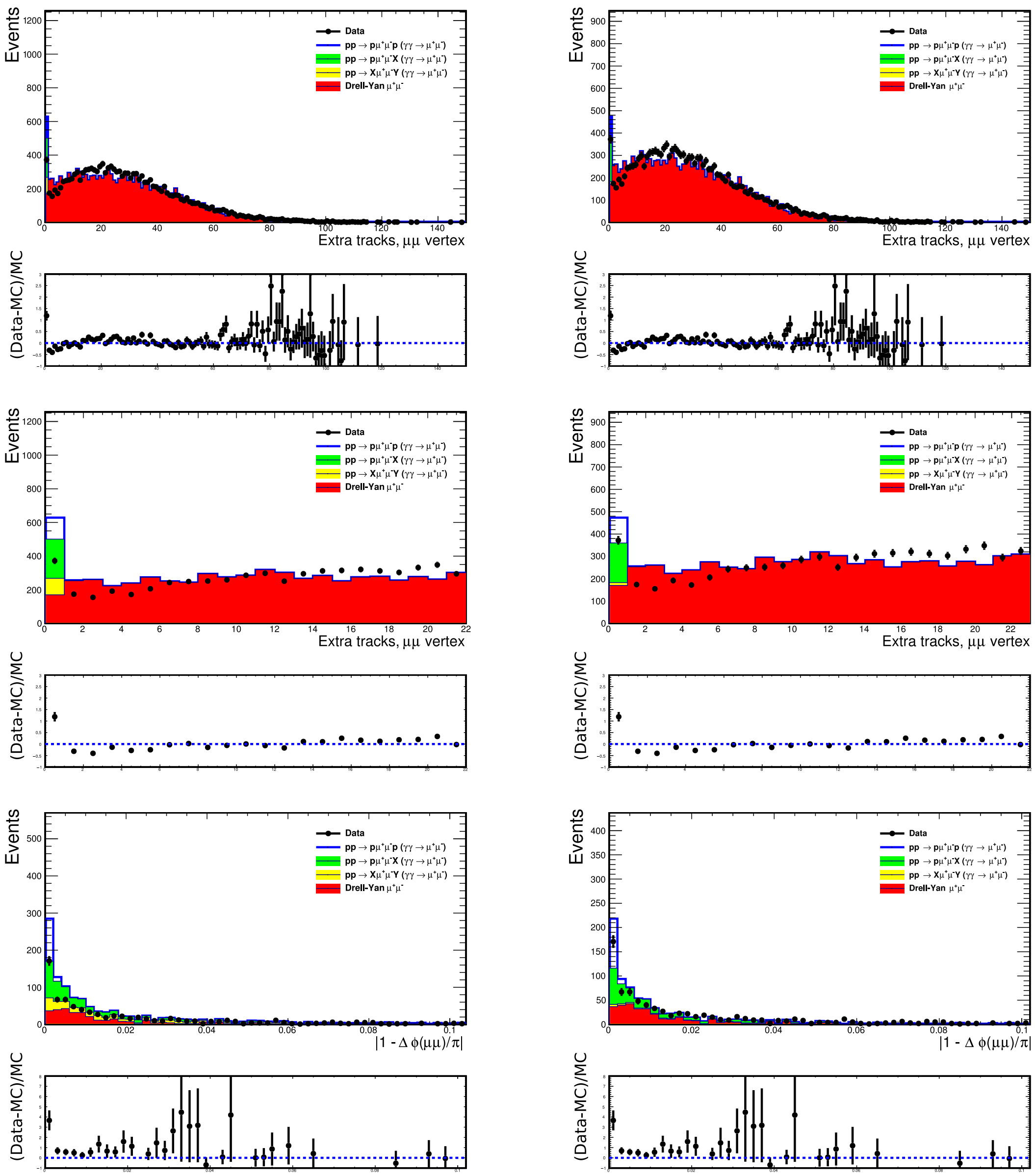

Figure 4.5: Multiplicity of extra tracks within 0.5 mm of the dimuon vertex for the full region (top), zoomed on the low multiplicity region (middle), and acoplanarity of the $\mu\mu$ pair (bottom). In the track multiplicity plots the acoplanarity < 0.009 cut is applied, while in the acoplanarity plot the cut of N(extra tracks)=0 is applied. The plots in the left column are normalized according to the default LPAIR cross sections, while the plots on the right include the additional predicted suppression of the $\gamma\gamma$ processes due to the survival probability. The lower panel in each plot shows the ratio of the data to the non-$\gamma\gamma$ exchange (Drell-Yan) background prediction, divided by the Drell-Yan background prediction.

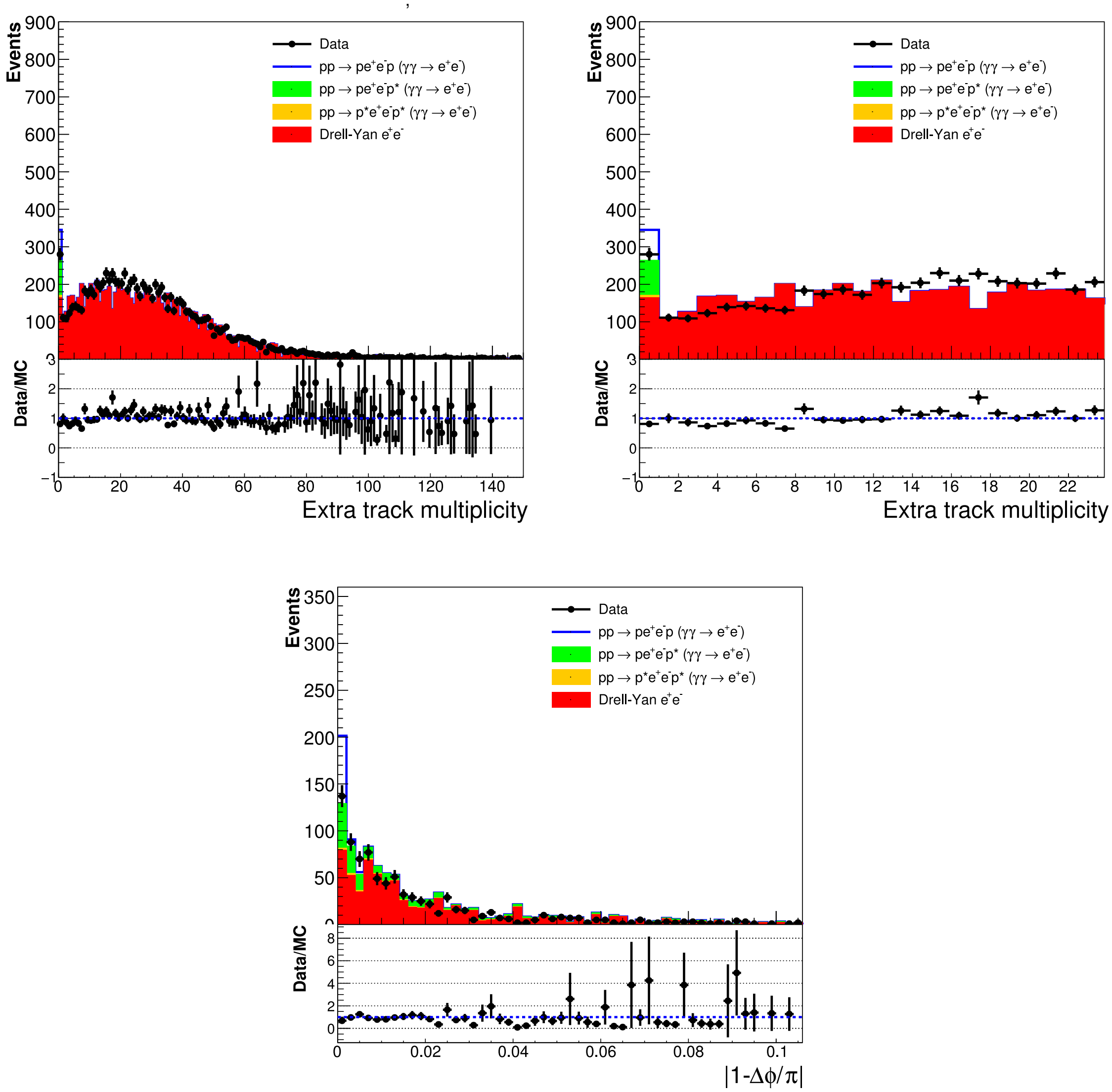

Figure 4.6: Multiplicity of extra tracks within 0.5 mm of the dielectron vertex for the full region (top left), zoomed on the low multiplicity region (top right), and acoplanarity of the *ee* pair (bottom). In the track multiplicity plots the acoplanarity < 0.006 cut is applied, while in the acoplanarity plot the cut of N(extra tracks)=0 is applied. The plots include the additional predicted suppression of the $\gamma\gamma$ processes due to the survival probability. The lower panel in each plot shows the ratio of the data to the sum of all signal and background predictions..

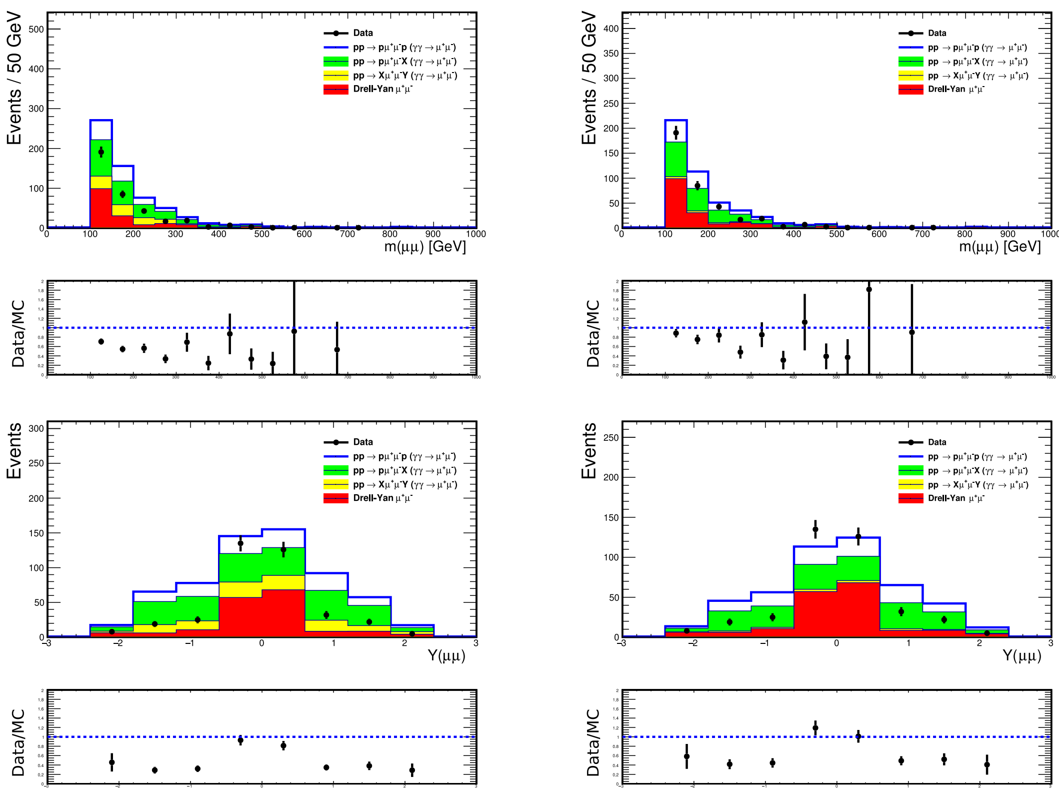

Figure 4.7: Dimuon invariant mass (top) and rapidity (bottom) distributions after all central detector selection cuts. The plots in the left column are normalized according to the default LPAIR cross sections, while the plots on the right include the predicted suppression of the $\gamma\gamma$ processes due to the survival probability. The lower panel in each plot shows the ratio of the data to the sum of all signal and background predictions.

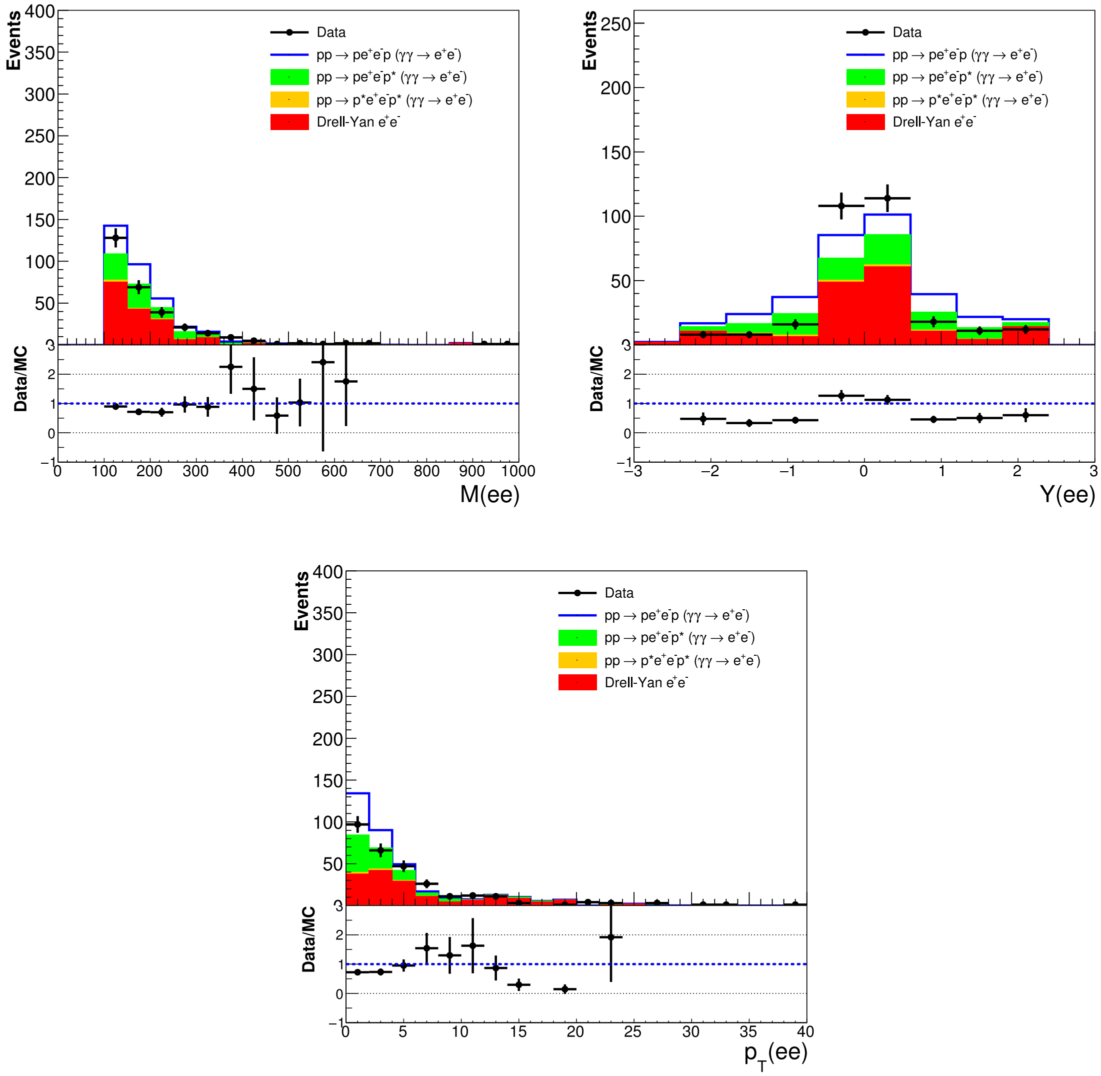

Figure 4.8: Dielectron invariant mass (top), rapidity (middle), and p_T (bottom) distributions after all central detector selection cuts. The plots include the predicted suppression of the $\gamma\gamma$ processes due to the survival probability. The lower panel in each plot shows the ratio of the data to the sum of all signal and background predictions.

4.3.3 Validation checks at the Z peak

Drell-Yan dilepton production is expected to be one of the largest backgrounds in the analysis; as discussed in Sec. 4.4, the resonant Z region is also used to derive data-driven background predictions. This section illustrates the comparison between the data and simulation for inclusive $Z \to \ell^+\ell^-$ events, in order to validate the lepton selection. Events are selected by applying all the standard analysis cuts, except that the invariant mass is required to be in the range $80 - 110$ GeV and no requirement is imposed on the multiplicity of extra tracks at the dilepton vertex. Figures 4.9 and 4.10 show data vs. simulation for the single muon and electron p_T and η distributions, respectively. Figures 4.11 and 4.12 shows similar comparison for the dimuon and dielectron invariant mass, rapidity, p_T, and acoplanarity distributions. No corrections to the lepton efficiency or momentum scale are applied. Approximately 7-8% more events are found in the data than in the MC for both channels, with the largest excesses at mid-rapidity and high $p_T(\ell)$.

Because the Z mass is $\sim$ 90 GeV, a Z produced with $p_T(Z) = 0$ will result in two leptons with $p_T(\ell) \sim 45$ GeV. The nominal offline cut of $p_T = 50$ GeV therefore strongly reduces the statistics of $Z \to \ell^+\ell^-$ events. The lepton p_T cut also affects the dilepton pair distributions, yielding a rise in the dilepton invariant mass distribution above 100 GeV, and in the acoplanarity starting near 0.3. These features in the data are well reproduced in the MC. Figures 4.13 and 4.14 show the same plots with the muon p_T cut reduced to 40 GeV, just above the trigger threshold of 38 GeV, to illustrate the effect of the lepton p_T selection. In this case the data are $\sim$ 6% below the MC, with the deficit localized in the forward region of CSC-only coverage ($|\eta| > 1.6$). Similar plots for dielectrons are shown in Fig. 4.15 and 4.16, with a deficit in the data of about $\sim$ 3%, localized mostly in the forward region. The CSCs are used in the endcap disks region where the magnetic field is uneven and particle rates are high, which causes some mismodelling in the MC.

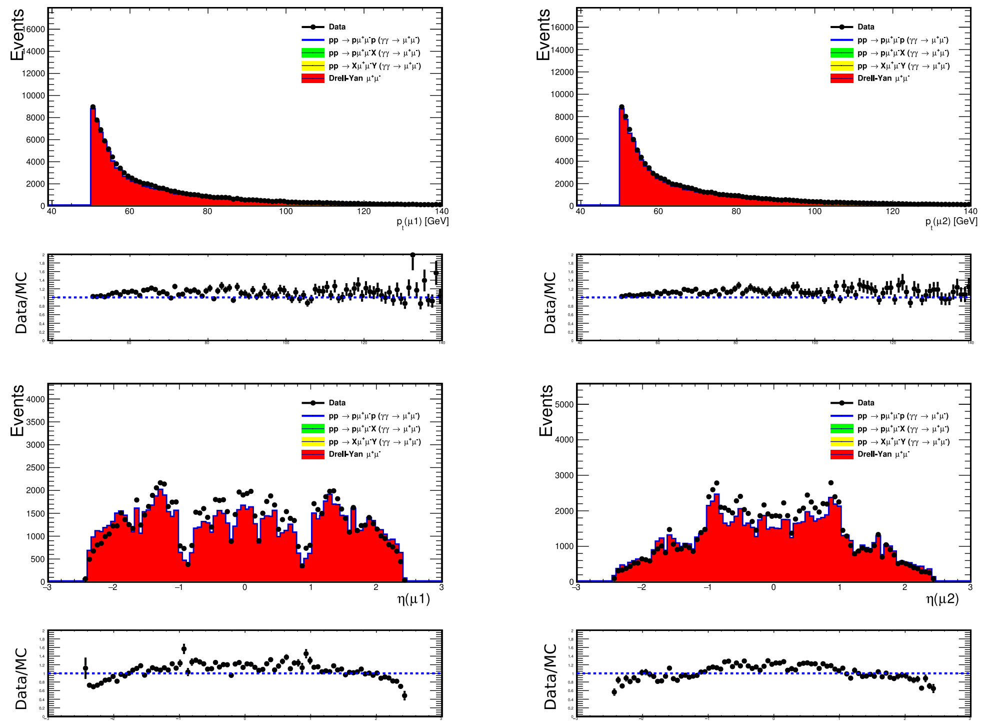

Figure 4.9: Transverse momenutm of the leading (top left) and subleading (top right) muon, pseudorapidity of the leading (bottom left), and subleading (bottom right) muon for dimuons in the Z peak region. The invariant mass is required to be between 80 and 110 GeV, with no requirement on the extra tracks multiplicity. The muon p_T is required to be above 50 GeV.

The comparison above shows that the MC reproduces the main features of the data, and specifically the dilepton mass shape distortion due to the trigger threshold, as well as the detector geometry. There are however discrepancies of the order of several percent, which do not have an impact on the final results: the Drell–Yan MC is used only to derive the relative scaling factor for the background estimate. The discrepancies in the dilepton distributions that affect the dilepton ξ spectra are included in the systematic uncertainties.

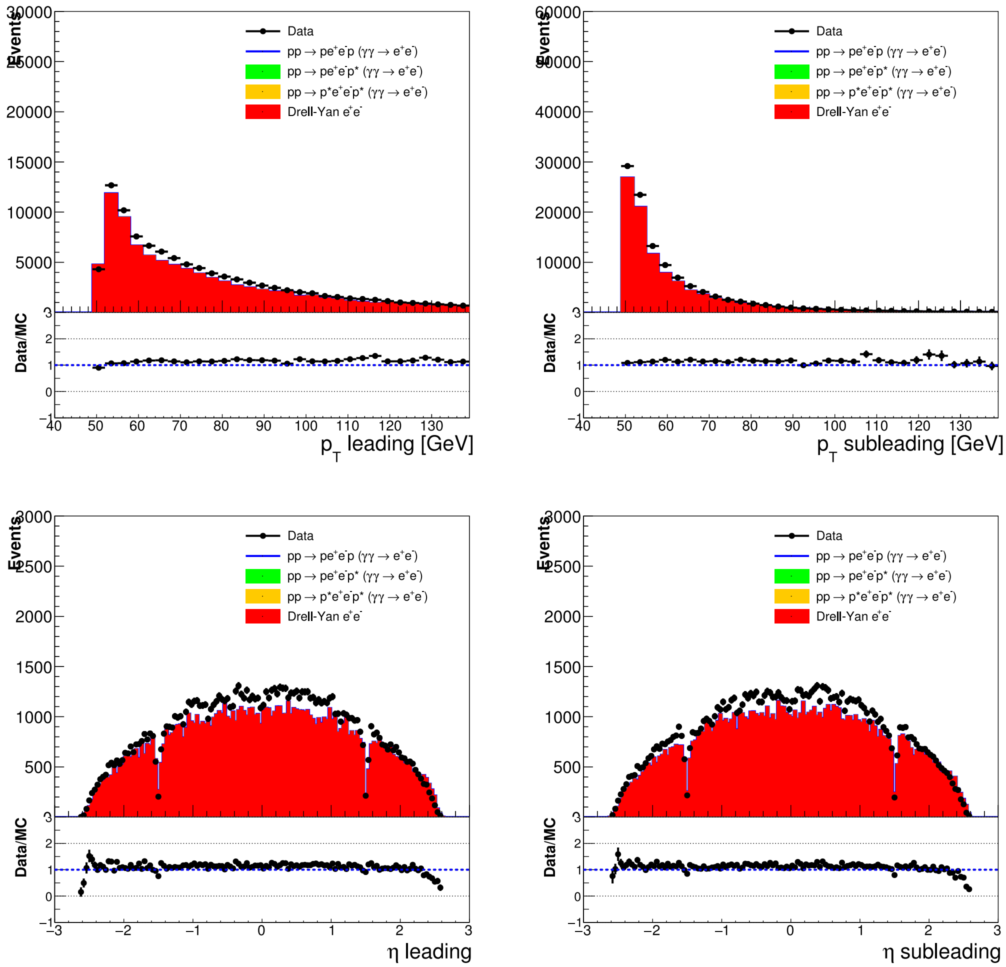

Figure 4.10: Transverse momenutm of the leading (top left) and subleading (top right) electron, pseudorapidity of the leading (bottom left), and subleading (bottom right) electron for dielectrons in the Z peak region. The invariant mass is required to be between 80 and 110 GeV, with no requirement on the extra tracks multiplicity. The electron p_T is required to be above 50 GeV.

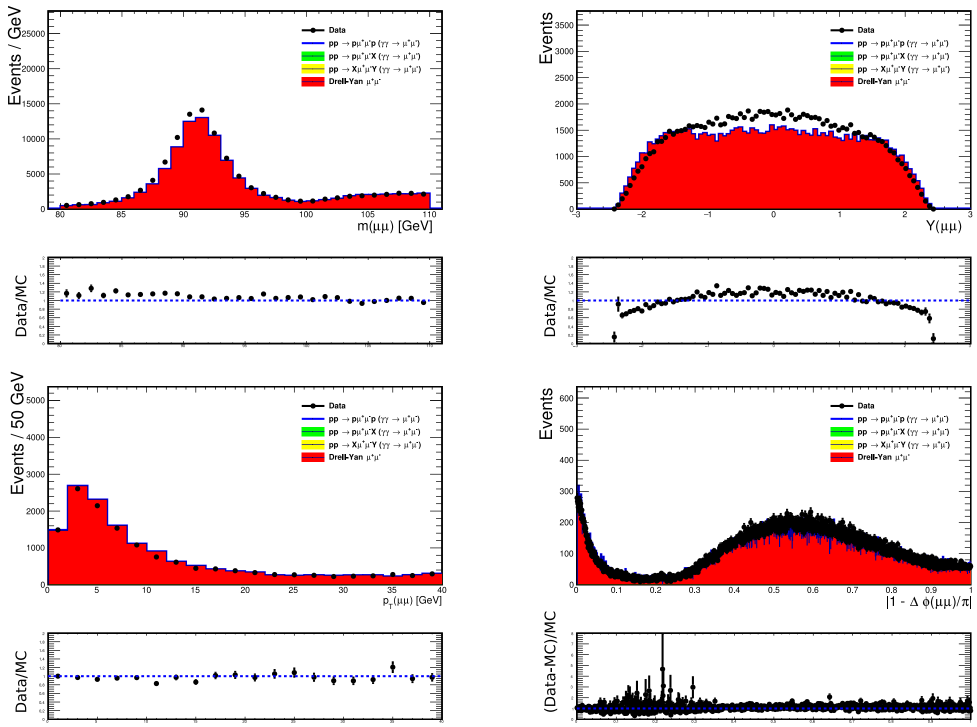

Figure 4.11: Invariant mass (top left), pair rapidity (top right), pair transverse momentum (bottom left), and acoplanarity (bottom right) distribution for dimuons in the Z peak region. The invariant mass is required to be between 80 and 110 GeV, with no requirement on the extra tracks multiplicity. The muon p_T is required to be above 50 GeV.

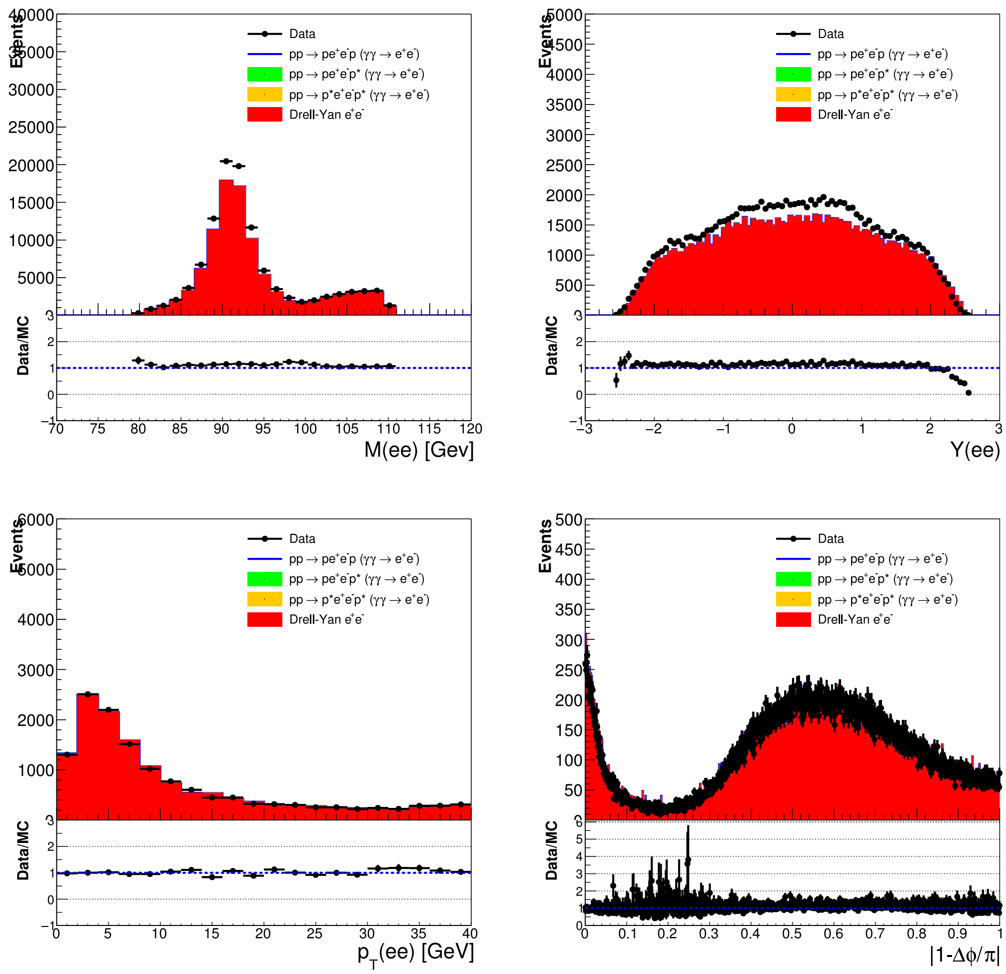

Figure 4.12: Invariant mass (top left), pair rapidity (top right), pair transverse momentum (bottom left), and acoplanarity (bottom right) distributions for dimuons in the Z peak region. The invariant mass is required to be between 80 and 110 GeV, with no requirement on the extra tracks multiplicity. The muon p_T is required to be above 50 GeV.

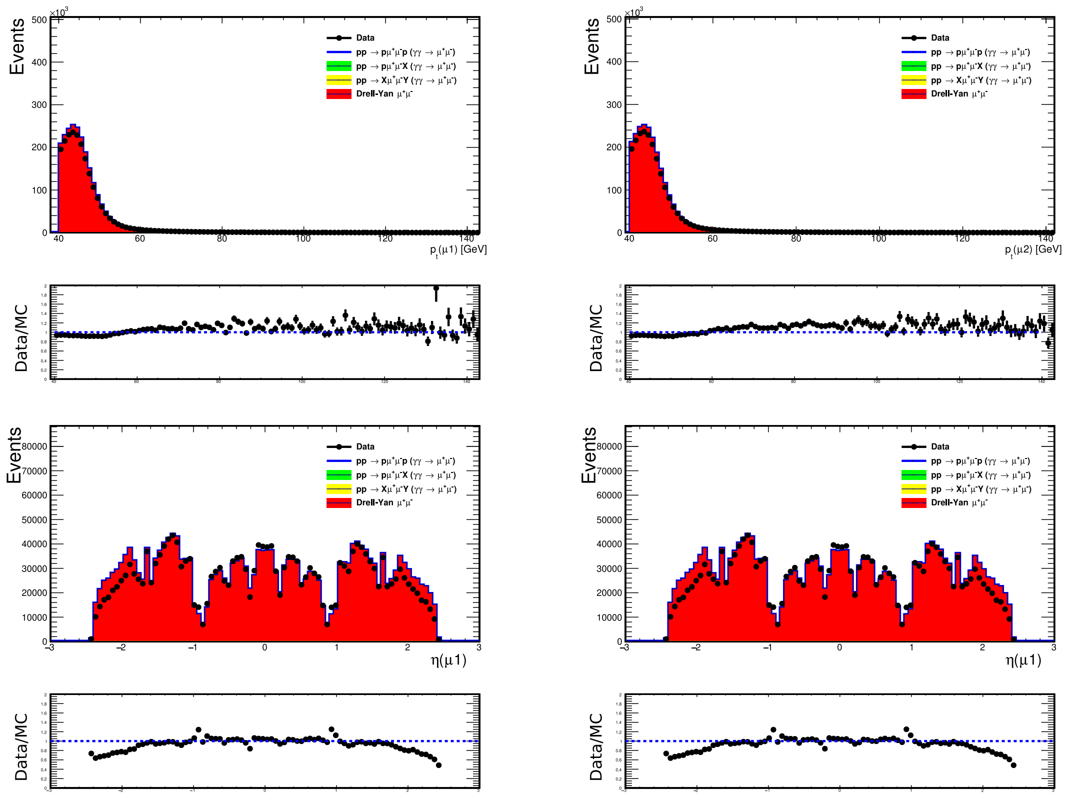

Figure 4.13: Transverse momenutm distribution of the leading (top left) and subleading (top right) muon, pseudorapidity distribution of the leading (bottom left), and subleading (bottom right) muon for dimuons in the Z peak region. The invariant mass is required to be between 80 and 110 GeV, with no requirement on the extra tracks multiplicity. The muon p_T is required to be above 40 GeV.

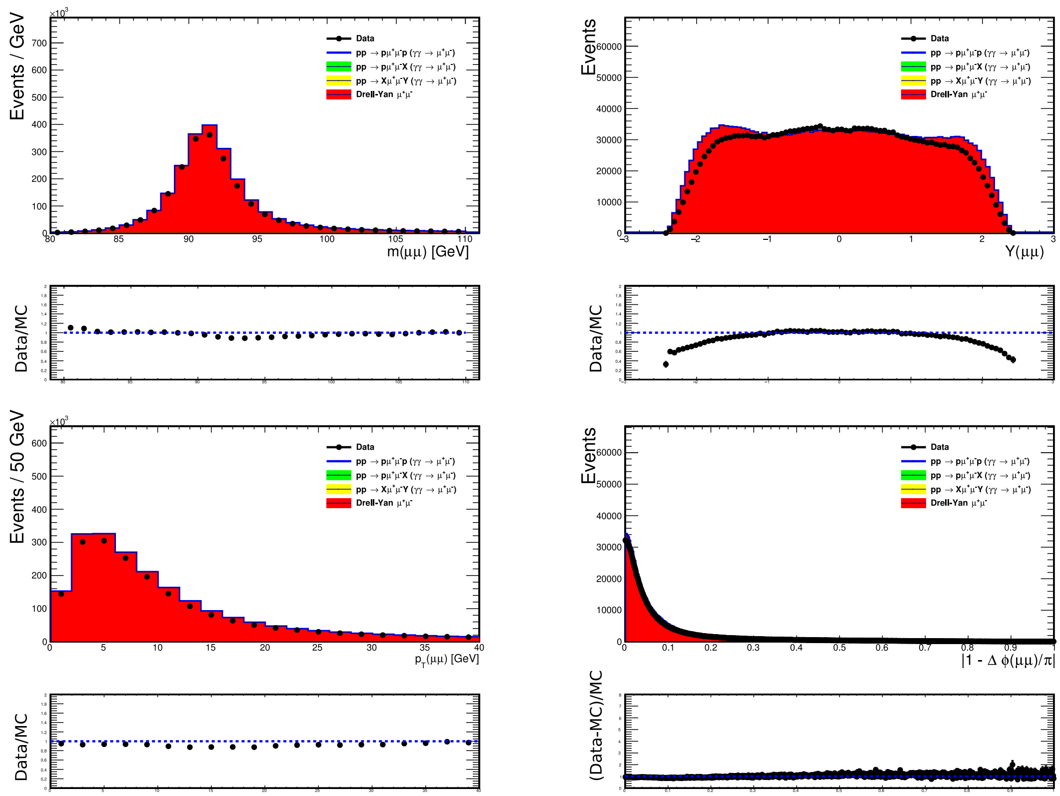

Figure 4.14: Invariant mass (top left), pair rapidity (top right), pair transverse momentum (bottom left), and acoplanarity (bottom right) distribution for dimuons in the Z peak region. The invariant mass is required to be between 80 and 110 GeV, with no requirement on the extra tracks multiplicity. The muon p_T is required to be above 40 GeV.

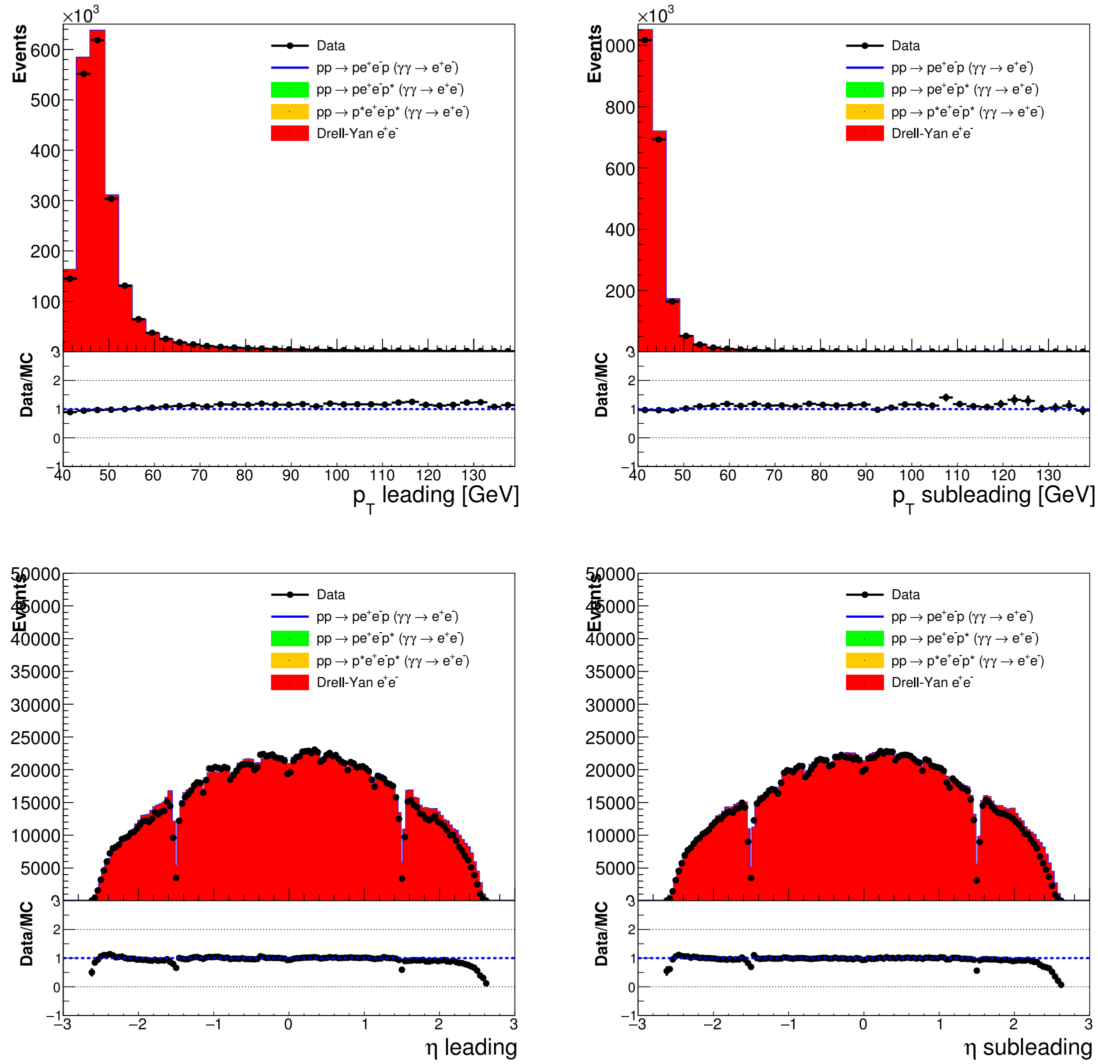

Figure 4.15: Transverse momentum distribution of the leading (top left) and subleading (top right) electron, pseudorapidity distribution of the leading (bottom left), and subleading (bottom right) electron for dielectrons in the Z peak region. The invariant mass is required to be between 80 and 110 GeV, with no requirement on the extra tracks multiplicity. The electron p_T is required to be above 40 GeV.

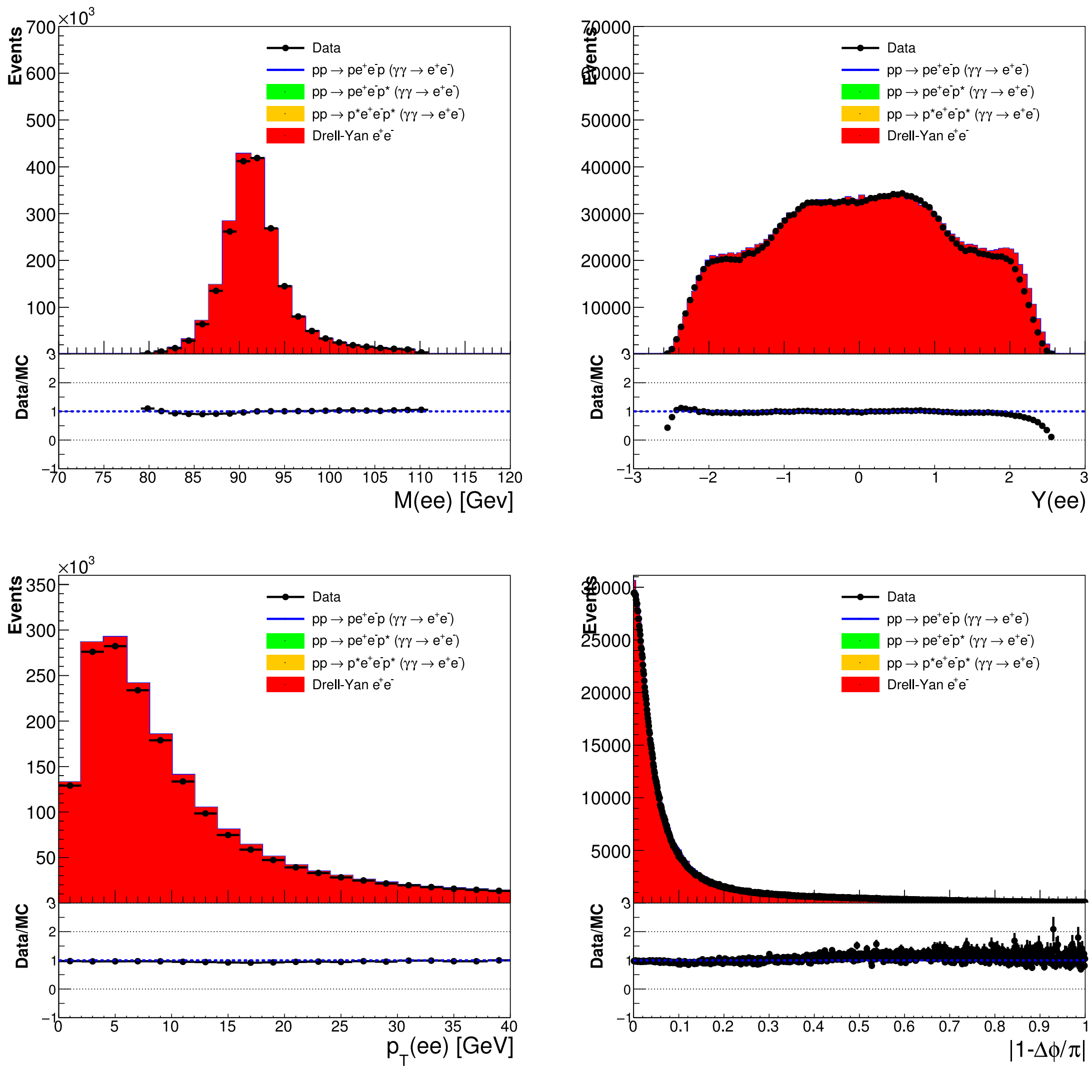

Figure 4.16: Invariant mass (top left), pair rapidity (top right), pair transverse momentum (bottom left), and acoplanarity (bottom right) distribution for dielectrons in the Z peak region. The invariant mass is required to be between 80 and 110 GeV, with no requirement on the extra tracks multiplicity. The electron p_T is required to be above 40 GeV.

4.3.4 Kinematic dependence of survival probability

The survival probability corrections [73] are defined for $|Y| = 0$, but are applied for all rapidities. As shown in Figs. 4.7 and 4.8, the data are well reproduced by the simulation with survival probability corrections in the mid-rapidity bins, but are significantly below the prediction at higher rapidities and higher masses. Several recent models predict a mild decrease of the survival probability as a function of rapidity and/or mass for elastic two-photon processes [80–82], but do not consider proton dissociation processes where the suppression could be larger.

To test this possibility, a template fit is performed to the acoplanarity distribution in slices of dimuon rapidity, after all central detector selection cuts. The Drell-Yan contribution is fixed to the nominal value, while the elastic and proton dissociation components are allowed to float freely. The only uncertainties considered are the statistical uncertainty of the data, and that of the MC templates used in the fit. The fits are performed with the TFractionFitter class of ROOT. Because of the limited statistics, only 2 bins in rapidity ($0 < |Y| < 0.6$ and $0.6 < |Y| < 2.4$) are used, and the single- and double-dissociation processes are combined into a single histogram. The fit returns an estimate for the survival probability for the elastic process, and for the effective survival probability of the single- and double-dissociation components combined.

Table 4.1 lists the results of the fitted elastic and proton dissociation components in the two rapidity bins. At mid-rapidity, the fitted survival probability for the elastic component is in good agreement with the theoretical predictions. In the forward region, the central value of the elastic component is below the mid-rapidity value, though the two are consistent within $\sim 1\sigma$. For the proton dissociation component, the best-fit value in the forward region is $\sim 3\sigma$ below the best-fit value at mid-rapidity, consistent with a kinematic dependence of the survival probability. Figure 4.17 shows the post-fit comparison of data with the fit result in the acoplanarity distribution.

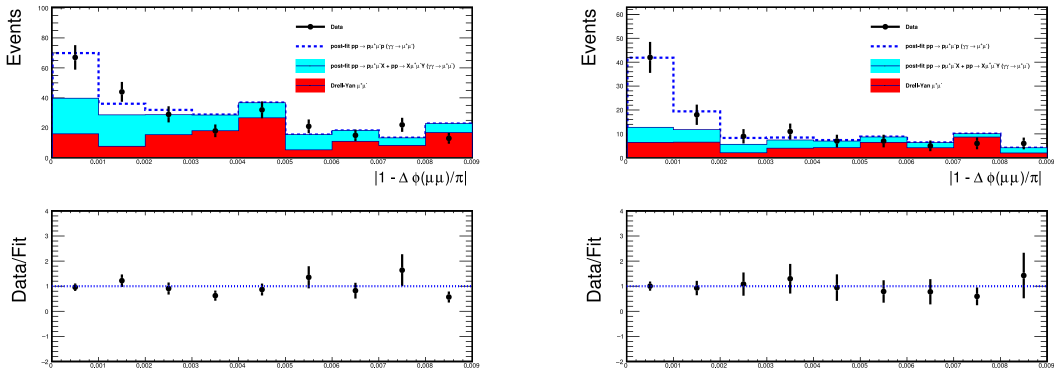

Figure 4.17: Best-fit acoplanarity distributions after all central detector selections, for $0 < |Y| < 0.6$ (left) and $0.6 < |Y| < 2.4$ (right). The upper panels show the data compared to the fitted contribution of Drell-Yan, single- plus double-dissociation $pp \to p^*\mu^+\mu^-p^{(*)}$, and elastic $pp \to p\mu^+\mu^-p$ processes. The Drell-Yan contribution is fixed to the nominal prediction, while the elastic and dissociation components are allowed to float freely. The lower panels show the ratio of the data to the fit result.

Figure 4.18 shows the invariant mass and rapidity distributions of Fig. 4.7, using the fitted $\gamma\gamma \to \mu\mu$ contributions in place of the theoretical predictions.

The survival probability correction affects the results of the present analysis only as a normalization factor for the double dissociative background contribution. The theoretical value of $S^2 = 0.13$ is used as the nominal. As illustrated above, this may overestimate the survival probability at the large rapidities, leading to an overestimate of the background. The nominal background estimate is thus conservative. The uncertainty on S^2 is taken as a contribution to the systematic uncertainty.

Rapidity range	Elastic (prediction, $\lvert Y \rvert < 0.5$)	Elastic (fit result)	Single-diss. (prediction, $\lvert Y \rvert < 0.5$)	Double-diss. (prediction, $\lvert Y \rvert < 0.5$)	Diss. (fit result)
$0 < \lvert Y \rvert < 0.6$	0.89	0.81 ± 0.38	0.76	0.13	0.86 ± 0.23
$0.6 < \lvert Y \rvert < 2.4$	0.89	0.54 ± 0.17	0.76	0.13	0.14 ± 0.07

Table 4.1: Rapidity dependence of survival probabilities based on fits to the acoplanarity distribution, in two regions of Y. The theoretical predictions for $|Y| < 0.5$ are shown, compared to the best-fit values from data, assuming no other deviations from the MC prediction.

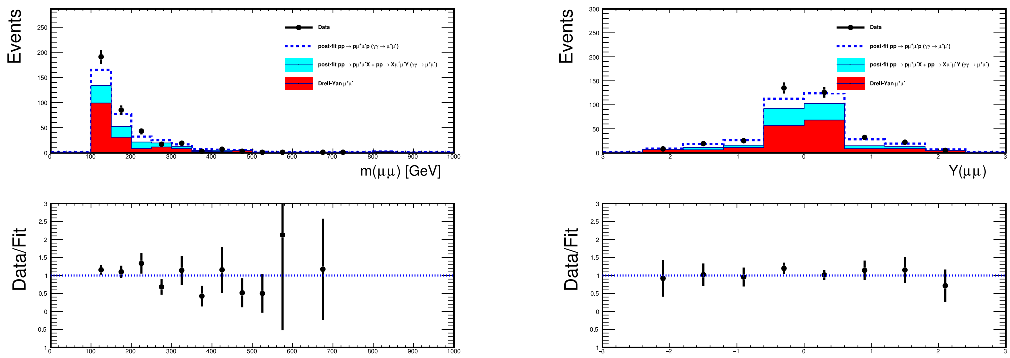

Figure 4.18: Dimuon invariant mass (left) and rapidity (right), after normalizing to the best-fit yield for elastic and dissociation contributions in the acoplanarity distribution in two bins of rapidity. The upper panels show the data compared to the fitted contribution of Drell-Yan, single- plus double-dissociation, and elastic contributions. The lower panels show the ratio of the data to the fit result.

4.3.5 Matching central and proton variables

The events selected as described in Sec. 4.3, with at least one well-reconstructed proton track in CT–PPS are retained for further analysis. For each event, the value of the fractional momentum loss of the scattered proton is estimated from the leptons as:

$$\xi(\ell^+\ell^-) = \frac{1}{\sqrt{s}} \left[p_T(\ell^+)^{\pm\eta(\ell^+)} + p_T(\ell^-)^{\pm\eta(\ell^-)} \right], \tag{4.1}$$

where the two solutions for $\pm\eta$ correspond to the protons moving in the $\pm z$ direction.

The formula is exact for exclusive events, but holds also for the single-dissociation case, as illustrated with LPAIR simulated events in Fig. 4.19; in this case only one of the two possible solutions will correspond to the direction of the intact proton. Studies with LPAIR indicate that a mass of the dissociating system larger than about 400 GeV is needed in order to produce a deviation comparable to the expected $\xi(\ell^+\ell^-)$ resolution of about 3% (4%) for dimuons (dielectrons). The latter is obtained from simulation, with an additional smearing to account for residual data–simulation differences (see Sec. 4.3.6). The LPAIR simulation also indicates that the minimum mass of the dissociating system required to generate activity in the CMS tracker is about 50 GeV; the fraction of dissociative events above this threshold is of a few percent.

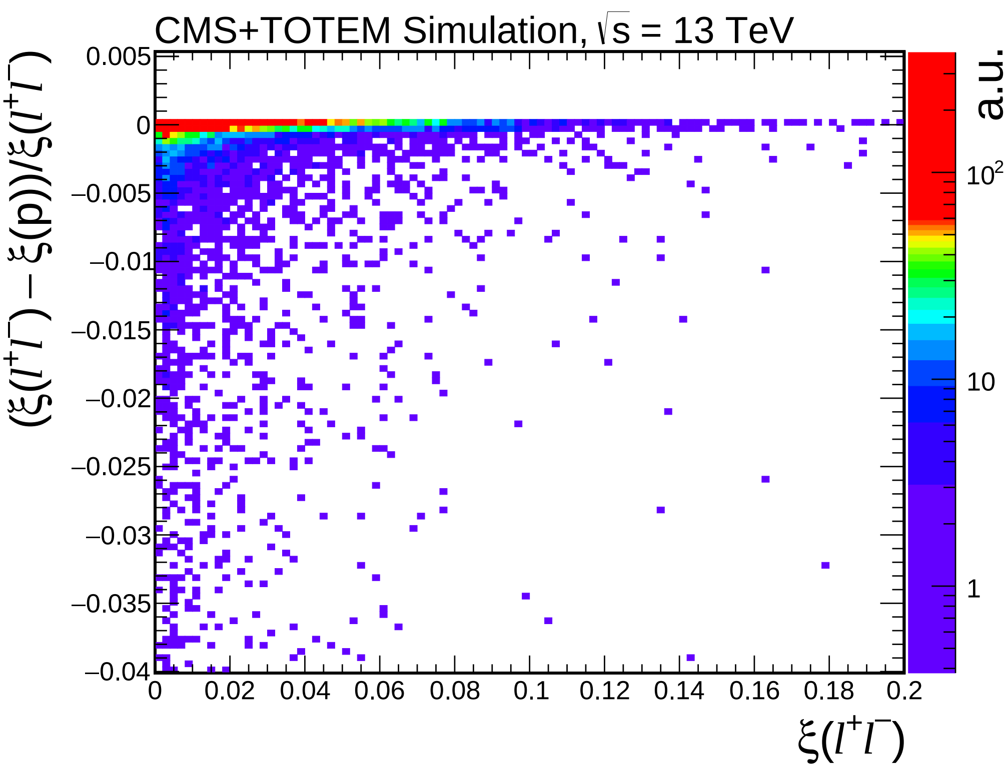

Figure 4.19: Generator-level relative difference $(\xi(\ell^+\ell^-) - \xi(\mathrm{p}))/(\xi(\ell^+\ell^-))$ vs. $\xi(\ell^+\ell^-)$ for simulated single dissociative $\to \ell^+\ell^-$ events. Of the two possible solutions for $\xi(\ell^+\ell^-)$, only the one corresponding to the side with the intact proton is shown.

To be considered as signal candidates, events are further required to have a value of $\xi(\ell^+\ell^-)$ within the CT–PPS coverage. The minimum value of ξ observed in an inclusive sample of dilepton-triggered events, with no selection to enhance $\gamma\gamma$ production, is used. Numerically this corresponds to:

- sector 45, RP 210N: $\xi > 0.033$,
- sector 45, RP 210F: $\xi > 0.024$,
- sector 56, RP 210N: $\xi > 0.042$,

- sector 56, RP 210F: $\xi > 0.032$.

The difference between the ξ coverage in the sectors 45 and 56 is due to the asymmetric beam optics.

For the events with a proton predicted to be within the acceptance, the signal region is defined by requiring $\xi(\ell\ell)$ and $\xi(\mathrm{RP})$ to match within 2σ of the combined uncertainty on $\xi(\ell^+\ell^-)$ and D_x, where the combined uncertainty is calculated by summing the $\xi(\ell\ell)$ and $\xi(\mathrm{RP})$ resolution uncertainties in quadrature. This matching window is expected to contain $\sim 95\%$ of signal events, while rejecting $80 - 90\%$ of backgrounds.

4.3.6 Resolution on $\xi(\ell\ell)$

The expected event-by-event resolution on the value $\xi(\ell\ell)$, i.e. the value of ξ obtained from the leptons, is shown in Fig. 4.20 for simulated dimuon events and Fig. 4.21 for dielectron events. The resolution estimate is obtained from the simulated signal samples, corrected for the muon and electron momentum scale and resolution. The signal samples used are generated with LPAIR, in the elastic ($pp \to p\ell\ell p$) and single proton-dissociation ($pp \to p\ell\ell X$) topologies. An additional η-dependent smearing of the muon momentum and electron momentum is applied to account for the difference in resolution between data and MC, based on values derived from the studies of $Z \to \ell\ell$ events in the full 2016 dataset. The resulting $\xi(\mu\mu)$ and $\xi(ee)$ values are compared with the generator-level ξ of the proton for each of the two samples (elastic and single proton-dissociation), with a generator-level requirement of $\xi(p) > 0.03$, corresponding to the approximate limit for the RP station with the best acceptance. Since the precise mix of elastic and single proton-dissociation events in the data is unknown, the larger RMS of the two is taken as a bound on the event-by-event $\xi(\ell\ell)$ resolution, resulting in a value of 3.3% for $\xi(\mu\mu)$ and 3.9% for $\xi(ee)$.

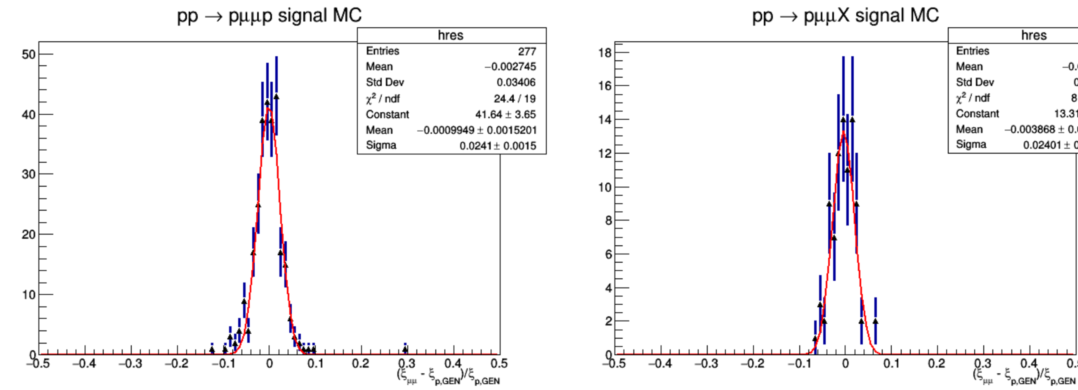

Figure 4.20: Resolution of $\xi(\mu\mu)$, $(\xi(\mu\mu) - \xi(p, GEN))/\xi(p, GEN)$ calculated from the muon kinematics in signal MC, for $\xi(p) > 0.03$, corresponding to the minimum CT–PPS Roman Pot acceptance. Left: elastic $pp \to p\mu\mu p$. Right: single proton-dissociation $pp \to p\mu\mu X$.

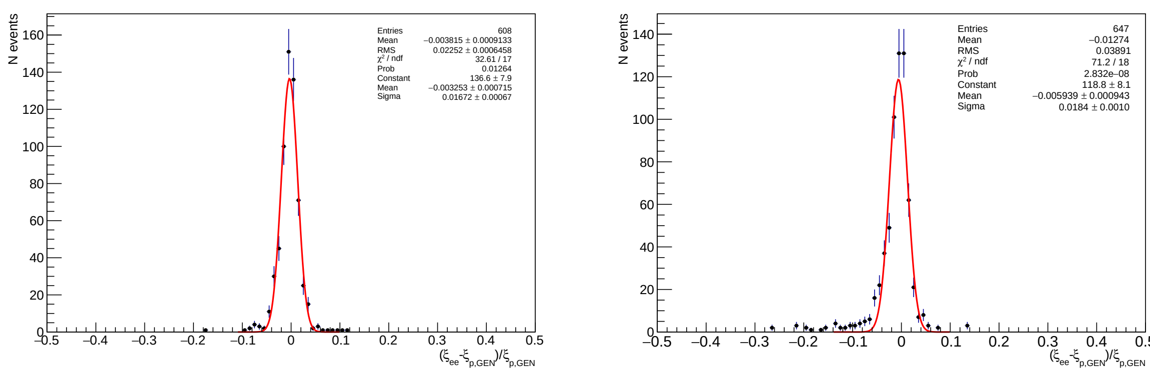

Figure 4.21: Resolution of $\xi(ee)$, $(\xi(ee) - \xi(p, GEN))/\xi(p, GEN)$ calculated from the electron kinematics in signal MC, for $\xi(p) > 0.03$, corresponding to the minimum CT–PPS Roman Pot acceptance. Left: elastic $pp \to peep$. Right: single proton-dissociation $pp \to peeX$.

4.4 Backgrounds

After the selection steps above, the backgrounds are expected to arise mainly from prompt $\ell^+\ell^-$ production in the central detectors, combined with proton tracks from unrelated pileup interactions or beam backgrounds in the same bunch crossing. The largest sources of prompt $\ell^+\ell^-$ production without leading protons are the Drell-Yan process, and $\gamma\gamma \to \ell^+\ell^-$ production in which both protons dissociate.

To estimate both the Drell-Yan and dissociative background control samples of $Z \to \mu^+\mu^-$ and $Z \to e^+e^-$ events are used. To avoid statistical correlations between the two predictions, only every second event from the sample is considered for the Drell-Yan prediction, and the remaining part for the double-dissociative background estimate. The factor two introduced by this splitting is taken into account for the final normalization.

4.4.1 Drell-Yan background

In order to estimate the Drell-Yan background from the data, the track multiplicity and acoplanarity criteria are removed, and an invariant mass window of $80 < m(\ell^+\ell^-) < 110$ GeV is selected, resulting in a high purity sample of Drell-Yan events.The Roman Pot data are then examined in these events to obtain the number of events with a proton track matching the kinematics of the $\ell^+\ell^-$ pair. Finally, simulated Drell-Yan samples, produced with the MadGraph5_aMC@NLO [68] generator interfaced to the CUETP8M1 tune [70] of PYTHIA 8 [62] for hadronization and showering, are used to extrapolate to the number of such events expected after the track multiplicity and acoplanarity selections. This allows to account for the differences in track multiplicity distributions expected at masses above the Z peak (Fig. 4.22). The scaling factor (SF) used for the extrapolation is derived from the number of MC events:

$$\mathrm{SF} = \frac{N(\text{passing track veto \& acoplanarity cuts})_{\mathrm{M}>110}}{N(\text{all})_{80<\mathrm{M}<110}}.$$

The factor SF equals $17.14 \cdot 10^{-4}$ for the dimuon channel and $16.90 \cdot 10^{-4}$ for the dielecron one.

An additional correction must be applied to account for differences in the shape of the Drell-Yan $\xi(\ell\ell)$ distribution between the Z-peak control region and the signal region. While the acoplanarity and invariant mass cuts have a small effect on the $\xi(\ell\ell)$

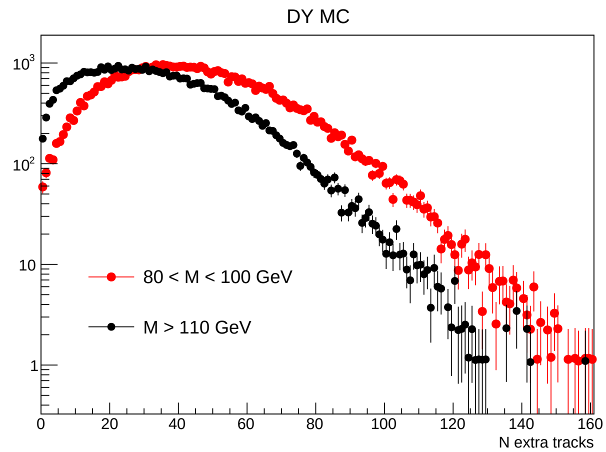

Figure 4.22: Number of extra tracks in Drell-Yan dimuon MC events for two mass regions: $80 < M < 110$ and $M > 110$, without acoplanarity cut.

shape in the simulation, the extra tracks veto affects it more significantly (Fig. 4.23). By using a fixed track veto size, DY background events are more likely to pass the selection if the leptons are at mid-rapidity, where the x, y position of the vertex is less well resolved (Fig. 4.24 and Fig. 4.25). Via Eq.(4.1), this results in an enhancement of the DY backgrounds near $\xi(\ell\ell) \sim 0.008$, falling with increasing lepton p_T. In order to account for this, the final DY $\xi(\ell\ell)$ distributions from the data control sample are reweighted to the shape obtained from DY simulation after the track veto cut (Fig. 4.26). The full difference in the background predictions between the reweighted and non-reweighted estimates is included as a systematic uncertainty. The resulting contributions are summarized in Sec. 4.4.3.

4.4.2 Double dissociation $\gamma\gamma \to \ell^+\ell^-$ background

The background from $\gamma\gamma \to \ell^+\ell^-$ production with double dissociation is estimated by mixing simulated events in the central detectors with data from the CT–PPS detectors. First the number of double dissociation Monte Carlo events passing the central detector selection is determined, and the corresponding shape of the $\xi(\ell\ell)$ distribution

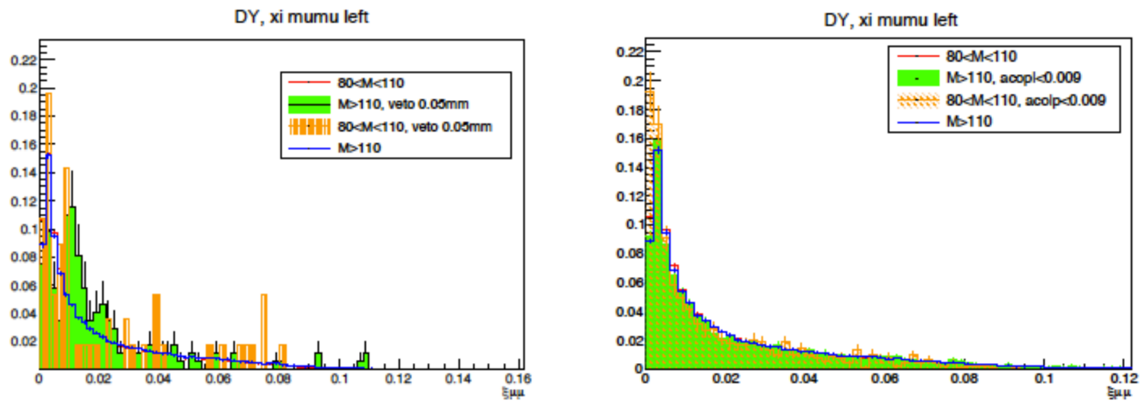

Figure 4.23: $\xi(\mu\mu)$ distributions in DY MC before (continuous histogram) and after (shaded histogram) the central detector cuts. Left: effect of the veto on extra tracks within 0.5 mm of the dimuon vertex. Right: effect of the acoplanarity and dimuon invariant mass cuts.

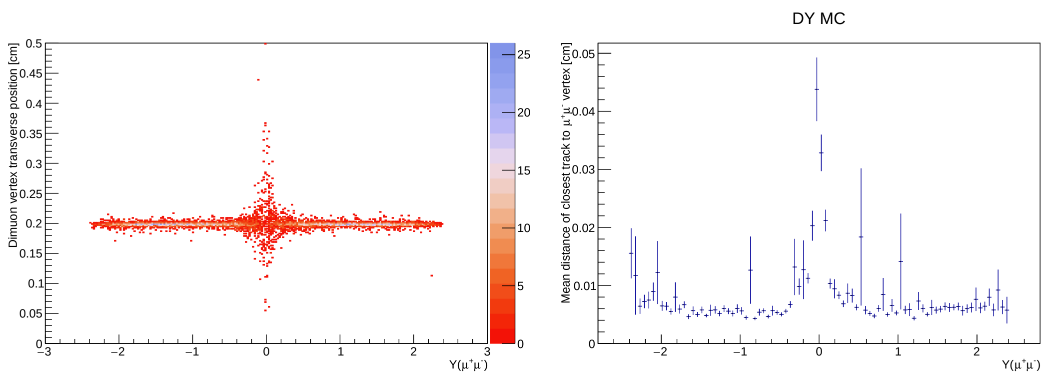

Figure 4.24: Left: Dimuon transverse vertex position vs. dimuon pair rapidity distribution in DY Monte Carlo events. Right: Dimuon pair rapidity vs. mean distance to the closest additional track to the dimuon vertex distribution, in DY Monte Carlo events.

is obtained by fitting an exponential shape to the simulated events (Figs. 4.27 and 4.28). Then a toy simulation is performed by sampling the fitted $\xi(\ell\ell)$ shape, and associating the resulting ξ value to a proton track from the Z control sample. To take into account the fraction of events without overlapping protons, the same data sample is also used to derive the number of events passing the central selection but not containing any Roman Pot data. For the final background estimate, the number of events in the toy simulation is normalized to the number of Monte Carlo events

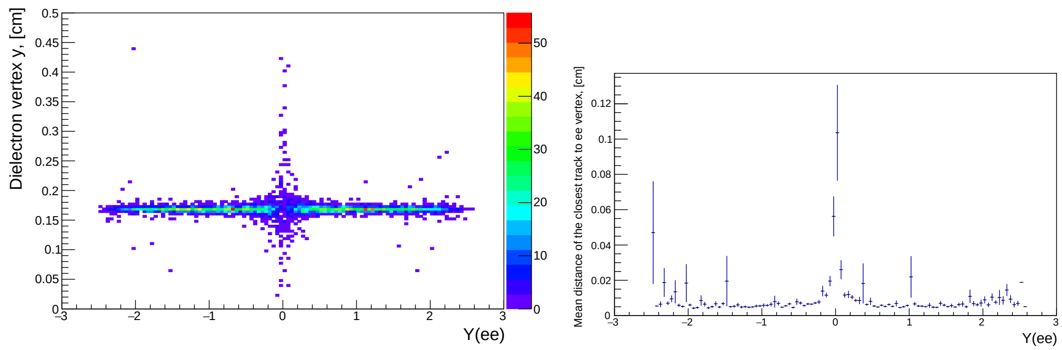

Figure 4.25: Left: Dielectron y vertex position vs. dielectron pair rapidity distribution in DY Monte Carlo. Right: Dielectron pair rapidity vs. mean distance to the closest additional track to the dielectron vertex distribution, in DY Monte Carlo events.

passing the full central selection and corrected for the fraction of events without any protons from the data.

4.4.2.1 Survival probability corrections in double dissociation

The number of double dissociation events passing the central detector cuts is taken from the simulation, and therefore depends on the theoretical prediction for the cross section and efficiency to pass the cuts. As discussed earlier, the LPAIR $\gamma\gamma \to \ell^+\ell^-$ samples are generated with no survival probability effects. For the elastic and single dissociation topologies this is expected to result in a mild suppression of the visible cross section, but for double dissociation the suppression factor can be very large [73, 80] with $S^2 = 0.13$.

In order to check this prediction, a control sample is selected with events passing all signal selection criteria, except that a large dimuon acoplanarity ($|1-\Delta\phi(\mu\mu)/\pi| > 0.015$) is required; in this region, LPAIR predicts a large double dissociation contribution. Figure 4.29 (top) shows that with the default $S^2 = 1.0$ there is a deficit compared to the data, while with a correction of $S^2 = 0.13$ applied to the double dissociation component, the data/MC agreement is reasonable. The single dissociation and elastic components may be suppressed as well — this test simply indicates that

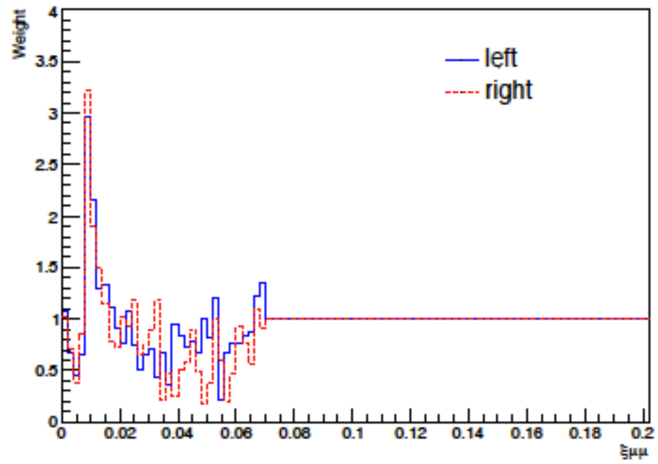

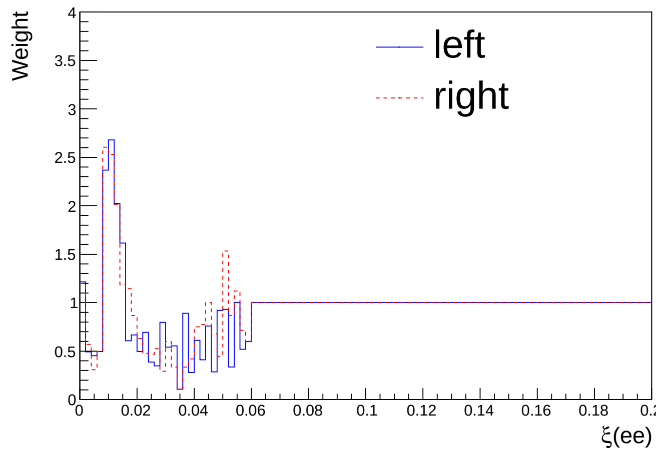

Figure 4.26: Weights applied to the Drell-Yan $\xi(\mu^+\mu^-)$ (top) and $\xi(e^+e^-)$ (bottom) distributions to account for the effect of the track veto cut.

the sum of all $\gamma\gamma \to \mu^+\mu^-$ processes in LPAIR is overestimated, but does not directly provide a measurement of the survival probability in double dissociation.

For the final double dissociation background estimate the survival probability correction $S^2 = 0.13$ is applied to the LPAIR prediction for both the dimuon and the dielectron channels, and includes a 100% relative uncertainty on the normalizations of these processes.

An additional check is performed to estimate the effect of introducing a Y-dependent survival probability. For this, values from the last column of Table 4.1 are considered, which correspond to sum of the single and double dissociation components. The survival probability for the double dissociation component is derived

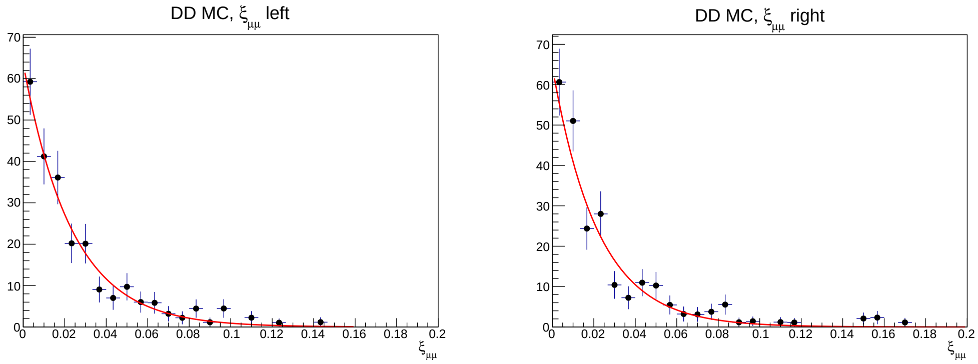

Figure 4.27: $\xi(\mu\mu)$ distributions in the DD Monte Carlo sample for the left and the right side of the spectrometer, fitted with an exponential function.

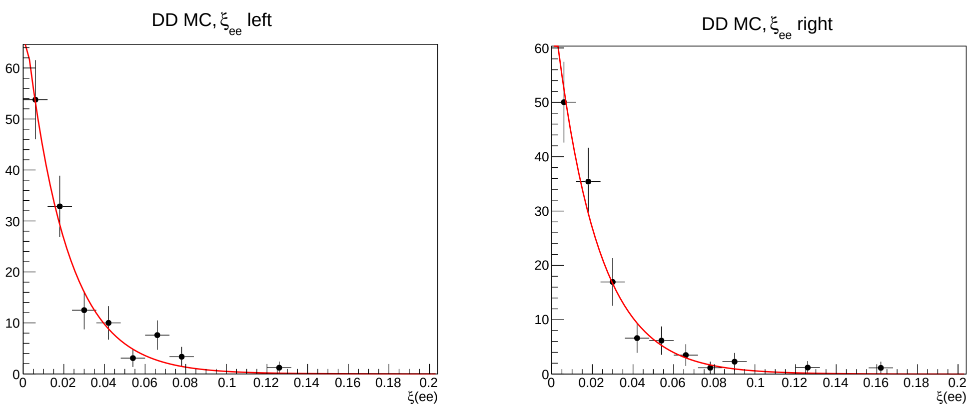

Figure 4.28: $\xi(ee)$ distributions in the DD Monte Carlo sample for the left and the right side of the spectrometer, fitted with an exponential function.

from these assuming the same ratio of double/single dissociation as theoretically predicted at mid-rapidity (|Y| < 0.5). This results in $S^2_{DD}(0 < |\mathrm{Y}| < 0.6) = 0.13$, $S^2_{DD}(|\mathrm{Y}| > 0.6) = 0.021$. These Y-dependent suppression factors are then applied as weights for the Monte Carlo events used to derive the shape of $\xi(\mu\mu)$ spectrum in double dissociaton events. The newly obtained spectra are then fitted and the background estimation procedure described above is repeated using the updated fits. The resulting predictions are summarized in Table 4.2. They are about five times lower than in case of the constant survival probability, which is larger than the ratio between the constant and modified survival probabilities integrated over Y. The

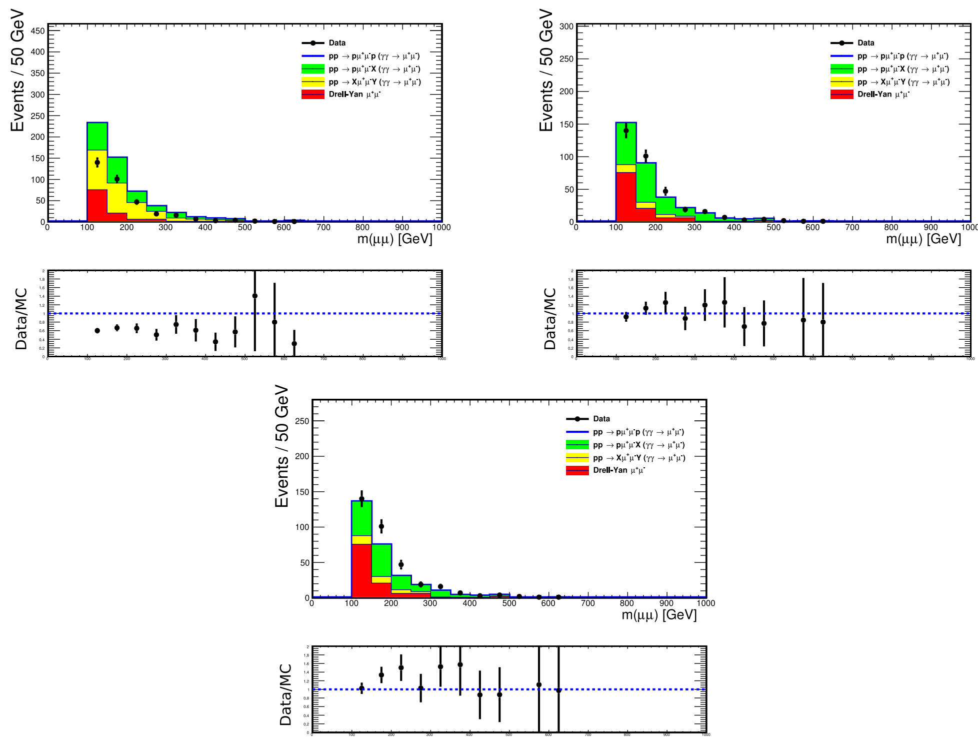

Figure 4.29: $m(\mu\mu)$ distributions in the control region with zero additional tracks at the dimuon vertex, and $|1-\Delta\phi(\mu\mu)/\pi| > 0.015$. The left plot shows the comparison of data to simulation when no survival probability suppression is included in the theory ($S^2 = 1.0$). The center plot shows the same comparison with a survival probability of $S^2 = 0.13$ applied to the double dissociation component, while the right plot has survival probabilities applied to all three components.

reason for the stronger suppression is the modification of the $\xi(\mu\mu)$ shapes because of the introduced weights – they become steeper. This means that the fraction of double dissociative events within the pots acceptance is reduced not only because of the larger suppression factor applied directly, but also because of the event migration towards lower $\xi(\mu\mu)$.

4.4.2.2 Backgrounds from protons in double dissociation

Because baryon number is conserved, the final state of the dissociating system should contain one proton or one neutron. In case the proton falls within the acceptance of CT–PPS, this can be an additional contribution to the background.

The background due to these secondary protons is estimated using generator-level simulation. The corresponding distribution of $\xi(\mu\mu)$ vs. $\xi(p)$ is shown on Fig. 4.30, where $\xi(p)$ is the fractional momentum loss of the most forward proton on each side. About 2-5% (depending on the station) of all double-dissociative events pass the central selection and have secondary proton within the CT–PPS acceptance. Assuming the cross section value predicted by LPAIR and a 13% survival probability, 0.17-0.38 events per station are expected after the signal selection. This leads to the final estimate of less then one secondary proton event in the signal sample. A similar number is expected for the dielectron channel.

In most of these events the proton results from the fragmentation of an N^* or Δ-baryon resonance, or from the remnant of an inelastic photon-quark interaction. In this case additional particles from the fragmentation are present in the event, implying that the proton has much lower energy (much higher ξ) than predicted by the dilepton kinematics. This explains the small number of background events from this source.

4.4.3 Total background

The final background predictions for the dimuon events are shown in Tables 4.3-4.4, for each station separately. For a 2σ matching window, the background prediction for the dimuon channel ranges between 0.52 and 0.66 events per station.

For the e^+e^- channel the predictions are shown in Tables 4.5 and 4.6. For a 2σ matching window, the total background is between 0.83 and 1.03 events per station. In order to be compared to the number of events observed in data, the number of background events expected with tracks in either or both of the near and far stations on each arm is calculated, cf. Tables 4.7 and 4.8 for the dimuon channel and Tables 4.9 and 4.10 for the dielectron channel.

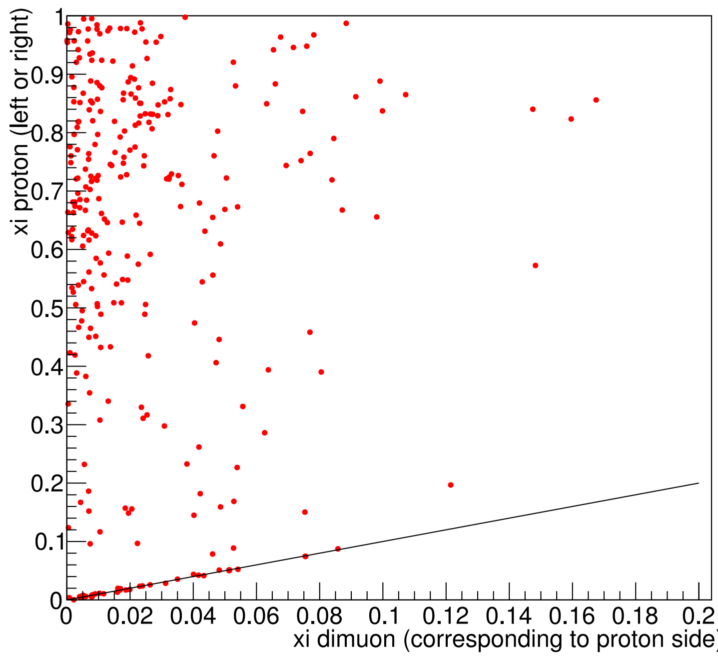

Figure 4.30: Generator-level $\xi(\mu\mu)$ vs. $\xi(p)$ distribution, in double dissociation events with a proton in the final state of the dissociating system. The diagonal line corresponds to the case where the kinematics of the proton and that of the dimuon system match.

Arm	1σ	2σ	3σ	full
Left	0.006 $\pm$ 0.001	0.009 $\pm$ 0.001	0.013 $\pm$ 0.001	0.149 $\pm$ 0.004
Right	0.005 $\pm$ 0.001	0.009 $\pm$ 0.001	0.013 $\pm$ 0.001	0.121 $\pm$ 0.004

Table 4.2: Estimated backgrounds from double-dissociation $\gamma\gamma \to \mu^+\mu^-$ production, with proton kinematics matching within 1σ, 2σ, 3σ respectively, and within the full Roman Pots acceptance in at least one of the FAR and NEAR stations of given arm. The Y-dependence of survival probability is taken into account using $S^2(0 < |\mathrm{Y}| < 0.6) = 0.13$, $S^2(|\mathrm{Y}| > 0.6) = 0.021$.

For a 2σ matching window, this results in a total background prediction of 1.49 ± 0.07 (stat.) dimuon events and 2.36 ± 0.09 (stat.) dielectron events with a matching RP track in at least one station, in both arms combined.

Station	1σ	2σ	3σ	full
Left far	0.286 ± 0.030	0.627 ± 0.045	0.917 ± 0.054	5.517 ± 0.126
Left near	0.230 ± 0.027	0.554 ± 0.042	0.776 ± 0.050	3.962 ± 0.109
Right far	0.233 ± 0.027	0.513 ± 0.039	0.726 ± 0.046	4.664 ± 0.115
Right near	0.258 ± 0.028	0.486 ± 0.037	0.707 ± 0.046	3.729 ± 0.102

Table 4.3: Estimated backgrounds from Drell-Yan $\mu^+\mu^-$ production, with proton kinematics matching within 1σ, 2σ, 3σ respectively, and within the full Roman Pots acceptance.

Station	1σ	2σ	3σ	full
Left far	0.022 ± 0.002	0.036 ± 0.003	0.058 ± 0.004	0.517 ± 0.011
Left near	0.013 ± 0.002	0.031 ± 0.003	0.045 ± 0.003	0.306 ± 0.008
Right far	0.021 ± 0.002	0.048 ± 0.003	0.073 ± 0.004	0.544 ± 0.011
Right near	0.014 ± 0.002	0.038 ± 0.003	0.065 ± 0.004	0.385 ± 0.009

Table 4.4: Estimated backgrounds from double-dissociation $\gamma\gamma \to \mu^+\mu^-$ production, with proton kinematics matching within 1σ, 2σ, 3σ respectively, and within the full Roman Pots acceptance.

Station	1σ	2σ	3σ	full
Left far	0.443 ± 0.037	0.912 ± 0.053	1.350 ± 0.064	5.520 ± 0.120
Left near	0.410 ± 0.036	0.806 ± 0.051	1.160 ± 0.060	4.000 ± 0.110
Right far	0.481 ± 0.040	0.952 ± 0.056	1.460 ± 0.070	5.450 ± 0.130
Right near	0.478 ± 0.040	1.010 ± 0.059	1.400 ± 0.069	4.750 ± 0.130

Table 4.5: Estimated backgrounds from Drell-Yan e^+e^- production, with proton kinematics matching within 1σ, 2σ, 3σ respectively, and within the full Roman Pots acceptance.

Station	1σ	2σ	3σ	full
Left far	0.014 ± 0.001	0.029 ± 0.002	0.044 ± 0.002	0.284 ± 0.006
Left near	0.010 ± 0.001	0.021 ± 0.002	0.034 ± 0.002	0.170 ± 0.004
Right far	0.012 ± 0.001	0.027 ± 0.002	0.040 ± 0.002	0.227 ± 0.005
Right near	0.009 ± 0.001	0.021 ± 0.002	0.031 ± 0.002	0.140 ± 0.004

Table 4.6: Estimated backgrounds from double-dissociation $\gamma\gamma \to e^+e^-$ production, with proton kinematics matching within 1σ, 2σ, 3σ respectively, and within the full Roman Pots acceptance.

Arm	1σ	2σ	3σ	full
Left	0.373 ± 0.034	0.752 ± 0.048	1.054 ± 0.057	6.135 ± 0.132
Right	0.338 ± 0.032	0.626 ± 0.043	0.890 ± 0.052	5.221 ± 0.122

Table 4.7: Estimated backgrounds from Drell-Yan $\mu^+\mu^-$ production, with proton kinematics matching within 1σ, 2σ, 3σ respectively, and within the full Roman Pots acceptance in at least one of the FAR and NEAR stations of given arm.

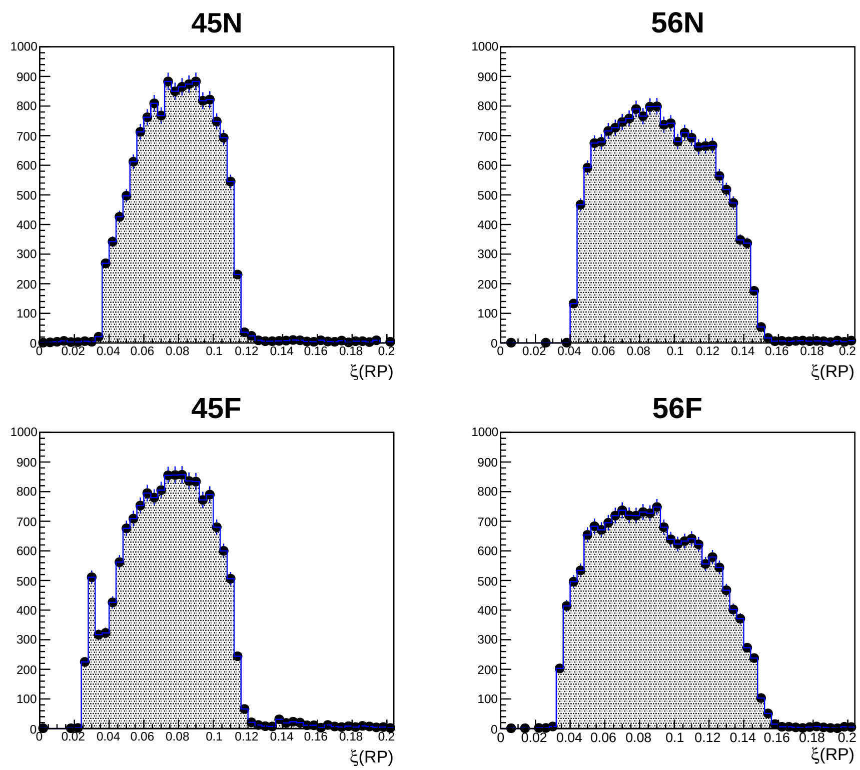

Figure 4.31: Distributions of ξ (RP). The Roman Pot data are sampled over the same running period as used for the analysis.

Arm	1σ	2σ	3σ	full
Left	0.028 ± 0.003	0.046 ± 0.003	0.072 ± 0.004	0.572 ± 0.012
Right	0.029 ± 0.003	0.062 ± 0.004	0.091 ± 0.005	0.595 ± 0.012

Table 4.8: Estimated backgrounds from double-dissociation $\gamma\gamma \rightarrow \mu^+\mu^-$ production, with proton kinematics matching within 1σ, 2σ, 3σ respectively, and within the full Roman Pots acceptance in at least one of the FAR and NEAR stations of given arm.

4.5 Background estimate cross-check

In order to cross-check the background estimate, an additional study based on the events passing the signal selection is carried out. A toy experiment is performed, in which the $\xi(\mu\mu)$ values of the events within the acceptance are matched to randomly sampled ξ(RP) values from the same running period as the data used for this analysis (Fig. 4.31). For each toy event, the ξ(RP) value is sampled from the FAR station on the side for which the $\xi(\mu\mu)$ was derived in the analysis. The toy experiment is

Arm	1σ	2σ	3σ	full
Left	0.563 ± 0.042	1.070 ± 0.057	1.570 ± 0.069	6.240 ± 0.130
Right	0.675 ± 0.047	1.230 ± 0.064	1.730 ± 0.076	6.090 ± 0.140

Table 4.9: Estimated backgrounds from Drell-Yan e^+e^- production, with proton kinematics matching within 1σ, 2σ, 3σ respectively, and within the full Roman Pots acceptance in at least one of the FAR and NEAR stations of given arm.

Arm	1σ	2σ	3σ	full
Left	0.017 ± 0.001	0.035 ± 0.002	0.052 ± 0.002	0.313 ± 0.006
Right	0.016 ± 0.001	0.032 ± 0.002	0.048 ± 0.002	0.247 ± 0.005

Table 4.10: Estimated backgrounds from double-dissociation $\gamma\gamma \to e^+e^-$ production, with proton kinematics matching within 1σ, 2σ, 3σ respectively, and within the full Roman Pots acceptance in at least one of the FAR and NEAR stations of given arm.

repeated 10000 times, and the mean number of events having $\xi(\mu\mu)$ matching $\xi(\text{RP})$ within 2σ is derived.

The signal to background ratio in the data is not known a priori. This means that using all observed data events for toy matching may overestimate the background: signal events should not be counted as a background if they are matched after replacing the measured $\xi(\text{RP})$ with a random one. As it is not possible to exclude unknown signal events, several hypotheses of S/B ratio in the observed sample are tested by varying the number of $\xi(\mu\mu)$ values used for the toy matching.

One additional feature of the toy background model is that because of the non-flat $\xi(\text{RP})$ spectrum (see Fig. 4.31), the matching probability varies as a function of $\xi(\mu\mu)$. In practice this means that not only the number of events used for toy matching, but also the choice of a specific $\xi(\mu\mu)$ value will produce different results. Thus several choices of $\xi(\mu\mu)$ values are considered, with points taken at opposite sides of the $\xi(\mu\mu)$ spectrum.

The numbers obtained using different input $\xi(\mu\mu)$ sets are summarized in Table 4.11.

Several cases are studied:

1. **All observed $\boldsymbol{\xi(\mu\mu)}$ values are selected for matching (i.e. assume that all observed events are background)**. This produces 1.8 accidentally matching events in the toy MC. There are 12 matching events observed in the data; the probability to observe 12 events if the mean is 1.8 according to the Poisson distribution is less then 1×10^{-6}, which indicates that the all-background hypothesis is unrealistic.

2. **Only $\boldsymbol{\xi(\mu\mu)}$ values outside the matching region are used: i.e. zero background hypothesis.** In this case 0.55 accidentally matching events are observed, corresponding to 50% probability to have zero background according to Poisson distribution.

3. **Only $\boldsymbol{\xi(\mu\mu)}$ values inside the matching region.** This selection illustrates by how much one would overestimate background on average when including all signal events. 1.25 accidentally matching events are observed.

4. **All $\boldsymbol{\xi(\mu\mu)}$ values outside the matching region, plus 1-2 inside.** One or two events from 2σ matching region are added, as a cross check for the nominal method prediction of 1.22 background events (in FAR RP stations), which is between 1 and 2. This input results in a prediction of 0.57-0.76 accidentally matched toy events for 1 additional signal-region event, and 0.69-0.98 matched events for 2 additional signal-region events. These numbers are in reasonable agreement with the nominal prediction of 1.22 events, taking into account the systematic uncertainty of the nominal background estimation $\sim 37\%$ and the limited statistics of the signal sample used for toy mixing.

The comparison described above lends support to the nominal background estimate.

Method used to derive the prediction:	Number of matched within 2σ events		
	45FAR	56FAR	SUM (45F+56F)
Nominal background estimate	0.66	0.561	1.22
Matching all $\xi(\mu\mu)$	0.868	0.933	1.801
Matching only signal region $\xi(\mu\mu)$	0.568	0.683	1.251
Matching only background region $\xi(\mu\mu)$	0.300	0.250	0.550
Matching all background + 1 event from signal region at smallest $\xi(\mu\mu)$	0.315	0.377	0.692
Matching all background + 1 event from signal region at largest $\xi(\mu\mu)$	0.450	0.464	0.914
Matching all background + 2 events from signal region at smallest $\xi(\mu\mu)$	0.336	0.504	0.840
Matching all background + 2 events from signal region at largest $\xi(\mu\mu)$	0.592	0.678	1.270

Table 4.11: Results obtained using the nominal background estimation methods described in Sec. 4 (see Table 4.4 and Table 4.3) (the first line) and using various configurations for the toy mixing experiment (the remaining lines).

4.5.1 Same-sign cross-check

As an additional cross-check, also same-sign $\mu^{\pm}\mu^{\pm}$ events are examined. Real $\gamma\gamma \rightarrow \mu^{\pm}\mu^{\pm}$ production is forbidden by charge conservation, but small backgrounds from electroweak or heavy flavor production processes could produce same-sign and opposite-sign pairs if some tracks are lost, in coincidence with a RP track from pileup or beam backgrounds. Ten same-sign events passing the central detector selection cuts are observed, none of which have a predicted $\xi(\mu^{\pm}\mu^{\pm})$ within the RP acceptance for any station. This rules out a background contribution from these sources.

4.6 Systematics

The uncertainties related to the effects of alignment and optics on the reconstruction of ξ(RP), and to the muon and electron momentum scales and resolution in the determination of $\xi(\ell\ell)$ are included for each event as described in Secs. 3.2, 3.3.1, 4.3.5 (and references quoted there).

In addition, when evaluating the significance of the excess above the background, the following sources of uncertainty in the background estimation are considered:

- The statistical uncertainty in the Drell-Yan and double dissociation estimates, due to the finite statistics of the simulated samples and the Z-peak sample used to derive the random proton correlations. For the dimuon channel, this corresponds to 5% for the Drell-Yan background, and 5% for the double dissociation background. For the dielectron channel, it amounts to 4% for the Drell-Yan background, and 4% for the double dissociation background.

- A luminosity uncertainty of 2.5% [83] for both the dimuon and dielectron channels is applied to the double dissociation estimate, in which the yield of events passing the central detector cuts depends on the data luminosity and the cross section predicted by the MC.

- A conservative uncertainty of 100% for both the dimuon and dielectron channels is applied to the double dissociation rate estimate, to account for the theoretical uncertainty on the survival probability. The existing theoretical predictions for the survival probability are obtained for mid-rapidity and for lower-p_T muons (20 GeV) than those used in the current measurement. This conservative uncertainty is chosen because of the extrapolation to higher p_T and rapidity values.

- The uncertainty on the Drell–Yan background estimate is evaluated from the difference between the track multiplicity distributions in the data and the simulation. This difference enters the background estimate through the scale factor used to extrapolate from the inclusive Z-peak control sample to the signal region. In the low multiplicity, DY-dominated region with 1-5 tracks, the MC overestimates the data (Figs. 4.5 and 4.6). The average data-MC difference in this region is taken as an estimate of the uncertainty of the number of expected DY events in the region with small extra track multiplicity, resulting in a 28% uncertainty for the dimuon channel and 14% for the dielectron channel. The difference between the two channels reflects the difference in the muon and electron reconstruction efficiencies over the whole rapidity range (Figs. 4.9 and 4.10). As the precision of the dilepton vertex reconstruction depends on the leptons rapidity, this propagates also to the extra track multiplicity at the vertex (see Figs. 4.24 and 4.25).

- A further uncertainty of 25% (for the dimuon channel) and 11% (for the dielectron channel) is applied to the Drell-Yan background estimate, corresponding to the difference between the background estimates with and without reweighting to the shape of the $\xi(\ell^+\ell^-)$ distribution in the DY MC.

  As an additional cross check of this uncertainty, all the nominal central detector signal region cuts are applied, while relaxing the invariant mass requirement from 110 GeV to 80 GeV, to select the $Z \to \ell^+\ell^-$ region. As described in Sec. 4.3, the single lepton p_T requirement of 50 GeV strongly suppresses the Z region, and no events compatible with $Z \to \ell^+\ell^-$ are observed. Therefore the cut is relaxed to $p_T > 40$ GeV. In this case a large number of events in the $Z \to \ell^+\ell^-$ region are observed, with a yield that is consistent with the simulation, within the 28% and 14% uncertainties assigned to the dimuon and dielectron results, respectively (Figs. 4.32, 4.33), confirming the nominal estimate above.

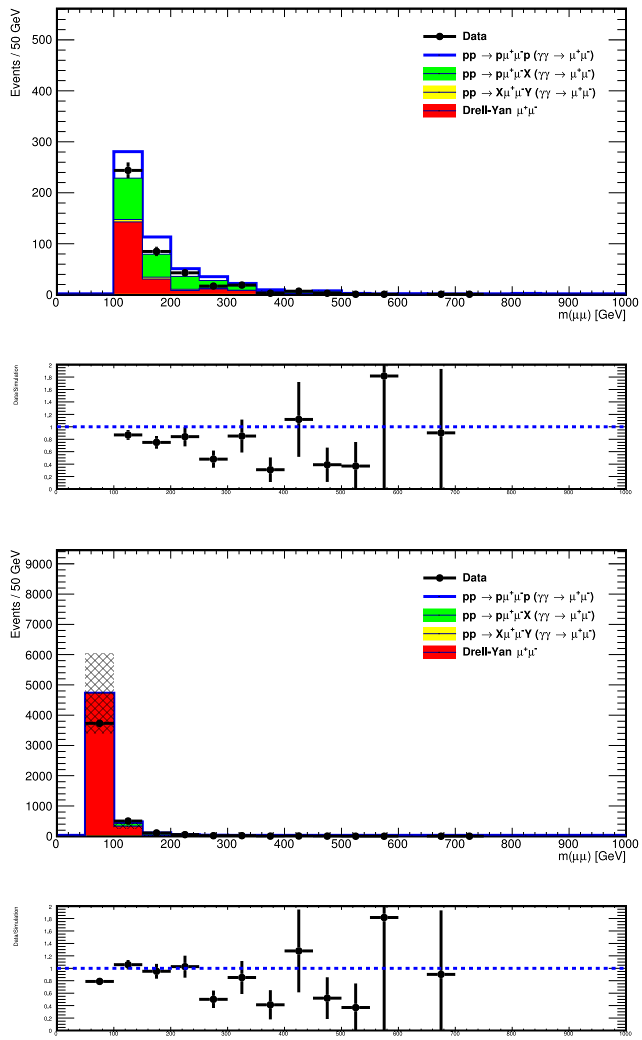

Figure 4.32: Dimuon invariant mass for all events passing the central detector selction, with the minimum mass cut lowered from 110 GeV to 80 GeV. The data and simulation are shown with single muon p_T cuts of 50 GeV (top, nominal), and 40 GeV (bottom). In the bottom plot, the shaded band indicates the systematic uncertainty assigned to the modelling of low-multiplicity Drell-Yan production.

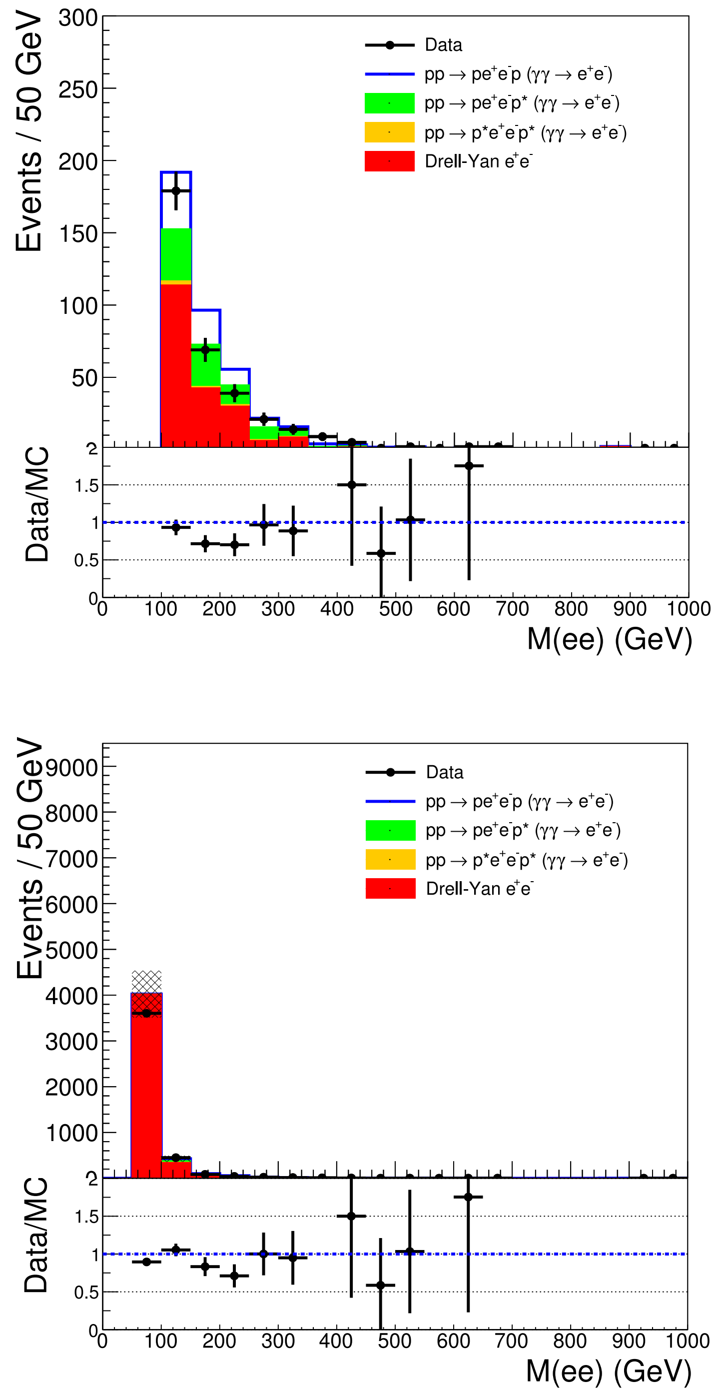

Figure 4.33: Dielectron invariant mass for all events passing the central detector selction, with the minimum mass cut lowered from 110 GeV to 80 GeV. The data and simulation are shown with single electron p_T cuts of 50 GeV (top, nominal), and 40 GeV (bottom). In the bottom plot, the shaded band indicates the systematic uncertainty assigned to the modelling of low-multiplicity Drell-Yan production.

4.7 Results (dimuon channel)

The correlation between $\xi(\mu\mu)$ and the ξ value measured in CT–PPS is shown in Fig. 4.34, for each of the four stations separately. In each plot the shaded band indicates the kinematic region that is out of the CT–PPS acceptance, where the sample is dominated by uncorrelated pileup and beam-background events. The error bars represent the 3.3% $\xi(\mu^+\mu^-)$ resolution and the 5.5% uncertainty on the ξ value of the measured proton track discussed earlier. In Fig. 4.35, the correlation is plotted for each arm, with the near and far RPs combined.

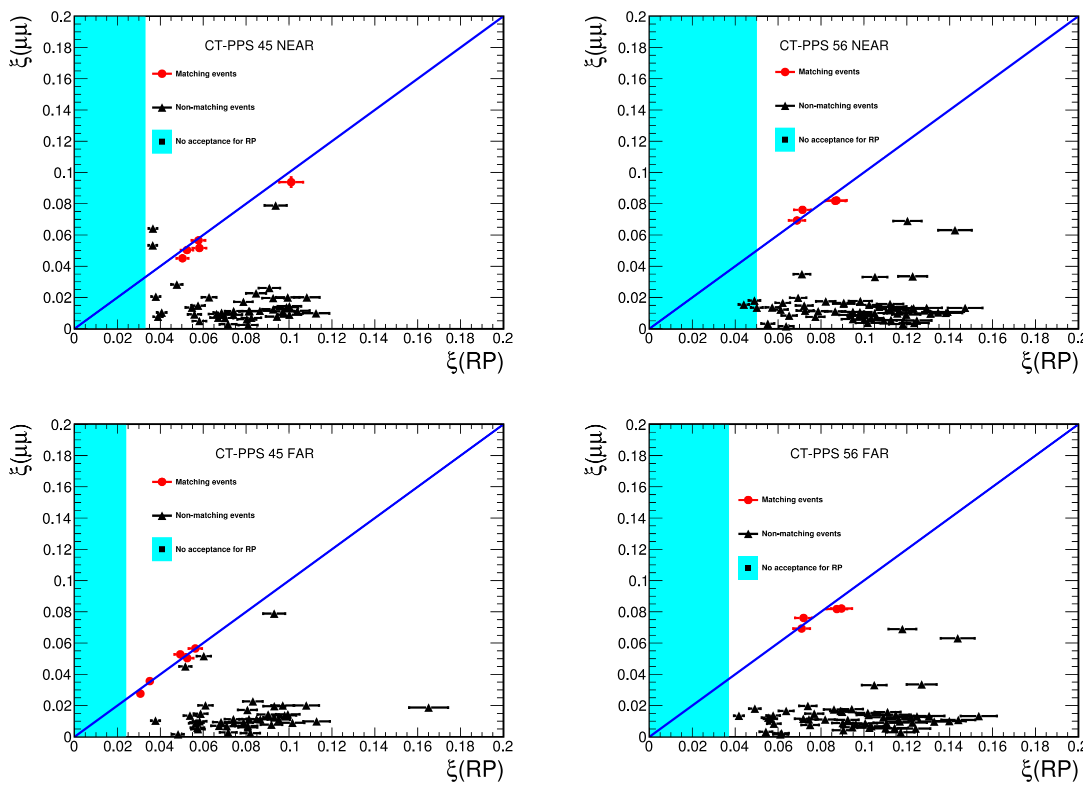

Figure 4.34: Correlation between $\xi(\mu\mu)$ and the ξ value measured in the Roman Pots, for each tracking Roman Pot. The shaded region corresponds to events in which the signal proton is predicted to be outside the Roman Pot acceptance. The plots correspond to the 45 near (upper left), 56 near (upper right), 45 far (lower left), and 56 far (lower right) stations. The events falling within the 2σ matching window are denoted by red circles, while those outside the 2σ window are indicated by black triangles.

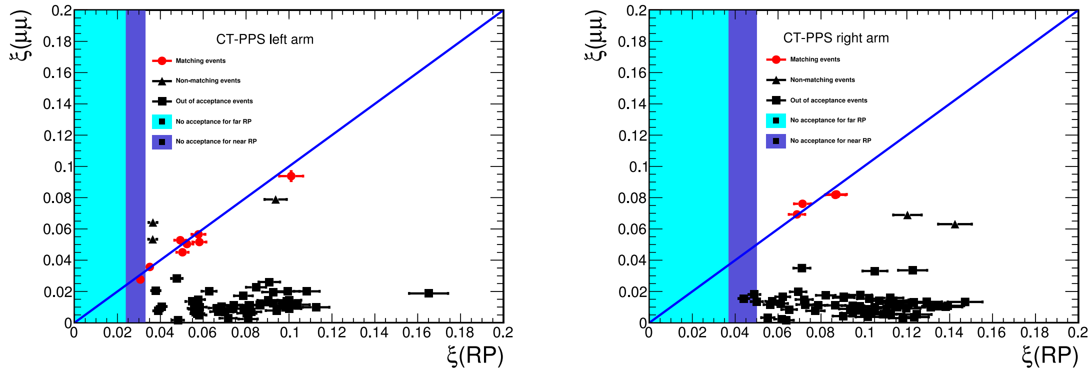

Figure 4.35: Correlation between $\xi(\mu\mu)$ and ξ measured in the Roman Pots, for both Roman Pots in each arm combined. The 45 (left) and 56 (right) arms are shown. The light shaded region corresponds to the kinematical region outside the acceptance of the far RP, while the darker shaded region corresponds to the region outside the acceptance of the near RP. For the events in which a track is detected in both, the ξ value measured at the near RP is plotted.

A total of 17 events pass all central detector cuts, have a $\xi(\mu\mu)$ value corresponding to a proton within the CT–PPS acceptance on one arm, and have a RP track reconstructed in at least one station in that arm. Figure 4.36 shows the relative difference of $\xi(\mu\mu)$ with respect to ξ(RP) for these events, with the $\pm 2\sigma$ window in which a signal peak is expected denoted by the vertical lines.

A total of 12 events is observed in which the measured ξ(RP) in at least one station matches the $\xi(\mu\mu)$ predicted from the muon kinematics within 2σ. Of these, 8 have tracks reconstructed in both the near and far stations of one arm, while 4 have tracks detected in 1 of the 2 stations. Of the events with RP tracks in both stations, two have a proton that is measured just within the 2σ cutoff in one station (1.7σ, 1.8σ), and just outside the cutoff in the adjacent station (2.1σ, 2.3σ).

From the background estimates in Sec. 4.4, a total of 11 ± 4.0 (statistical and systematic uncertainties added in quadrature) background events are expected within the acceptance, but falling outside the 2σ matching window in $\xi(\mu\mu)$ and ξ(RP). In the data five such non-matching events are found, compatible with the background prediction at the 1.4σ level.

An estimate of the significance for finding twelve matching events given the background prediction of Sec. 4.4 is carried out using the HybridNew method of the Higgs Combine tool [84] and considering the systematic uncertainties in the background estimate described in Sec. 4.6 as log-normal nuisance parameters. This results in 4.3 σ.

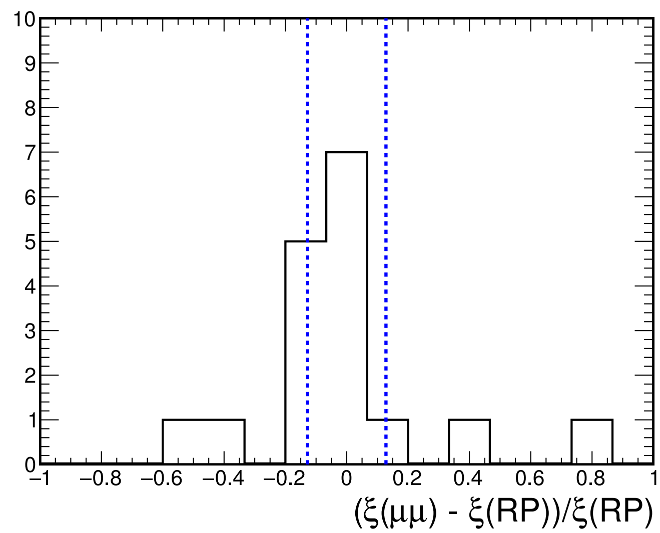

Figure 4.36: Plot of the residuals $(\xi(\mu\mu) - \xi(\mathrm{RP}))/\xi(\mathrm{RP})$, for all events with a proton predicted within the CT–PPS acceptance and at least one RP track reconstructed. The blue vertical lines indicate the $\pm 2\sigma$ matching window used to define the signal region. In events with a RP track measured in both NEAR and FAR stations, only the NEAR measurement of ξ is plotted.

4.7.1 Properties of the signal region events

The properties of the 12 selected events are shown in Table 4.12. In the events with tracks reconstructed in both near and far stations, the two $\xi(\mathrm{RP})$ measurements are compatible within 5%. The vertical position of the RP tracks is within 1.5 mm of zero in all events, consistent with the hypothesis of $\gamma\gamma$ production with small absolute value of four-momentum transfer squared t. Figure 4.37 shows the dimuon invariant mass and rapidity distributions of the selected events, demonstrating the coverage expected for single tagged events from the pre-TS2 optics and acceptance (Fig. 4.38). Five of the selected events have an acoplanarity value smaller than 0.0005, where the elastic contribution is expected to be prominent. The remaining have acoplanarity values greater than 0.0015, where single dissociation is expected to be dominant (Fig. 4.39).

Figure 4.40 shows the result of a fit for the fraction of elastic and single dissociation events among the 12 signal region candidates, based on the acoplanarity distribution. The signal template shapes are taken from the LPAIR simulation, after all cuts are applied. The background is normalized to the value expected in the data. Because of the smallness of the double dissociation contribution and the similarity between the Drell-Yan and double dissociation shapes, the background template is taken from the Drell-Yan MC. The best fit results in roughly equal yields of elastic and single dissociation events, with large unceratinties:

$$N(pp \to p\mu^+\mu^-p) = 5.2 \pm 2.9,$$

$$N(pp \to p\mu^+\mu^-p^*) = 5.3 \pm 3.2.$$

4.7.1.1 Summary of events with tracks in only one station

Of the twelve candidate events, four have RP tracks in only one of the two stations. This may happen because of the different acceptance between the near and far stations, or because of inefficiencies in reconstructing tracks (for example because of radiation damage to the strips in the region sensitive to low ξ values, or failure of the track reconstruction when multiple tracks are present).

Of the four such single-station events, one has a track in the 45-FAR station ($\xi = 0.031$) that is out of the acceptance of 45-NEAR ($\xi_{min} = 0.033$). Three events

Run:LS:Event	$\xi(\mu\mu)$	Sector	ξ(RP)	x(RP) [mm]	y(RP) [mm]	$m(\mu\mu)$ [GeV]	$Y(\mu\mu)$
274971:546:814088551	0.069	56-NEAR	0.069	5.15	-0.793	137	-1.89
274971:546:814088551	0.069	56-FAR	0.071	5.05	-0.999	137	-1.89
275125:413:778836261	0.082	56-NEAR	0.087	6.7	-0.577	329	-1.18
275125:413:778836261	0.082	56-FAR	0.090	6.55	-0.705	329	-1.18
275918:254:432304802	0.076	56-NEAR	0.071	5.36	0.719	279	-1.27
275918:254:432304802	0.076	56-FAR	0.072	5.13	0.862	279	-1.27
279841:995:1697032699	0.082	56-NEAR	0.087	6.65	-0.281	110	-2.26
279841:995:1697032699	0.082	56-FAR	0.087	6.37	-0.336	110	-2.26
279766:1575:2754611755	0.050	45 NEAR	0.052	5.29	-0.134	124	1.66
279766:1575:2754611755	0.050	45-FAR	0.053	5.26	-0.0926	124	1.66
279841:335:518378884	0.052	45 NEAR	0.058	5.93	-0.38	114	1.78
279841:335:518378884	0.052	45-FAR	0.060	6.11	-0.541	114	1.78
279844:212:258097039	0.045	45 NEAR	0.050	5.06	-0.361	307	0.645
279844:212:258097039	0.045	45-FAR	0.052	5.16	-0.482	307	0.65
280017:447:783978922	0.057	45 NEAR	0.058	5.89	-0.956	148	1.56
280017:447:783978922	0.057	45-FAR	0.056	5.67	-1.26	148	1.56
273730:1581:1646037324	0.036	45-FAR	0.035	3.41	-0.619	342	0.3
274971:594:883153054	0.094	45 NEAR	0.101	11.1	-0.739	232	1.66
275920:294:524083123	0.053	45-FAR	0.049	4.91	-0.423	194	1.26
280191:536:1002667118	0.028	45-FAR	0.031	2.96	-0.286	164	0.787

Table 4.12: Properties of the signal candidate events. When a proton track is reconstructed in both the near and far stations, the event appears twice.

have a track that is within the acceptance of both stations of sector 45; in two of those events a track is only found in the FAR station ($\xi = 0.035, 0.049$), while in one event a track is only found in the NEAR station ($\xi = 0.101$). In sector 56, all four candidate events have tracks reconstructed in both the NEAR and FAR stations.

4.7.2 Double-tagged dimuon events

From the generator-level LPAIR Monte Carlo, the cross section for double-tagged events in the region $p_T(\mu) > 50$ GeV, $|\eta(\mu)| < 2.4$, $M_{\mu\mu} > 110$ GeV, $\xi(p1) > 0.024$, $\xi(p2) > 0.033$, is estimated to be 0.13 fb. Therefore in the sample of 9.4 fb^{-1} used in this analysis, a mean of ~ 1.2 events would be expected at most, if the efficiency of the central CMS selection cuts and the efficiency for reconstructing the proton tracks in the RPs were 100%. From the simulation, the efficiency for $pp \to p\mu^+\mu^-p$ events to pass all the central detector selection criteria is $\sim 69\%$. Assuming an upper limit

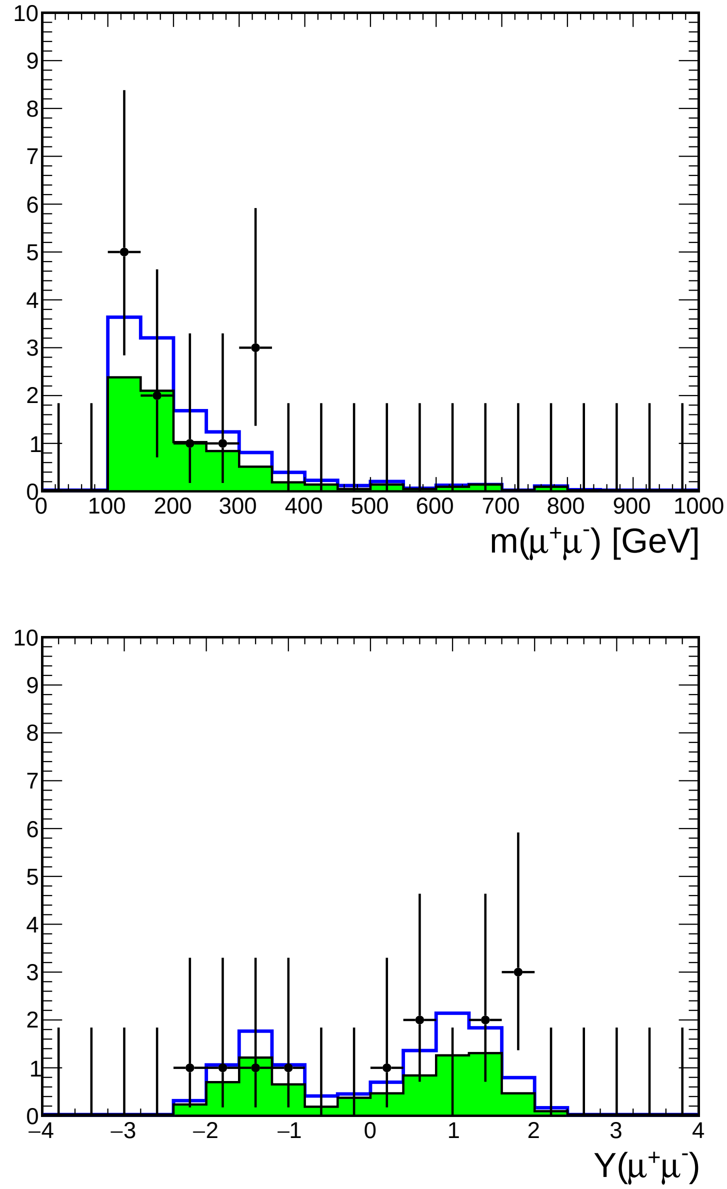

Figure 4.37: Invariant mass (top), and dimuon pair rapidity (bottom) distributions for the final sample of events with matching $\xi(\mu\mu)$ and $\xi(\mathrm{RP})$. The blue and green histograms represent the exclusive and semiexclusive contributions predicted by LPAIR, respectively. The error bars represent the Garwood intervals [85]. The signal simulation is shown normalized to the data, with the ξ acceptance cuts applied on the generator-level proton information. The simulation includes neither the effect of radiation damage nor other inefficiencies in the silicon strips, nor any survival probability suppression. Following the CMS convention, the positive-rapidity (resp. negative-rapidity) region corresponds to the 45 (resp. 56) LHC sector in the plots.

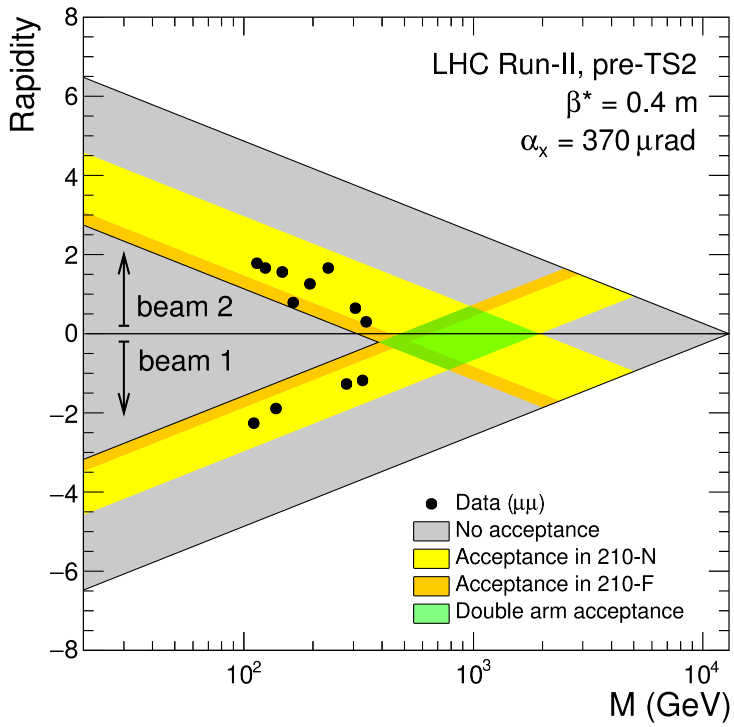

Figure 4.38: Expected pre-TS2 invariant mass-rapidity acceptance (accounting for the asymmetry observed between sectors 45 and 56). The data points overlaid to this figure correspond to the dimuon signal region events. The dark yellow and dark green bands correspond to the acceptance of the far stations, while the light yellow and light green bands correspond to the acceptance of the near stations. Following the CMS convention, the positive-rapidity (resp. negative-rapidity) region corresponds to the 45 (resp. 56) LHC sector.

on the luminosity-weighted efficiency for reconstructing the proton tracks in CT–PPS of 50%, < 0.4 double-tagged events are expected in the current dataset.

In the data no events are observed with protons detected in both arms of CT–PPS, with both ξ values consistent with the muon kinematics measured in the central CMS detectors. The minimum mass acceptance for detecting both protons from $pp \to p\mu^+\mu^-p$ events in at least one station per arm, given the single-arm acceptance values of Sec. 3.6, is $M(\mu^+\mu^-) \sim 360$ GeV. The signal candidate with the highest dimuon invariant mass has a value of $M(\mu^+\mu^-) = 342$ GeV, just below the minimum mass where both protons would be within the CT–PPS acceptance.

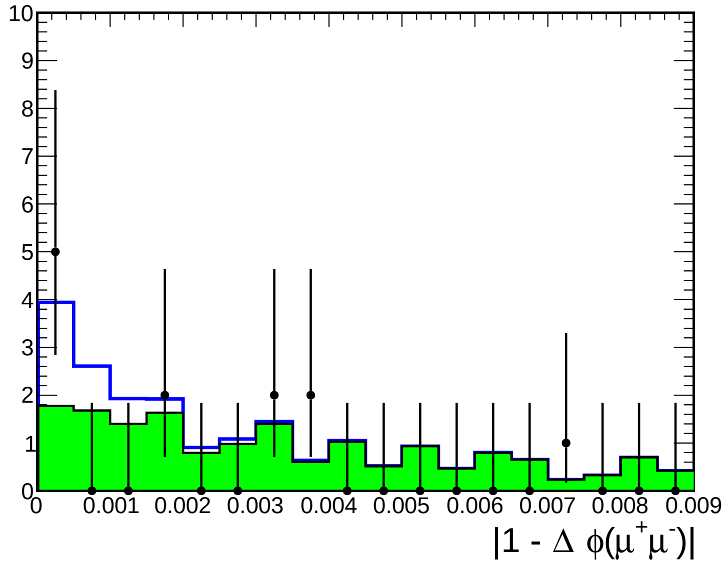

Figure 4.39: Acoplanarity distribution for the final sample of events with matching $\xi(\mu\mu)$ and $\xi(\mathrm{RP})$. The error bars show the Garwood intervals. The blue and green histograms represent the exclusive and semiexclusive contributions predicted by LPAIR, respectively. The signal simulation is shown normalized to the data, with the ξ acceptance cuts applied on the generator-level proton information. The simulation includes neither the effect of radiation damage nor other inefficiency in the silicon strips, nor any survival probability suppression.

4.7.3 Vertical component of scattering angle for signal events

An additional observable discriminating between signal and background is the squared four-momentum transfer t of the protons. For $\gamma\gamma$ induced production, the value of t is expected to be compatible with zero within resolution. For diffractive processes of the type dominating the sample of pileup protons, the average value of $|t|$ should be larger. In the limit of $\xi = 0$, t can be defined in terms of the horizontal and vertical scattering angles of the proton as:

$$t = -(p \times \theta_x^*)^2 - (p \times \theta_y^*)^2.$$

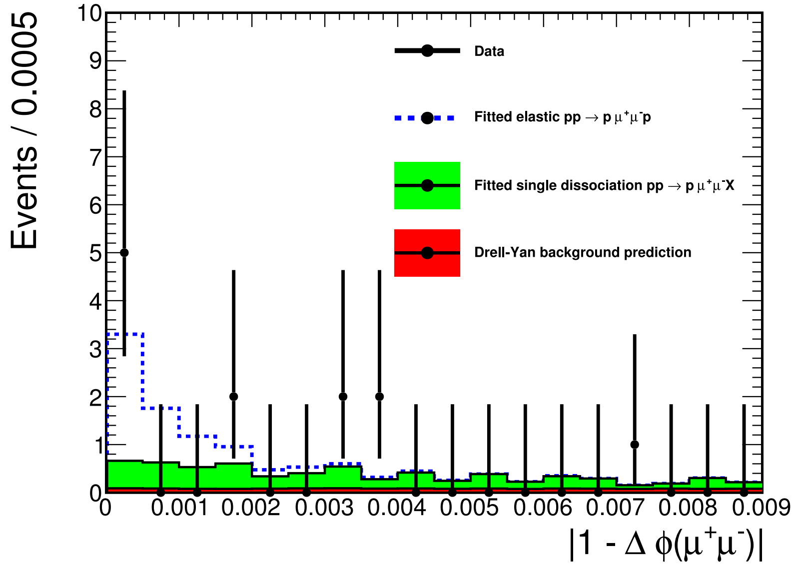

Figure 4.40: Fit to the acoplanarity distribution of the 12 events in the $\mu\mu$ signal region. The error bars represent the Garwood intervals. The elastic and single dissociation yields are free parameters, with template shapes based on the LPAIR MC. The background distribution is normalized to the value expected in the data, with a shape derived from the Drell-Yan MC.

With the current proton reconstruction, the CT–PPS detectors are sensitive to the vertical component of the scattering angle, θ^*_y. Table 4.13 lists the estimated θ^*_y values of the 12 signal events, with the reconstruction and beam divergence uncertainties.

One event (275918:432304802) has a θ^*_y value approximately 3.5σ from 0, making it compatible with the background hypothesis. Two events have a θ^*_y value differing from zero at the 2-3σ level in at least one of the two RPs, while the other events have θ^*_y within 2σ of 0.

Run:LS:Event	Sector	θ^*_y (μrad)	$\sigma(\theta^*_y)$ (reco + beam divergence)	n_σ
273730:1646037324	45-FAR	-0.4 ± 85.1	87.4	0.0
274971:814088551	56-NEAR, 56-FAR	28.2 ± 12.2, 26.6 ± 9.0	23.4, 21.9	1.2, 1.2
274971:883153054	45-NEAR	21.6 ± 5.3	20.7	1.0
275125:778836261	56-NEAR, 56-FAR	5.5 ± 6.6, 5.2 ± 5.3	21.1, 20.7	0.3, 0.3
275918:432304802	56-NEAR, 56-FAR	-84.9 ± 15.2, -81.2 ± 12.1	25.1, 23.4	3.4, 3.5
275920:524083123	45-FAR	74.1 ± 33.9	39.4	1.9
279766:2754611755	45-NEAR, 45-FAR	-82.2 ± 27.2, -84.4 ± 47.6	33.8, 51.6	2.4, 1.6
279841:518378884	45-NEAR, 45-FAR	-12.6 ± 22.3, -8.8 ± 13.8	24.3, 30.0	0.4, 0.4
279841:1697032699	56-NEAR, 56-FAR	-6.9 ± 6.7, -7.3 ± 5.6	21.1, 20.8	0.3, 0.4
279844:258097039	45-NEAR, 45-FAR	-25.4 ± 53.5, -20.5 ± 23.8	57.1, 31.1	0.4, 0.7
280017:783978922	45-NEAR, 45-FAR	86.6 ± 29.8, 80.2 ± 21.7	35.9, 29.5	2.4, 2.7
280191:1002667118	45-fAR	70.8 ± 41.5	46.0	1.5

Table 4.13: θ^*_y values for the signal region candidate events.

4.8 Results (dielectron channel)

The correlation between $\xi(ee)$ and the ξ value measured in CT–PPS is shown in Fig. 4.41. The error bars represent the 3.9% $\xi(ee)$ resolution, and the 5.5% uncertainty on the ξ value of the measured proton track. Figure 4.42 shows the same events with the near and far RPs combined.

A total of 23 events pass all central detector cuts, have a $\xi(ee)$ value within the CT–PPS acceptance and RP track reconstructed in at least one station. The relative difference of $\xi(ee)$ with respect to $\xi(\mathrm{RP})$ for these events is shown in Fig. 4.43, with the $\pm 2\sigma$ window in which the signal peak is expected denoted by the vertical lines.

Eight events are observed in which the measured $\xi(\mathrm{RP})$ in at least one station matches the $\xi(ee)$ value predicted from the electron kinematics within 2σ. Of these, 6 have tracks reconstructed in both the near and far stations of one arm, while 2 have tracks detected in one of the two stations.

A total of 10.5 ± 2.1 (statistical and systematic uncertainties added in quadrature) background events are expected within the acceptance, but outside the 2σ matching window in $\xi(ee)$ and $\xi(\mathrm{RP})$. In the data 15 non-matching events are found. This number is compatible at the 2.2σ level with the nominal background prediction.

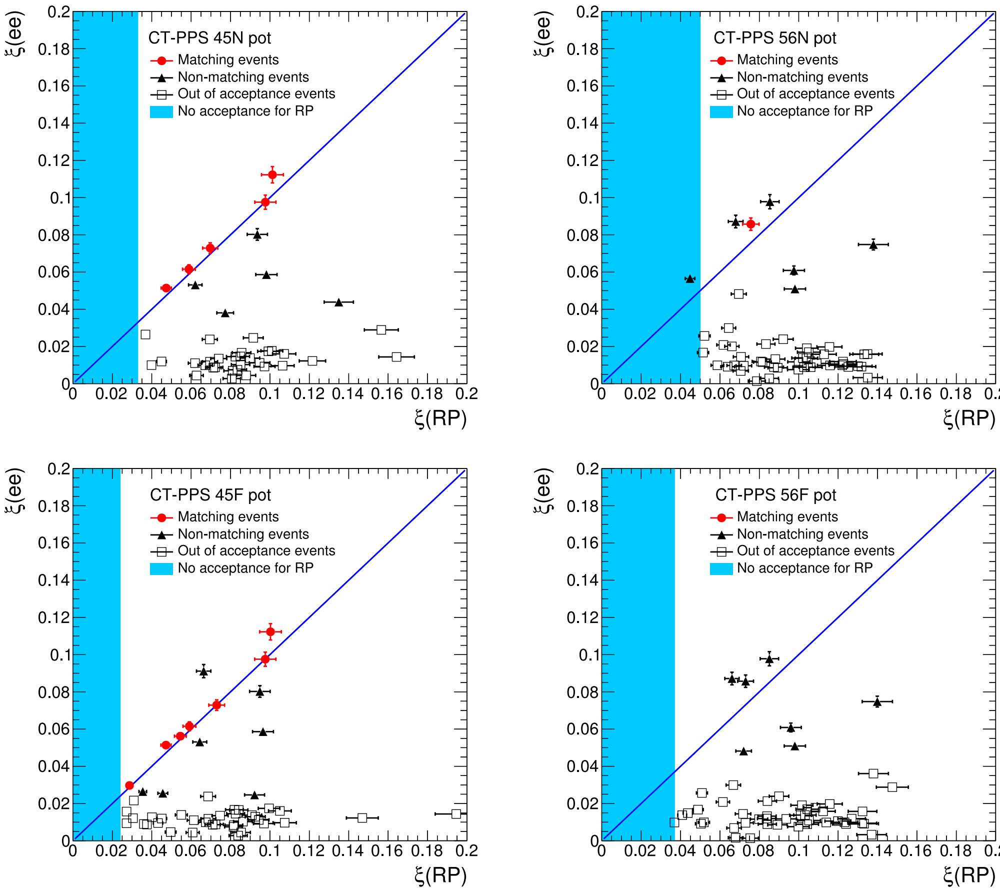

Figure 4.41: Correlation between $\xi(ee)$ and ξ measured in CT–PPS, for each station. The shaded band indicates the region outside the CT–PPS acceptance. The plots correspond to the 45 near (upper left), 56 near (upper right), 45 far (lower left), and 56 far (lower right) stations. The events falling within the 2σ matching window are denoted by red circles, while those outside the 2σ window are indicated by black triangles.

The significance for finding eight matching dielectron events given the background prediction is 2.6σ, again estimated with the Higgs combine tool and considering the systematic uncertainties in the background estimate as nuisance parameters.

4.8.1 Properties of the signal region events

The properties of the 8 selected events are shown in Table 4.14. The vertical position of the RP tracks is within 1.5 mm of zero in six out of eight events, consistent with

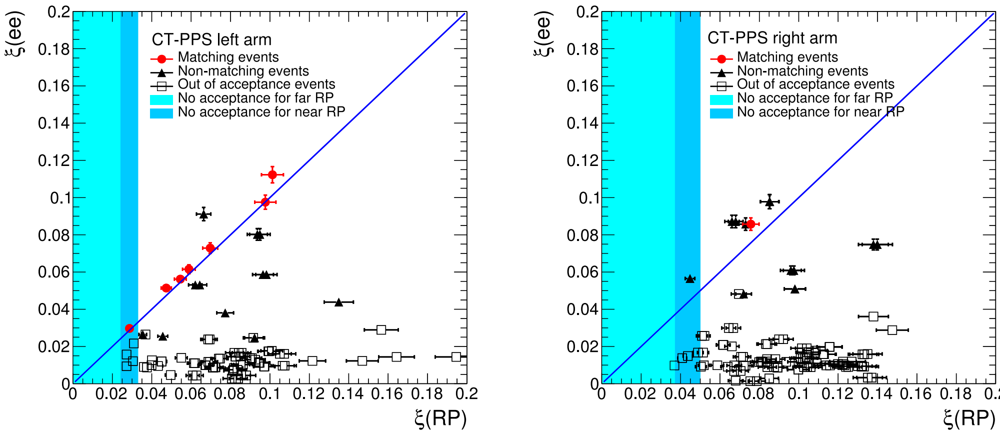

Figure 4.42: Correlation between $\xi(ee)$ and ξ measured in the CT–PPS, for both stations in each arm combined. The 45 (left) and 56 (right) arms are shown. The light shaded band corresponds to the region outside the acceptance of the far RP, while the darker shaded band indicates the region outside the acceptance of the near RP. For the events in which a track is detected in both, the ξ value measured at the near RP is plotted.

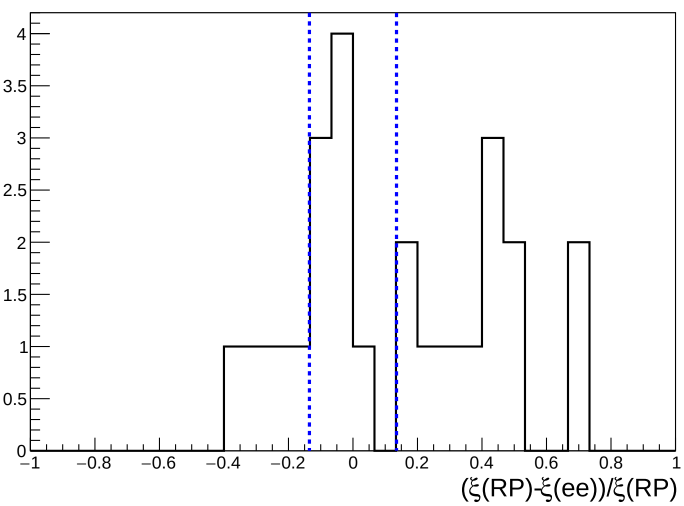

Figure 4.43: Plot of the residuals $(\xi(ee) - \xi(\mathrm{RP}))/\xi(\mathrm{RP})$, for all events with a proton predicted within the CT–PPS acceptance and at least one proton track reconstructed. The blue vertical lines indicate the $\pm 2\sigma$ matching window used to define the signal region. In events with a proton track measured in both NEAR and FAR stations, only the NEAR measurement of ξ is plotted.

Run:LS:Event	$\xi(ee)$	Sector	ξ(RP)	x(RP) [mm]	y(RP) [mm]	$m(\mu\mu)$ [GeV]	$Y(\mu\mu)$
274199:562:1030351654	0.073	45N	0.070	7.23	-0.833	131	1.979
274199:562:1030351654	0.073	45F	0.073	7.56	0.385	131	1.979
274241:172:310425671	0.062	45N	0.059	6.01	-0.628	917	-0.137
274241:172:310425671	0.062	45F	0.059	5.98	0.596	917	-0.137
275283:28:57807841	0.112	45N	0.101	11.14	-0.890	233	1.836
275283:28:57807841	0.112	45F	0.100	10.92	-0.190	233	1.836
275125:236:457316798	0.098	45N	0.098	10.67	-2.795	174	1.983
275125:236:457316798	0.098	45F	0.098	10.58	-1.887	174	1.983
279760:614:1006546188	0.051	45N	0.047	4.74	-0.834	670	-0.003
279760:614:1006546188	0.051	45F	0.047	4.68	-0.557	670	-0.003
280017:149:273631077	0.030	45F	0.029	2.76	-0.432	327	0.167
274199:328:627059009	0.056	45F	0.055	5.47	-0.535	436	0.515
279931:1808:3093224163	0.086	56N	0.076	5.72	-1.612	161	-1.935

Table 4.14: Properties of the signal candidate events. In the events in which a proton track is reconstructed in both the near and far stations, the event appears twice.

the hypothesis of $\gamma\gamma$ production at small $|t|$. The distribution of the events in the $m(e^+e^-), y$ plane is shown in Fig. 4.44. Also shown is the region where the CT–PPS acceptance is non zero. Figure 4.45 shows the one-dimensional mass and rapidity distributions of the selected events.

4.8.1.1 Summary of the events with tracks in only one station

Of the 8 candidate events, two have proton tracks in only one of the two stations. As discussed in Sec. 4.7.1.1, this may happen because of the different acceptance between the NEAR and FAR stations, or because of the reconstruction inefficiency.

Of the two single-station events, one has a track in the 45-FAR station ($\xi = 0.029$) that is out of the minimal acceptance of the 45-NEAR station ($\xi_{min} = 0.033$). Another event has a track within the minimal acceptance of both stations of sector 45; the track is only found in the FAR station ($\xi = 0.055$).

4.8.2 Double-tagged dielectron events

From the generator-level LPAIR Monte Carlo, the cross section for double-tagged events for $p_T(e) > 50$ GeV, $|\eta(e)| < 2.4$, $M_{ee} > 110$ GeV, $\xi(p1) > 0.024$ and $\xi(p2) >$

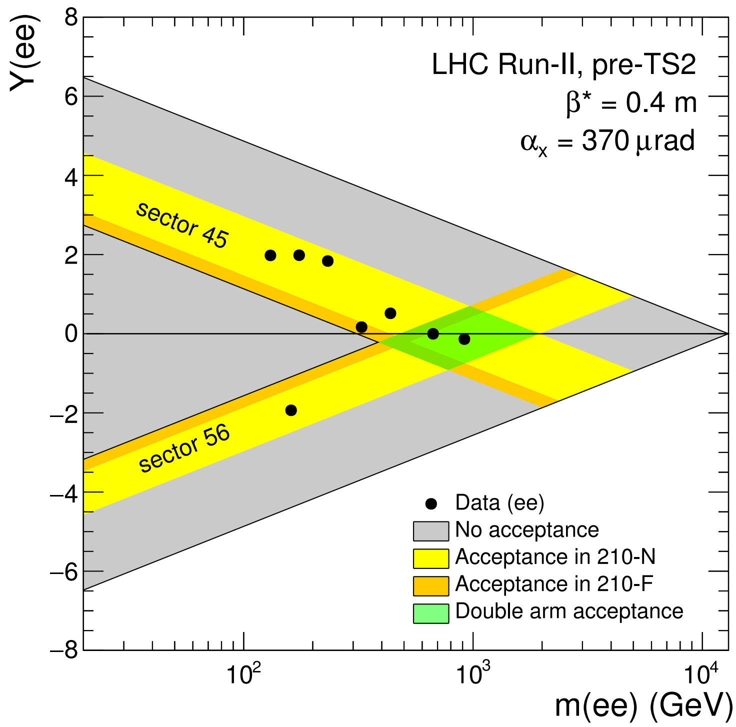

Figure 4.44: Expected pre-TS2 invariant mass-rapidity acceptance (accounting for the asymmetry observed between sectors 45 and 56). The data points overlaid to this figure correspond to the dielectron signal candidate events. The dark yellow and dark green bands correspond to the acceptance of the far stations, while the light yellow and light green bands correspond to the acceptance of the near stations. Following the CMS convention, the positive-rapidity (negative-rapidity) region corresponds to the 45 (56) LHC sector.

0.033, is estimated to be 0.13 fb. Therefore in the sample of 9.4 fb^{-1} used in this analysis, a mean of ~ 1.2 events is expected at most, if the efficiency of the selection cuts and that for reconstructing the proton tracks were 100%. From the simulation, the efficiency for $pp \to pe^+e^-p$ events to pass all the central detector selection criteria is $\simeq 62\%$. Assuming an upper limit on the luminosity-weighted average efficiency for reconstructing the proton tracks in CT–PPS of 50%, fewer than 0.4 double-tagged events would be expected in the current dataset.

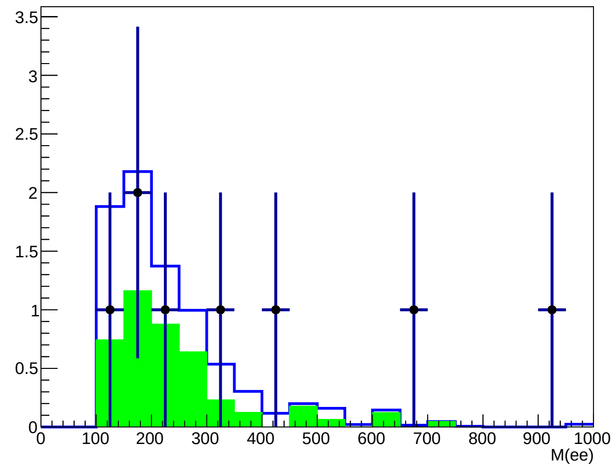

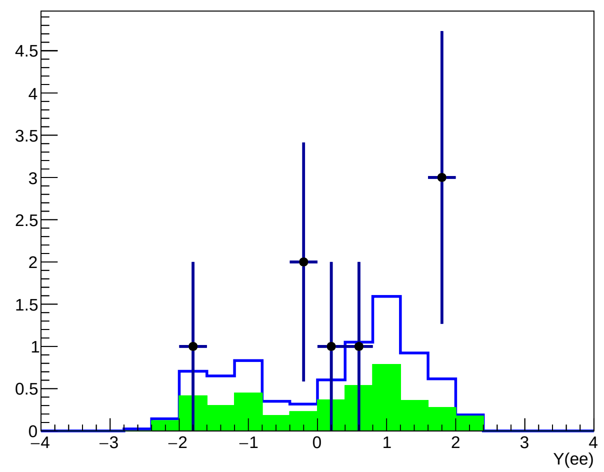

Figure 4.45: Invariant mass (top), and dielectron pair rapidity (bottom) distributions for the final sample of events with matching $\xi(ee)$ and $\xi(\mathrm{RP})$. The blue and green histograms represent the exclusive and semiexclusive contributions predicted by LPAIR, respectively. The signal simulation is shown normalized to the data, with the ξ acceptance cuts applied at the generator-level. The simulation includes neither the effect of radiation damage or other inefficiency in the silicon strips, nor any survival probability suppression. Following the CMS convention, the positive-rapidity (negative-rapidity) region corresponds to the 45 (56) LHC sector in the plots.

Indeed, no events are observed in the data with protons in both arms of CT–PPS, with both ξ values consistent with the electron kinematics measured in the central CMS detectors.

4.8.3 High-mass dielectron events

Two events in the data are in the high-mass region (M =670 and 917 GeV), where the expected Standard Model contribution is very low. According to the LPAIR Monte Carlo, the cross section for single- and double-tagged events in the region $p_T(e) > 50$ GeV, $|\eta(e)| < 2.4$, $M_{ee} > 650$ GeV and $\xi(p1) > 0.024$ is 0.16 fb and 0.07 fb for each of the processes, respectively (without survival probability correction). In the data sample of 9.4 fb^{-1}, assuming selection efficiencies of $\sim$ 28% (single-tagged events) and $\sim$ 62% (double-tagged), a proton track reconstruction efficiency of 50% and taking survival probability into account, this would lead to fewer than 0.2 expected events. This suggests that the two observed events are background.

4.8.4 Vertical component of scattering angle for signal events

The same study of θ^*_y as for the dimuon channel (see Sec. 4.7.3) is performed for the dielectron candidate events.

Two events (275125:457316798 and 279931:3093224163) have a θ^*_y 2.9σ and 4.7σ from 0, making them more compatible with the background hypothesis. All other measurements of θ^*_y are within 1.3σ of 0.

4.8.5 Asymmetry between arms in the e^+e^- sample

The results of the previous section indicate that the one event with a proton detected in Sector 56 has a θ^*_y more consistent with background, and one of the seven events with a proton detected in Sector 45 has a background-like θ^*_y. Two methods are used to estimate the probability for finding 6 events in Sector 45 and 0 events in Sector 56. In both methods the total number of $\mu^+\mu^-$ and e^+e^- events passing the central detector selection is used to determine the ratio $\mathrm{N}(e^+e^-)/\mathrm{N}(\mu^+\mu^-) = 0.79$.

In the first method, the asymmetry in the number of observed dimuon events in the two arms is taken as nominal. This method suffers from the low statistics of the $\mu^+\mu^-$ sample, but includes the effect of the ξ-dependent inefficiencies in reconstructing the protons. In the $\mu^+\mu^-$ channel one event, in Sector 56, has a background-like value of θ^*_y. Removing this event results in 8/11 events (73%) in Sector 45, and 3/11 events (37%) in Sector 56. Combining these ratios with the ratio $\mathrm{N}(e^+e^-)/\mathrm{N}(\mu^+\mu^-) = 0.79$ results in predictions of 6.32 events in Sector 45, and 2.37 events in Sector 56. Poisson distributions with these mean values are then used to predict probability of observing a given multiplicity for each arm. This results in the joint probability distribution shown in Fig. 4.46. The probability of finding exactly 6 events in Sector 45 and 0 events in Sector 56 is estimated to be 1.5%. In comparison, the maximum probability for finding any specific combination of counts is 4.2%.

In the second method, the asymmetry predicted in the elastic e^+e^- LPAIR sample is used, with the generator-level ξ acceptance cuts applied to the protons. This method has smaller statistical uncertainties than the first, but assumes 100% efficiency for reconstructing any proton within the CT–PPS acceptance. This method predicts 64% of the events with protons in Sector 45, and 36% in Sector 56. Combining these percentages with the ratio $\mathrm{N}(e^+e^-)/\mathrm{N}(\mu^+\mu^-) = 0.79$, and normalizing to the 11 total signal-like events in the $\mu^+\mu^-$ channel, results in predictions of 5.6 events in Sector 45, and 3.1 events in Sector 56. As in the first method the Poisson distribution is

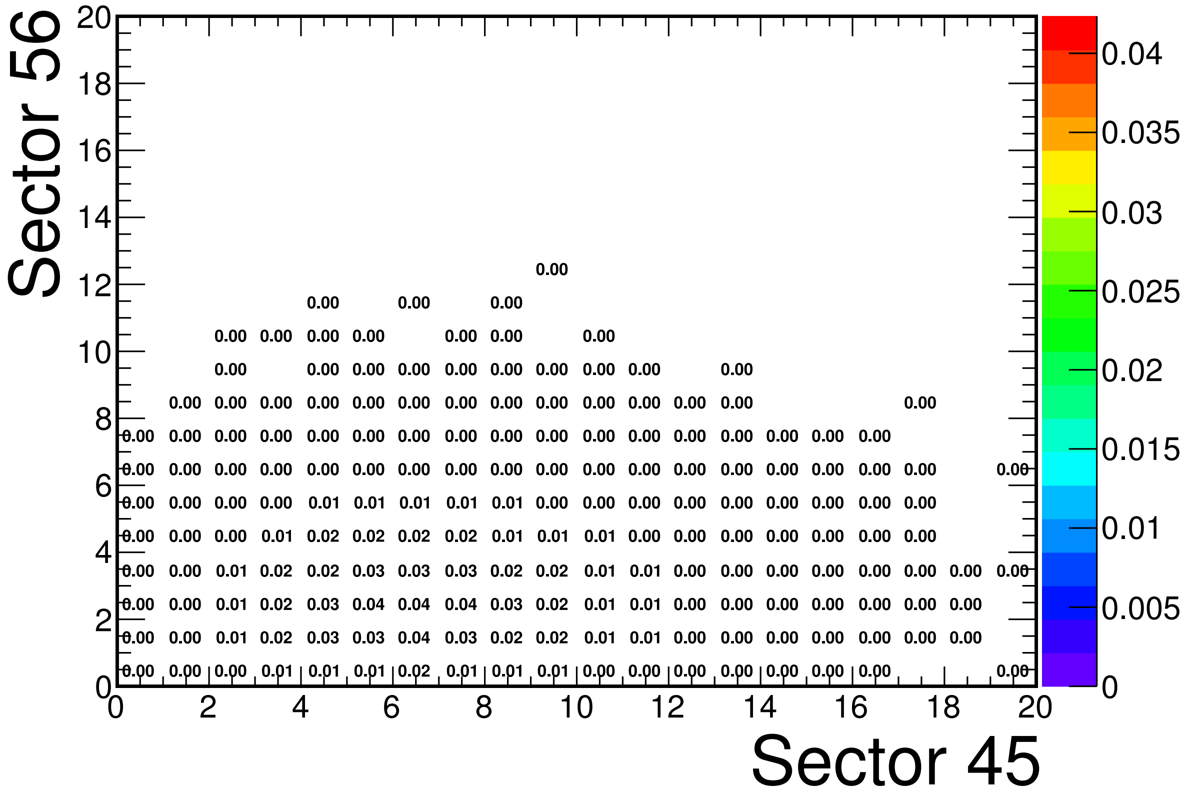

Figure 4.46: Predicted probability for finding any combination of events with protons in Sectors 45 and 56 in the e^+e^- channel, based on the observed number of events in the $\mu^+\mu^-$ channel.

used to predict probability to observe given multiplicity for each arm. This results in the joint probability distribution shown in Fig. 4.47. The probability of finding exactly 6 events in Sector 45 and 0 events in Sector 56 is estimated to be 0.7%. In comparison, the maximum probability for finding any specific combination of counts with this method is 3.8%.

In conclusion, both methods described give comparable estimates, and although the predicted probability to observe zero dielectron events is low, it is only about 3-5 times smaller than that of the most probable multiplicity configuration in each of the arms.

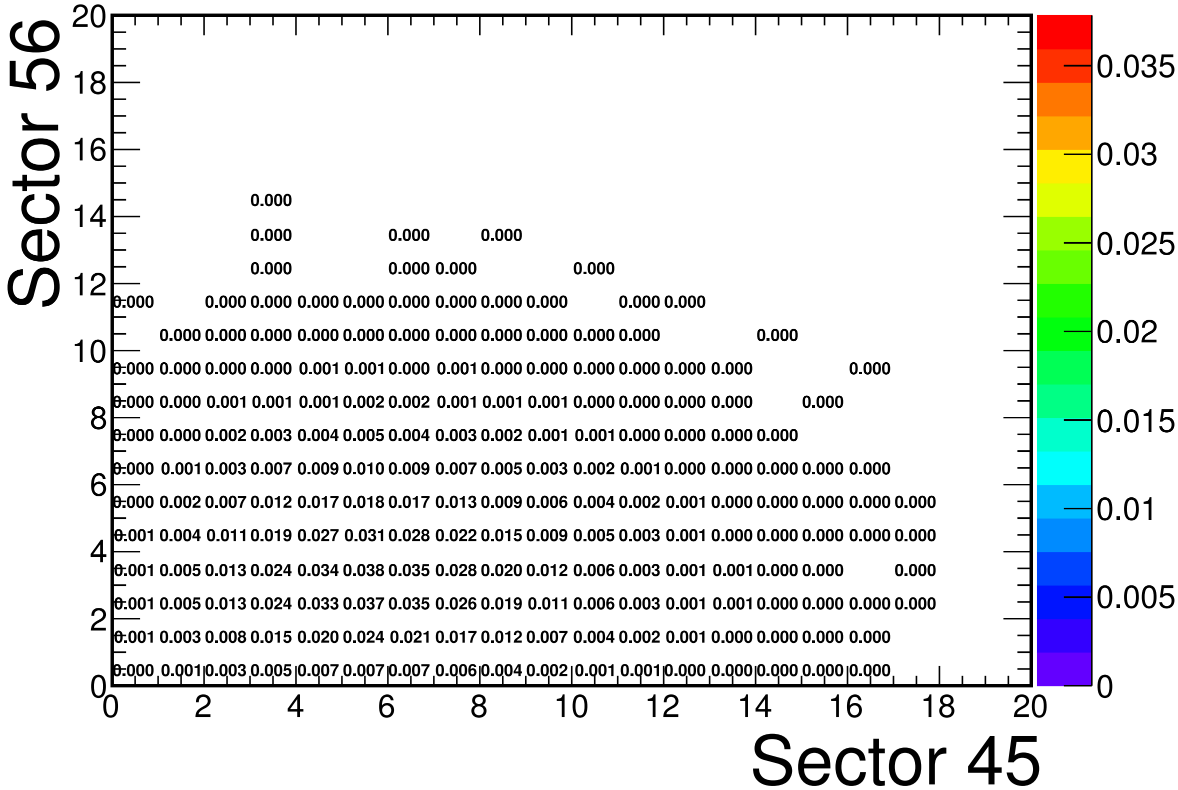

Figure 4.47: Predicted probability for finding any combination of events with protons in Sectors 45 and 56 in the e^+e^- channel, based on the generator-level elastic LPAIR e^+e^- ratio.

4.9 Comparison of predicted and observed yields

No cross section or direct comparison to theory predictions was performed for the publication of this analysis, since the efficiencies had not been studied in detail at the time. In this section the most recent available understanding of the radiation damage, acceptance, and pileup dependence of the proton detection efficiency is used to make a rough estimate of the expected number of events in the dimuon channel.

For this study the best estimate for the number of dimuon candidates observed in the central detectors is used, which allows to derive rapidity dependent survival probability suppression from a fit. This is combined with the LPAIR MC prediction for the proton ξ distribution, as well as the inefficiency sources mentioned in the previous section.

4.9.1 MC predictions

As discussed previously, the default LPAIR cross sections with no survival probability correction significantly overestimate the number of observed events in the central detector. In the following, for the comparison, the absolute prediction for the number of tagged events from LPAIR with a flat survival probability is used, along with the best fit estimate using the candidates observed in the central detector data.

4.9.2 Radiation damage

In order to account for the time-dependent and ξ-dependent effects of radiation damage, a fill from the beginning of 2016 is used. It corresponds to a period before the strips had absorbed a heavy radiation dose, and is used as a reference for the shape of the proton ξ distribution in the data. This shape is then compared to that for the dimuon events throughout the 2016 datasets used for this analysis. The same trigger as for the final analysis is used, in order to capture the correct time dependence and pileup profile. No further offline selection is applied to the muons, so the sample is expected to be dominated by pileup/background tracks in the RPs.

In order to account for the different statistics of the two samples, the shapes of the proton ξ distributions in the reference fill and the 2016 dataset are normalized in the region of $0.10 < \xi < 0.12$, where the occupancy maps indicate that the losses from radiation damage are small. The two histograms are then divided to give an efficiency curve as a function of ξ for each of the 4 RPs.

Two different early fills are chosen as the references for the comparison: one is the initial RP alignment fill and the second is the first standard fill for which the RPs were inserted. The input histograms for the alignment fill and full 2016 data sample are shown in Fig. 4.48. The efficiencies obtained by dividing the histograms are shown in Fig. 4.49, for both the alignment fill and the early high-luminosity fill. For ξ values greater than about 0.05, the results are qualitatively similar for the two reference fills. At lower ξ values, differences are apparent: the 45-FAR distribution is significantly different in the alignment fill and in the first high-luminosity reference fill, and the 45-NEAR distribution is cut off at a higher value (the position of this RP was varying throughout 2016).

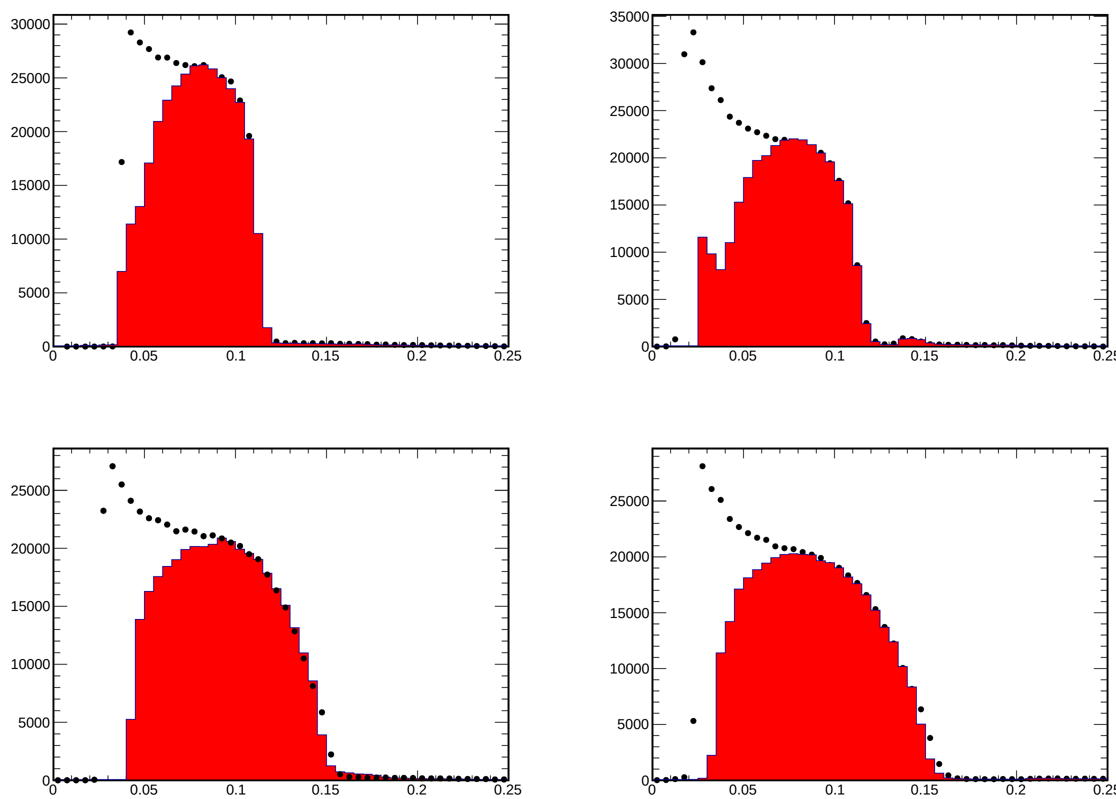

Figure 4.48: ξ distributions in the alignment reference fill (points with error bars) and for the 2016 dimuon data sample (solid histograms). Clockwise from upper left: 45-NEAR, 45-FAR, 56-FAR, 56-NEAR.

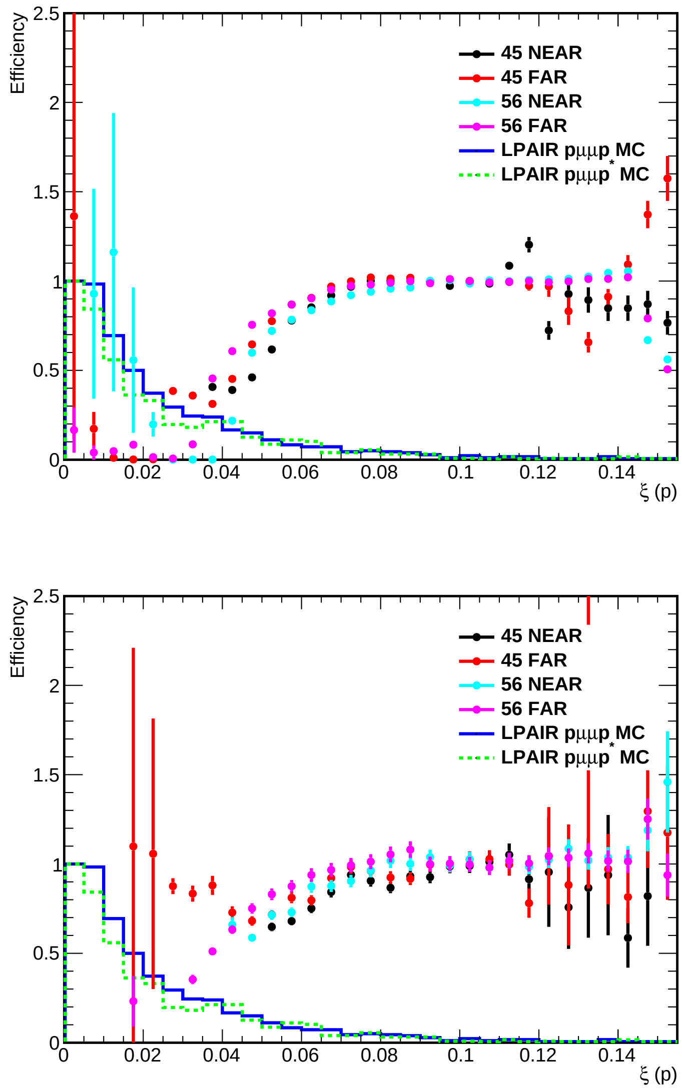

Figure 4.49: ξ-dependent inefficiency due to radiation damage, integrated over the full sample used for the 2016 analysis. The points with error bars are the efficiency for each of the RP stations. The open histograms represent the predicted LPAIR ξ spectra of elastic and single-dissociation events, after applying all cuts on the central detector quantities in the simulation. The LPAIR histograms are arbitrarily normalized to have the maximum at unity in the plots. For clarity, both arms are combined when plotting the MC ξ prediction. Top: results using the alignment fill as reference. Bottom: results using the first high-luminosity fill with the RPs inserted with no orbit margin as reference.

4.9.3 Pileup

Multiple proton tracks cannot be reconstructed in the strip detectors. If the hit multiplicity indicates the presence of more than one track, the event is flagged. The inefficiency due to multiple tracks can be estimated from the rate of multi-track flags in the data. Studies have shown that this is strongly correlated with the pileup rate estimated by CMS, with a mean efficiency of $\sim 70\%$ and a range of $\sim 60 - 85\%$ throughout the 2016 dataset. A value of 70% is thus taken as an approximation of this efficiency for the dimuon sample.

4.9.4 Acceptance

The geometrical acceptance is obtained with LPAIR at generator level assuming a parametrisation of the optics [42]. The acceptance is then determined by counting how many protons arrive at a scoring plane at the detector position, as a function of the generated proton ξ.

4.9.5 Yield predictions and comparison to data

To obtain a final yield prediction, it is assumed that the three effects described in the previous sections (radiation damage, multiple tracks, acceptance) are uncorrelated. The LPAIR spectrum is therefore weighted by each correction, in bins of ξ for the radiation damage and acceptance, and as a flat factor for the pileup. For simplicity, only the FAR RPs are considered because of the better acceptance at low ξ. To make the comparison, the kinematic region $\xi \geq 0.05$ is considered. This is chosen as a tradeoff between limiting the effects of the y-dependent radiation damage and those of the acceptance, while retaining enough events to perform the comparison.

Tables 4.15-4.16 show the predicted and observed yields for $\xi \geq 0.05$ when either the alignment fill or the early high-luminosity fill is used as a reference for the radiation

RP	Elastic prediction from fit (from theory)	Single-diss. prediction from fit (from theory)	Total prediction from fit (from theory)	Data
56 FAR	1.5 (2.6)	3.3 (4.4)	4.8 (7.0)	4 (1 background-like θ_y^*)
45 FAR	1.7 (2.9)	3.4 (4.6)	5.1 (7.5)	5
Sum	3.1 (5.5)	6.5 (9.0)	9.9 (14.4)	9

Table 4.15: Predicted vs. observed number of matching dimuon events in the FAR RPs, when the alignment fill is used as a reference for the radiation damage. The predictions from the fitted suppression factor and from the theoretical calculation with a flat survival probability are shown (in parentheses). The backgrounds are not subtracted from the data.

RP	Elastic prediction from fit (from theory)	Single-diss. prediction from fit (from theory)	Total prediction from fit (from theory)	Data
56 FAR	1.6 (2.7)	3.4 (4.5)	5.0 (7.2)	4 (1 background-like θ_y^*)
45 FAR	1.5 (2.6)	3.1 (4.1)	4.6 (6.8)	5
Sum	3.1 (5.3)	6.5 (8.6)	9.6 (14.0)	9

Table 4.16: Predicted vs. observed number of matching dimuon events in the FAR RPs, when the early high-luminosity fill is used as a reference for the radiation damage. The predictions from the fitted suppression factor and from the theoretical calculation with a flat survival probability are shown (in parentheses). The backgrounds are not subtracted from the data.

damage estimate. The predictions are given for both the fitted rapidity-dependent survival probability factor from the data, and in parentheses for the theory prediction with a flat survival probability suppression. The backgrounds are not subtracted from the data yields. The predictions are normalized to the integrated luminosity of 9.4 fb^{-1} used for the present analysis.

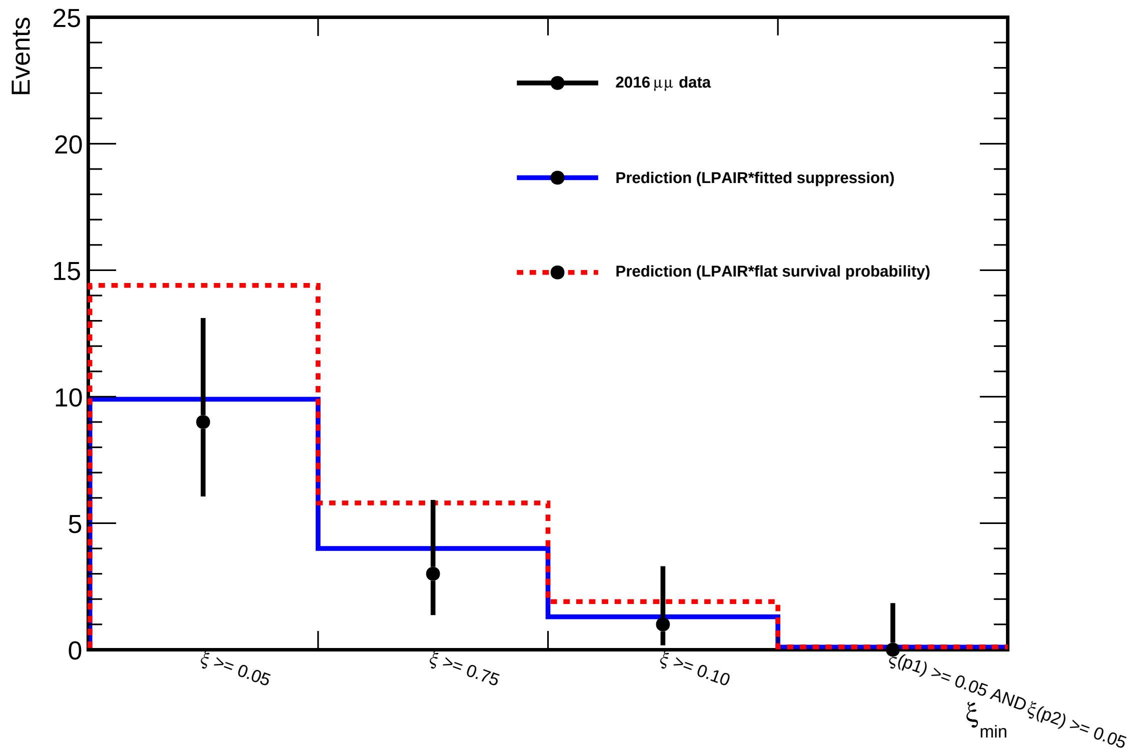

Figure 4.50: Predicted vs. observed number of matching dimuon events in the FAR RPs, as a function of the minimum ξ. The radiation damage corrections are applied using the alignment fill as reference. The predictions are shown both for a flat survival probability (dashed lines), and for the rapidity-dependent suppression factor fitted from the data (solid lines). The data points are plotted with Poisson statistical uncertainties, with no systematic errors. The first 3 bins show the results for the OR of either side, while the last bin shows results when requiring that both protons be detected; the error bars are correlated between the bins.

Figure 4.50 shows the comparison of the predicted and observed yields as a function of the minimum ξ cut. The first three bins show the results for the case where a proton is detected in either the 45 or 56 arms, neglecting the small contribution from events with both protons detectable. The last bin in the plot shows the double tag case where both protons have $\xi \geq 0.05$. In this case the procedure for the predictions is the same, except that the ξ's of the two protons from the LPAIR elastic sample are filled in a 2-d histogram for each event, and the radiation damage corrections are applied to each $\xi(p1), \xi(p2)$ bin of this histogram.

Both methods used to derive the predictions give comparable results and are in good agreement with the yield observed in the data.

4.9.5.1 e^+e^- channel

The previous comparisons were performed for only the $\mu^+\mu^-$ channel. For the e^+e^- channel the full study is not repeated, but instead the predictions are scaled by the ratio of $e^+e^-/\mu^+\mu^-$ yields observed in the central detector, assuming the proton efficiencies are the same for the two channels.

Figure 4.51 shows the comparison of the predicted and observed yields for the e^+e^- and $\mu^+\mu^-$ channels combined as a function of the minimum ξ cut. As in the dimuon case, the backgrounds are not subtracted from the data in the plot. The predicted yield in the two channels combined agrees well in all ξ bins with the one observed in the data.

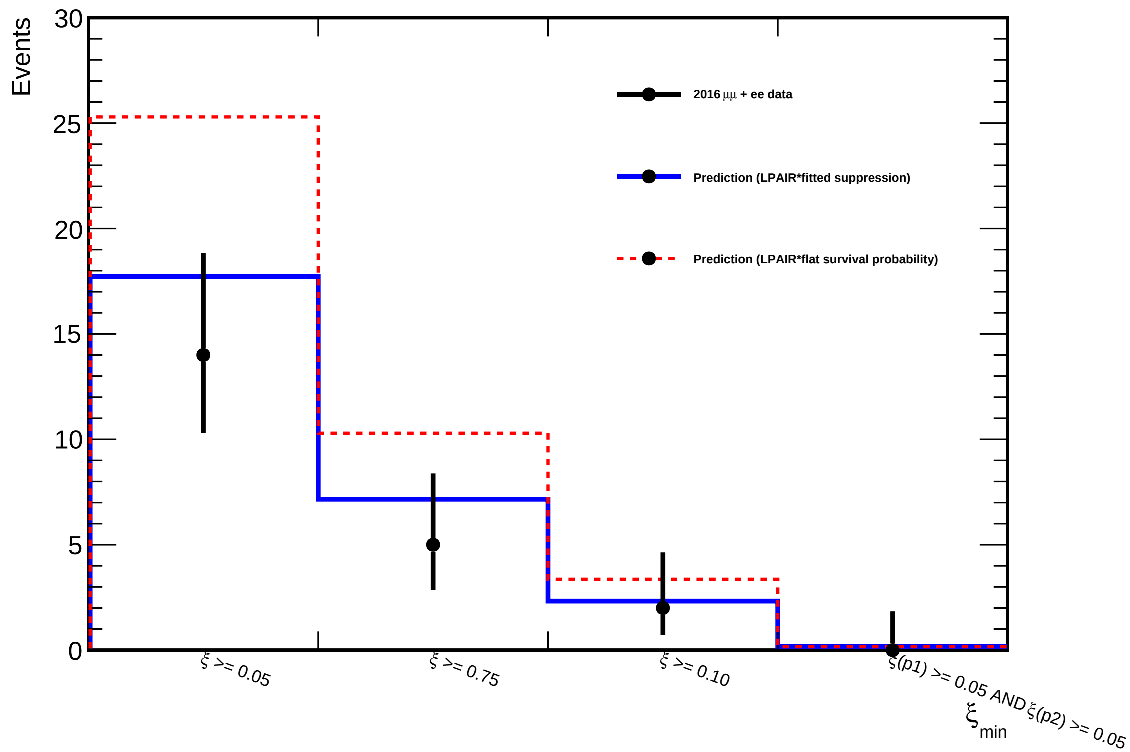

Figure 4.51: Predicted vs. observed number of matching dimuon+dielectron events in the FAR RPs, as a function as a function of the minimum ξ. The radiation damage corrections are applied using the alignment fill as reference. The predictions are shown both for a flat survival probability (dashed lines), and for the rapidity-dependent suppression factor fitted from the data (solid lines). The data points are plotted with Poisson statistical uncertainties, with no systematic errors. The first 3 bins show the results for the OR of either side, while the last bin shows results when requiring that both protons be detected; the error bars are correlated between the bins.

4.10 Combined results

4.10.1 Signal significance

The significance of the combined dimuon and dielectron signal is estimated using the HiggsCombine tool [84] with HybridNew method. The luminosity uncertainty and the theory uncertainty on the double dissociative survival probability are assumed correlated between the two channels. The other sources are assumed independent —

in particular, the modelling of the extra track multiplicity around the dilepton vertex in the Drell–Yan MC and the reweighting uncertainties because of the significant difference in reconstruction performance between the two channels, as was discussed in Sec. 4.7.1.1. The estimated significance of the combined signal excess over background is 5.1 σ. Figures 4.52 and 4.53 show the proton-dilepton ξ correlation and the $m(\ell^+\ell^-)$ vs $y(\ell^+\ell^-)$ distribution for both the dimuon and the dielectron channels combined.

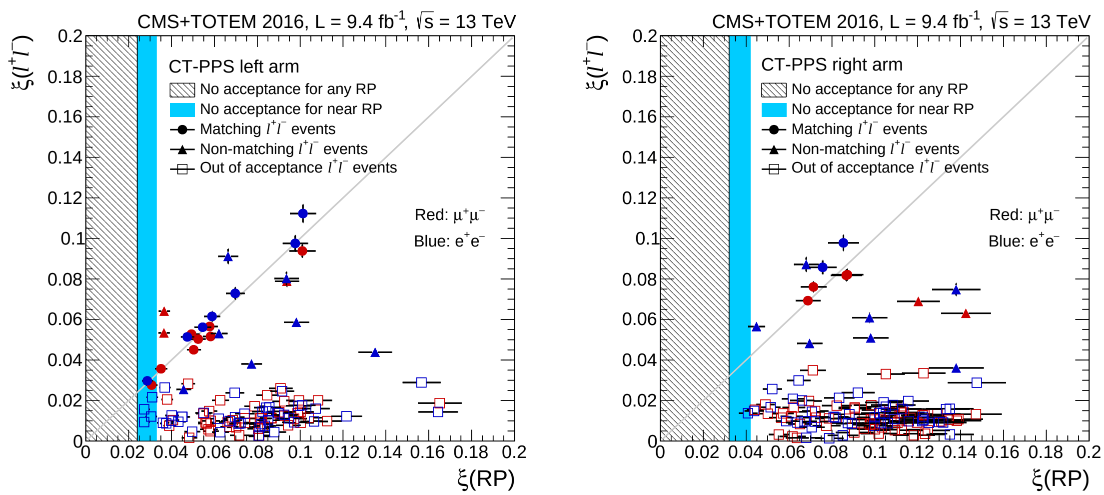

Figure 4.52: Correlation between the fractional values of the proton momentum loss measured in the central dilepton system, $\xi(\ell^+\ell^-)$, and in the RPs, $\xi(\mathrm{RP})$, for both RPs in each arm combined. The 45 (left) and 56 (right) arms are shown. The hatched region corresponds to the kinematical region outside the acceptance of both the near and far RPs, while the shaded (pale blue) region corresponds to the region outside the acceptance of the near RP. For the events in which a track is detected in both, the ξ value measured at the near RP is plotted. The horizontal error bars indicate the uncertainty of $\xi(\mathrm{RP})$, and the vertical bars the uncertainty of $\xi(\ell^+\ell^-)$. The events labeled "out of acceptance" are those in which $\xi(\ell^+\ell^-)$ corresponds to a signal proton outside the RP acceptance; in these events a background proton is detected with nonmatching kinematics.

4.10.2 Fraction of dissociation events

The fractions of the exclusive and single proton dissociative contributions in the final sample of matching events are estimated by comparing their acoplanarity distribution

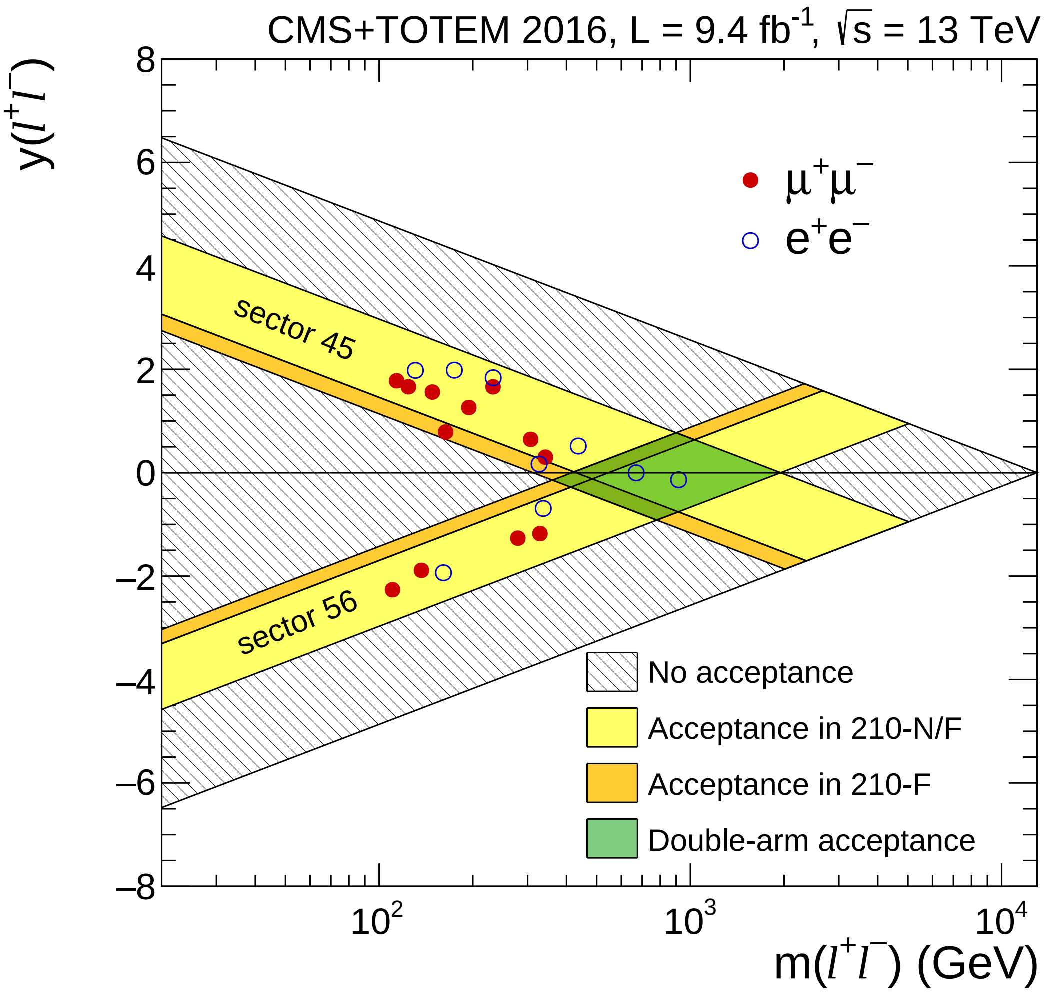

Figure 4.53: Expected acceptance regions in the rapidity vs. invariant mass plane overlaid with the observed dimuon (closed circles) and dielectron (open circles) signal candidate events. The "double-arm acceptance" refers to exclusive events, $pp \to p\ell^+\ell^-p$. Following the CMS convention, the positive (negative) rapidity region corresponds to the 45 (56) LHC sector.

to those expected for the two classes of events in LPAIR, following the same method discussed in Secs. 4.3.4 and 4.9.

The combined fit to the acoplanarity distribution for the fractions of elastic and single dissociation events is shown in Fig. 4.54. In order to account for the different resolution of the two channels, the bin width is increased to 0.001, $\sim 2\sigma$ of the resolution in the e^+e^- channel. The fit range is also limited to 0-0.006, corresponding to the signal region in the e^+e^- channel. The signal and background template shapes used in the fit are taken from the $\mu^+\mu^-$ MC. The background yield is fixed to the expected value for the combined $\mu^+\mu^-$ and e^+e^- channels in this range, while the elastic and single dissociation contributions are left floating. The best fit results in yields of:

$$N(pp \to p\ell^+\ell^-p) = 4.6 \pm 4.0,$$

$$N(pp \to p\ell^+\ell^-p^*) = 11.3 \pm 5.1.$$

The total number of events is fixed to the value observed in data, and therefore the elastic and single dissociation yields are highly anti-correlated in the fit (correlation coefficient = -0.59).

The resulting prediction that the sample consists of approximately 70% single proton dissociation events is consistent within large uncertainties with the predictions of LPAIR weighted by the rapidity gap survival probabilities. The dominance of single dissociation is also consistent with the lack of a second observed proton in the two high-mass e^+e^- events.

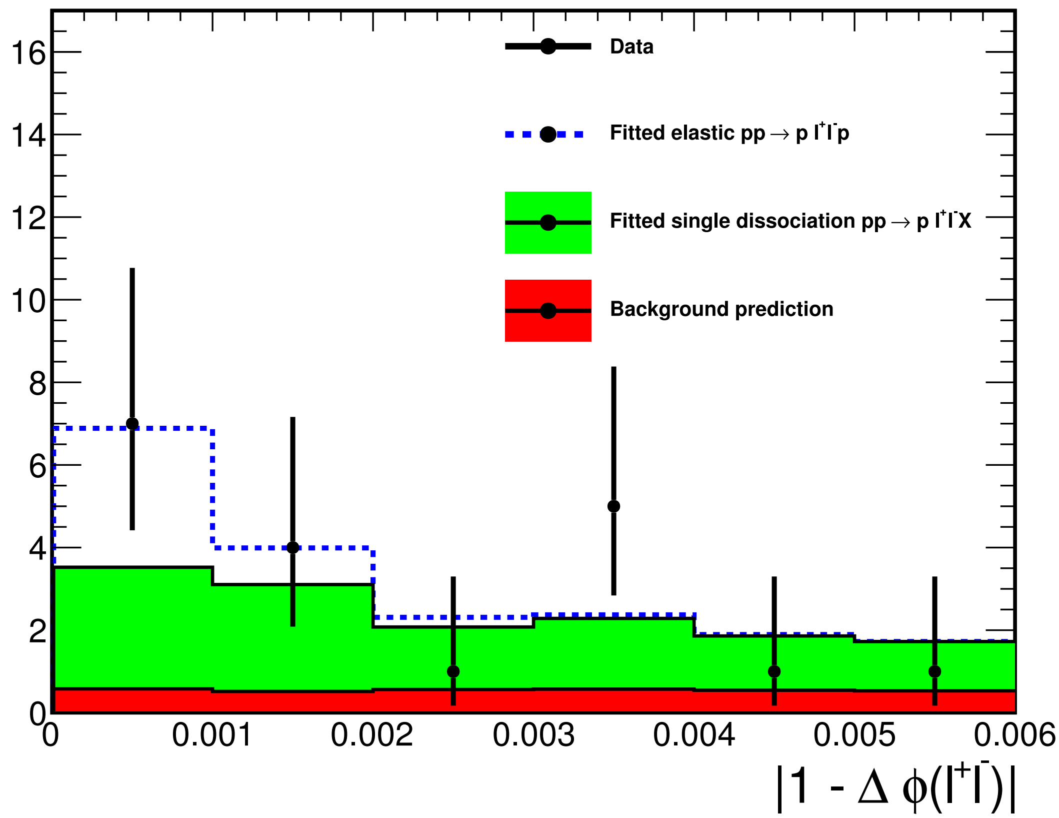

Figure 4.54: Fit to the acoplanarity distribution of the 12 events in the $\mu\mu$ signal region. The error bars represent the Garwood intervals. The elastic and single dissociation yields are free parameters, with template shapes based on the LPAIR MC. The background distribution is normalized to the value expected in the data, with the shape derived from the Drell-Yan MC.

4.11 Summary

The $\gamma\gamma \to \mu^+\mu^-$ and $\gamma\gamma \to e^+e^-$ reactions in $pp \to p\ell^+\ell^-p^{(*)}$ events have been studied together with forward protons reconstructed in the CMS–TOTEM precision proton spectrometer (CT–PPS), using a sample of 9.4 fb^{-1} collected in proton–proton collisions at $\sqrt{s} = 13$ TeV. The Roman Pot alignment and LHC optics corrections have been determined using a high statistics sample of forward protons. A total of 12 $\gamma\gamma \to \mu^+\mu^-$ and 8 $\gamma\gamma \to e^+e^-$ events are observed with dilepton invariant mass larger than 110 GeV, and a forward proton with consistent kinematics. This corresponds to an excess larger than five standard deviations over the expected background from double-dissociative and Drell–Yan dilepton processes. The result represents the first observation of proton-tagged $\gamma\gamma$ collisions at the electroweak scale. The present data demonstrate the excellent performance of CT–PPS and its potential for high-mass exclusive (proton-tagged) measurements. With its 2016 operation, CT–PPS has proven for the first time the feasibility of continuously operating a near-beam proton spectrometer at a high-luminosity hadron collider.

Chapter 5

First look at the 2017 data

5.1 Introduction

The dilepton analysis with the 2016 CT–PPS data has established a way to calibrate the spectrometer, as well as to validate the performance of all reconstruction steps. A similar analysis has been carried out on the 2017 data in order to certify their quality before using them for new physics searches.

Several changes to the detector configuration and running conditions were made in 2017. First, one of the CT–PPS RP stations in each arm was equipped with 3D pixel tracking detectors. The advantageous features of pixel tracking are radiation hardness and the ability to reconstruct multiple tracks, thus increasing the efficiency in high pileup conditions. The data were taken with one RP equipped with Si-strips and one with 3D pixel sensors per arm, located in the 210 far and 220 far stations, respectively.

The average pileup increased in 2017 by about 20% with respect to the previous year, reaching about 33 interactions per bunch crossing. In addition, during 2017, the LHC switched to "luminosity levelling" by changing the beams crossing angle (α_X) during fills. This resulted in a constant change of the optics parameters during the

CT–PPS operation, meaning that the optics corrections must be derived and applied as a function of the α_X value used in a given fill. Finally, as CT–PPS resumed operation after the technical stop with an upgraded set of detectors in changed running conditions, the 2016 alignment no longer applied and the positions of the sensors had to be redetermined.

5.2 The 2017 dataset

The data discussed here were collected during the period June-November 2017 and correspond to an integrated luminosity of 37.5 fb^{-1}.

The HLT triggers used for the online selection were chosen to resemble those in 2016, with the exception of the p_T threshold, which was increased to 43 GeV for the dimuon case[1].

During the 2017 operation, LHC used luminosity levelling to maximize the luminosity delivered to the CMS and ATLAS experiments, while at the same time keeping it appropriate for the ALICE and LHCb experiments, designed for lower values ($\sim\ 10^{30} - 10^{32}$ cm^{-2} s^{-1}). Luminosity levelling is performed by changing the proton beams crossing angle: the beams are moved relative to each other in order to modify the area available for interactions as the bunches pass through each other. The introduction of the levelling technique became necessary because of the high beam intensities, which made it impossible to use the previous approach based on limiting the number of bunches.

The distribution of the crossing angle values in the full 2017 CT–PPS dataset is shown in Fig. 5.1 and the pileup distribution in Fig. 5.2. The most often used crossing angle values during 2017 are α_X =120, 130, 140 and 150 μrad. The shape of the pileup distribution is due to use of several crossing angle values, as the number of

[1]The HLT_DoubleMu43NoFiltersNoVtx patch was used for the dimuon channel, and HLT_DoubleEle33_CaloIdL_MW for the dielectron channel.

interactions per bunch crossing is correlated with the size of the beams crossing area, as discussed above.

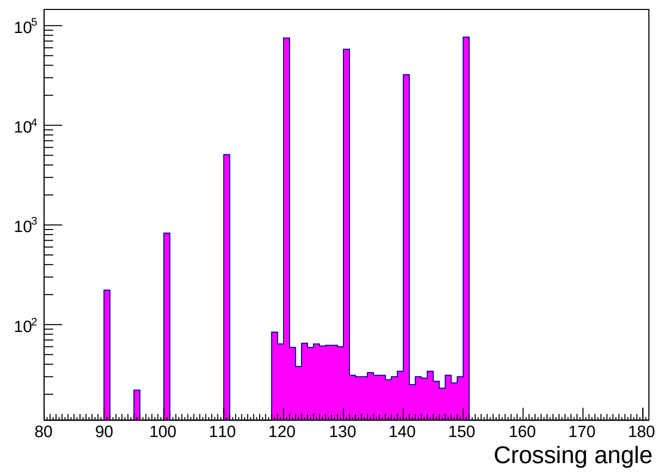

Figure 5.1: Crossing angle distribution in the 2017 dataset, in logarithmic scale.

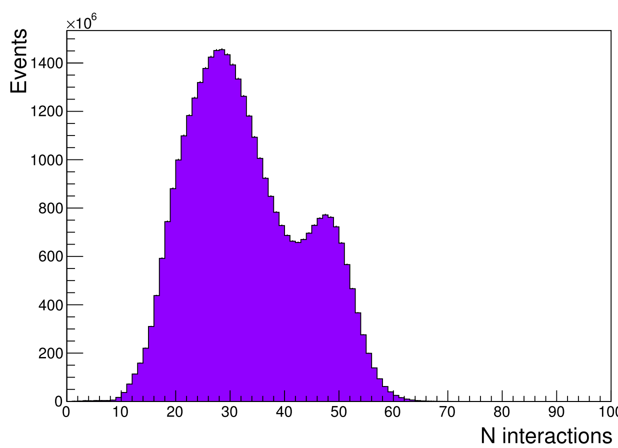

Figure 5.2: Pileup distribution in the full 2017 dataset. The distribution has a double-peak structure because of luminosity levelling during the data taking.

5.3 Alignment and optics

5.3.1 Alignment

An alignment procedure similar to that described in Sec. 3.2 was used for the 2017 data. Several alignment fills were performed with $\alpha_X = 120$, 130 and 140 μrad, respectively. An illustration of the matching of the RMS of the y coordinate of the track impact points in the RPs in the physics and alignment fills is shown in Fig. 5.3.

The alignment corrections are expected to be independent of the crossing angle. To confirm this, the alignment corrections derived for several fills collected at different α_X values were compared. The results for one of the stations in Sector 56 (210 far) are shown in the Fig. 5.4. Indeed no crossing angle dependence is observed in the data within the expected uncertainty of 150 μm. For the present study, the horizontal shifts averaged over all fills are used.

5.3.2 Optics

The optics parametrisation was derived using an approach similar to that of 2016 (see Sec. 3.3.1). An example of the estimated vertical effective length L_y parametrised as a function of ξ at different RPs is shown in Fig 5.5. Several reference samples of elastic events were used to derive the parametrisation, corresponding to the values $\alpha_X = 120, 130$ and 140 μrad. A preliminary constant dispersion estimate, neglecting the non-linear dependence on the trajectory position, is used in the present study. Dispersion values for any other α_X value can be derived with a linear extrapolation based on the reference samples, resulting in a $\delta D_X \simeq 0.46$ cm change per 10 μrad crossing angle.

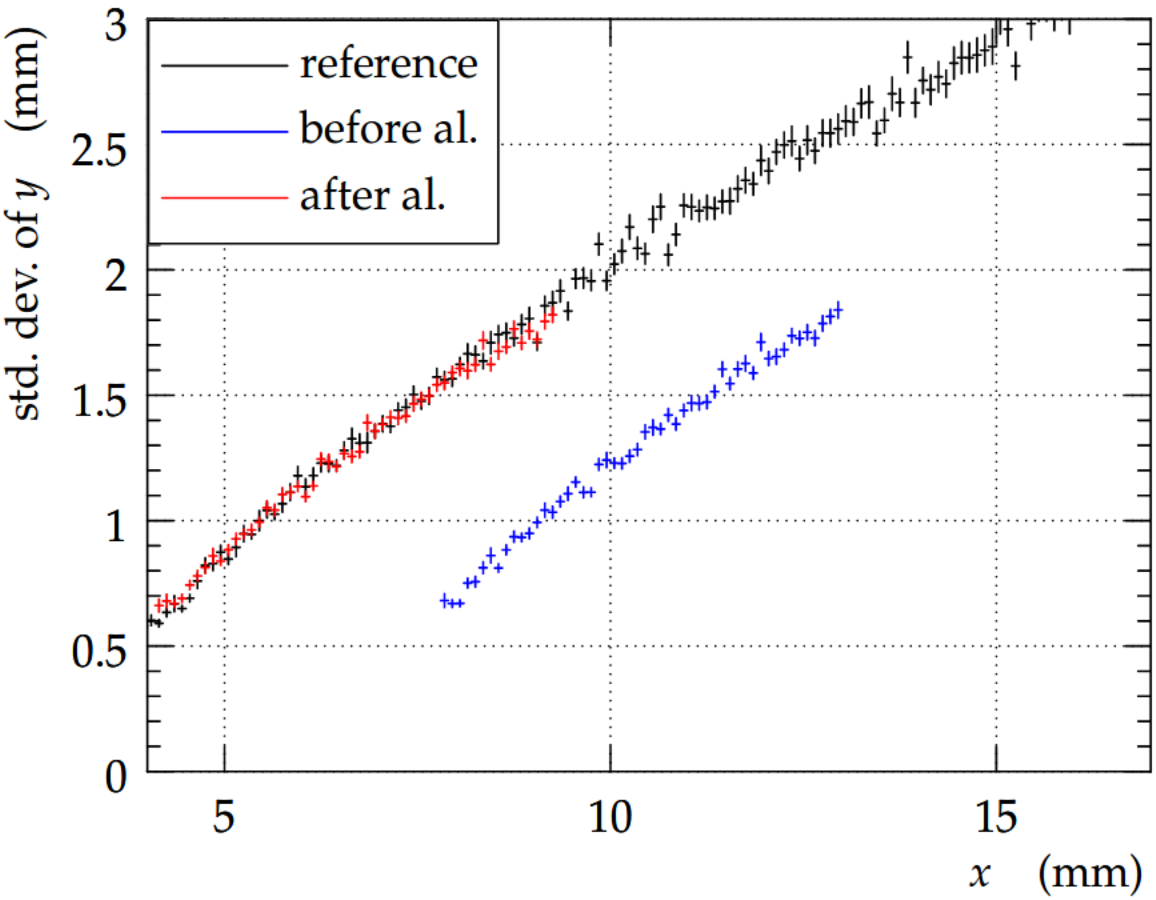

Figure 5.3: Distribution of the profile RMS of the vertical coordinate of track impact points as a function of the horizontal coordinate for the alignment fill (black points), a physics fill before alignment (blue points), and after alignment (red points). The beam center is at $x = 0$ for the black and red points; the x axis origin is undefined for the blue points. The histograms from different fills are rescaled to compare their shapes.

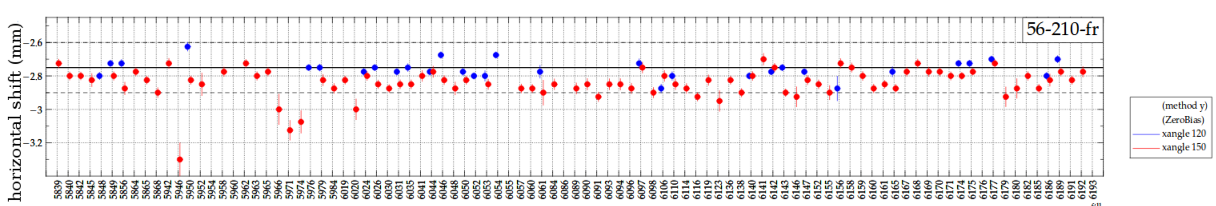

Figure 5.4: Distribution of the alignment corrections for the Sec 56 210 FAR station as a function of the fill number, for data taken at $\alpha_X = 120$ (blue points) and $\alpha_X = 150$ μrad (red points). The dashed lines represent the uncertainty band.

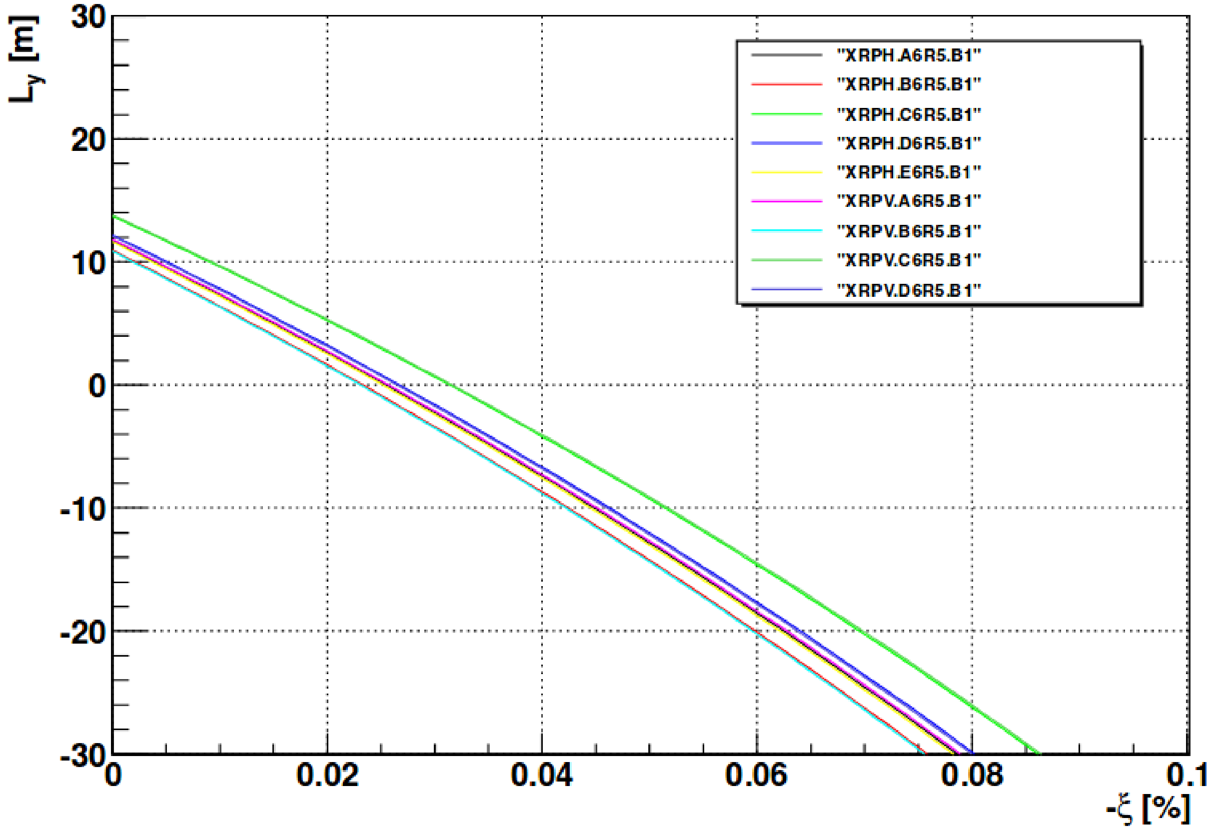

Figure 5.5: Vertical effective length L_y (in meters) as a function of ξ for different RPs positions, calculated with the beam line optics simulation program MADX [43].

5.4 Pixel track multiplicity

From the analysis point of view the main difference of the new CTPPS data with respect to the 2016 ones is the presence of multiple reconstructed tracks in the same event, thanks to the 3D pixel sensors. As discussed in Sec. 4.3, since there is no significant magnetic field, the particle trajectories are linear. The pixel track reconstruction algorithm first groups hits on the different planes of the detector with x and y coordinates within a certain window. All impact point combinations with hits in at least three planes are then used to search for and fit the tracks parallel to the beam. The Si-strips and pixel tracks are reconstructed separately and no global reconstruction is used for the present study.

A classification of the events according to the track multiplicity is shown in Fig. 5.6 as a function of the number of PU vertices. There is a clear correlation between the track multiplicity and pileup: in the high-luminosity conditions of 2017 the percentage of single tracks is only 35-40%. The percentage of showers, defined as ≥ 5 tracks, is directly proportional to PU and at the maximum luminosity reaches 10%. In order to validate the pixel track reconstruction performance, the data used for the dilepton analysis were split into several subsamples based on the track multiplicity, and each subsample was analyzed separately.

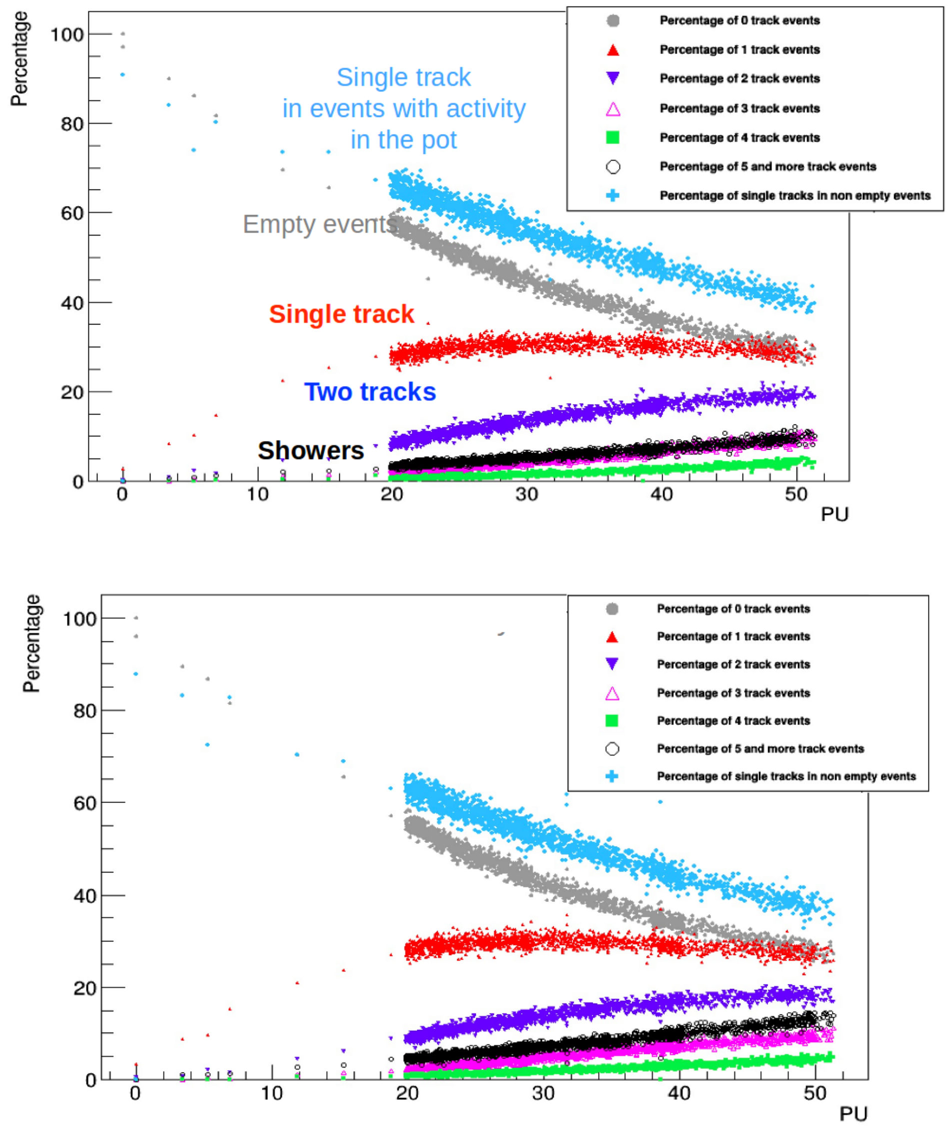

Figure 5.6: Event classification according to the multiplicity of the pixel tracks as a function of the number of PU vertices.

5.5 Results

5.5.1 3D pixels vs Si-strips reconstruction

The reconstructed track multiplicity distribution per arm for the events satisfying the selection requirements is shown in Fig. 5.7. The mean number of tracks is $\sim 1.3 - 1.7$, with the difference between arms reflecting the variation in dispersion between the two beams, which translates into a different acceptance in Sector 45 and 56.

The majority of the tracks reconstructed in the same event by both pixels and strips have a matching x coordinate (Fig. 5.8), with a small amount of hits due to uncorrelated noise and showers.

The $\xi(\mu^+\mu^-)$ vs ξ(RP) correlation plots for a subsample of dimuon events passing the selection and having both a single pixel track and a track measured by the Si-strips are shown in Fig. 5.9. Here again a good correspondence between the measurements of two detectors is found, with a slight shift of the pixel coordinate measurements with respect to those from strips, which reflects the distance between the stations. This can be corrected by taking the scattering angle into consideration. There is an excess of single tracks measured with the pixels, with most extra events at ξ(RP)$\simeq$ $0.02 - 0.03$. This is expected because of the difference in acceptance between the two stations, as illustrated in Fig.5.10, which shows the inclusive proton track ξ distribution reconstructed in each of the stations.

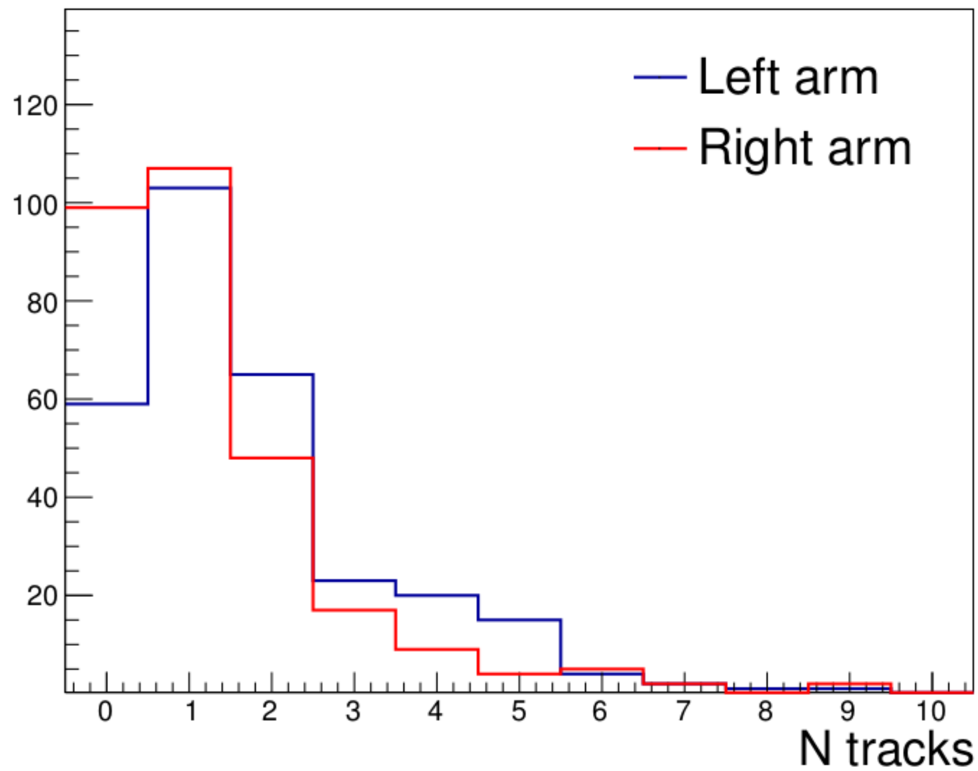

Figure 5.7: The reconstructed pixel track multiplicity distributions per arm, for events passing the selection cuts.

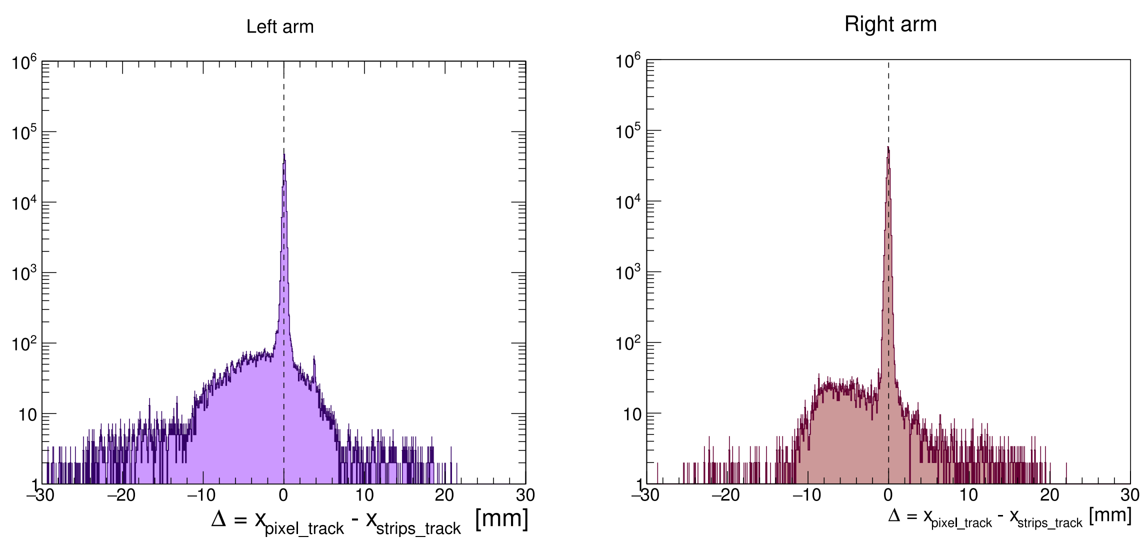

Figure 5.8: Difference between the proton x coordinates measured by the pixel and Si-strip detectors for the same event. The 45 (left) and 56 (right) arms are shown.

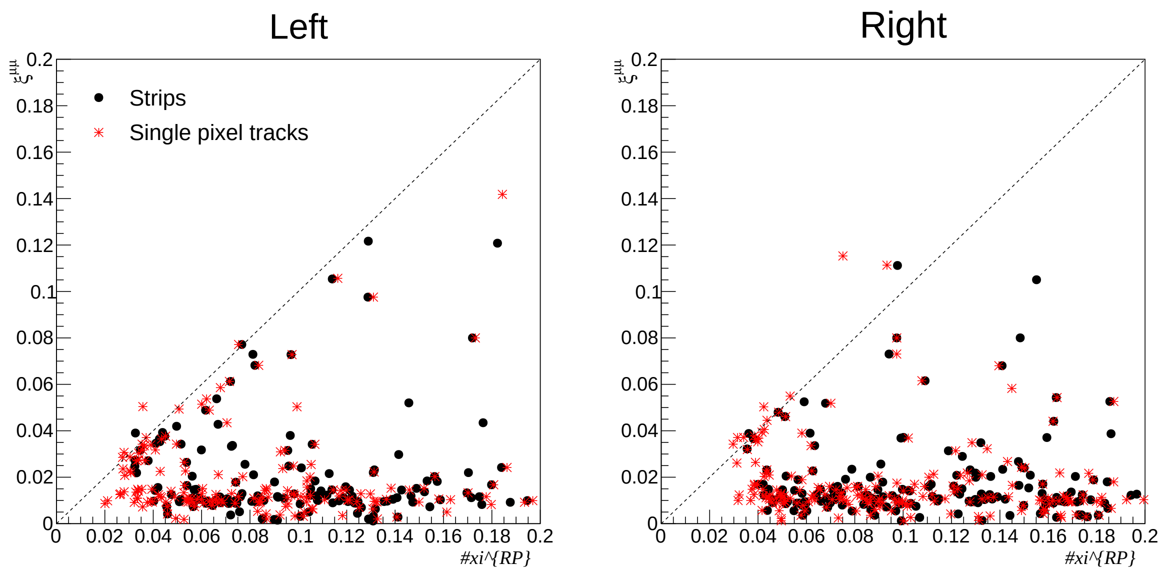

Figure 5.9: Correlation between $\xi(\mu^+\mu^-)$ and ξ(RP) measured in CT–PPS, for both stations on each arm overlaid. The 45 (left) and 56 (right) arms are shown.

g.

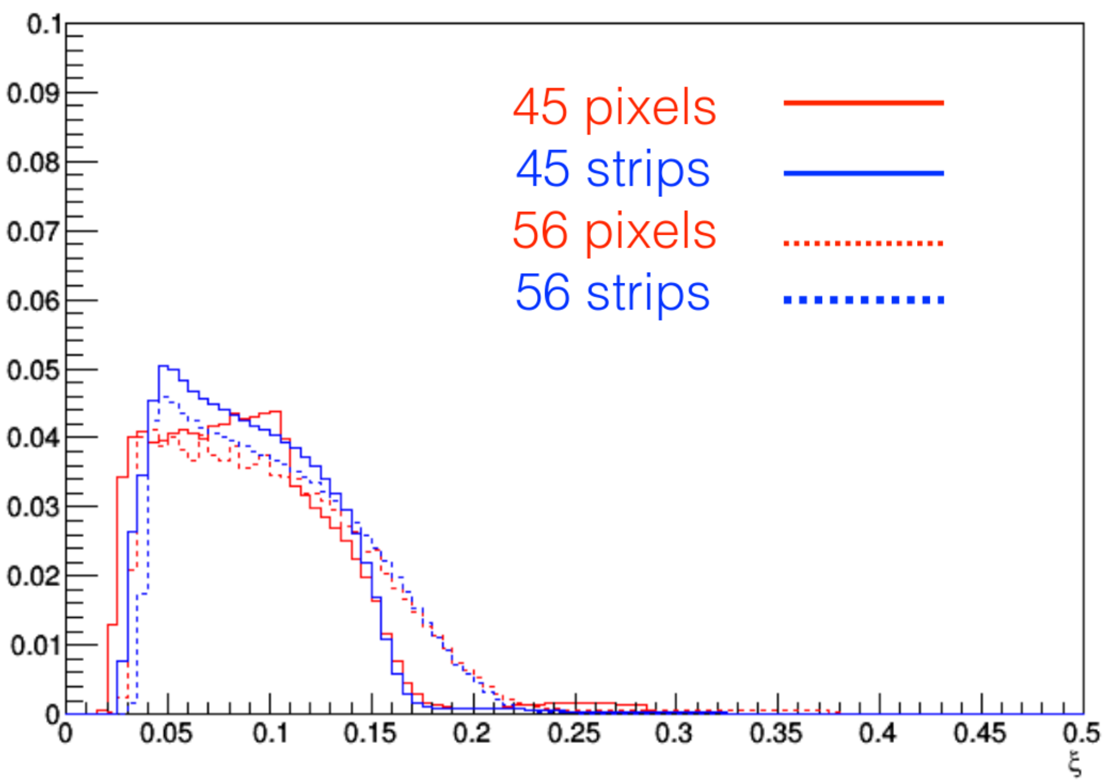

Figure 5.10: Inclusive ξ(RP) spectra as reconstructed by pixel and Si-strip tracking detectors. The 45 (left) and 56 (right) arms distributions are shown. All histograms are normalized to unity.

5.5.2 Correlation between $\xi(l^+l^-)$ and ξ(RP)

The $\xi(l^+l^-)$ vs ξ(RP) correlation plots, using the $N_{tracks} = 1$ sample reconstructed by the pixel detector, are shown in Fig. 5.11, for the dimuon and the dielectorn samples. The error bars show the combined uncertainty of the ξ measurements, corresponding to 5.5% for ξ(RP) and 3.3% (3.9%) for $\xi(\mu^+\mu^-)(\xi(e^+e^-))$; the shaded band around the diagonal represents the matching region corresponding to 2σ of the combined uncertainty of the ξ measurements. A total of 14 (10) events with ξ matched within 2σ is observed in the left (right) arm in the dimuon sample. In the dielectron sample, 17 (10) events are observed in the left (right) arm. Figure 5.12 shows the same correlation plots for the subsample of events with exactly two reconstructed pixel tracks in a given arm – here each event contributes twice, with two points having the same $\xi(l^+l^-)$, but two different ξ(RP) values, derived from each of the reconstructed tracks. Finally, Fig. 5.13 illustrates the ξ correlation for the $N_{tracks} \geq 3$ subsample. As evident from comparison between Figs. 5.11-5.13, the multitrack reconstruction allows to almost double the number of signal candidates with respect to the single track sample. Most of the gain in the signal region is provided by the two-track sample, while higher multiplicity events tend to contain mostly showers and noise, contributing random ξ(RP) values not correlated with the central system.

The mass spectrum of the dilepton events matched within 2σ in $N_{tracks} \leq 2$ samples starts at 110 GeV (corresponding to the dilepton mass cut used for the selection) and extends up to about 1 TeV (Fig. 5.14). Despite the double-arm acceptance region starting around 400 GeV, no double-tagged events were observed in the sample. A generator-level estimate with LPAIR without detector simulation predicts about 7 CEP dilepton events within the CT–PPS acceptance in the 37.5 fb^{-1} of the data. However, this does not include the effect of the survival probability, nor that of acceptance and efficiency.

Figure 5.15 shows the relative difference of $\xi(l^+l^-)$ and $\xi(\text{RP})$ with respect to $\xi(\text{RP})$ for the $N_{tracks} \leq 2$ sample, with the $\pm 2\sigma$ window in which a signal peak is expected denoted by the vertical lines. A clear signal peak can be seen, with a width approximately corresponding to the 2σ uncertainty. It should be noted however that the mean position of the resolution peak is slightly off-centered with respect to zero by about $\sim 10-20\%$ – an effect observed in both the dimuon and the dielectron samples. This indicates the need for additional small alignment corrections, along with further refinement of the optics by including the non-linear terms in the dispersion estimate.

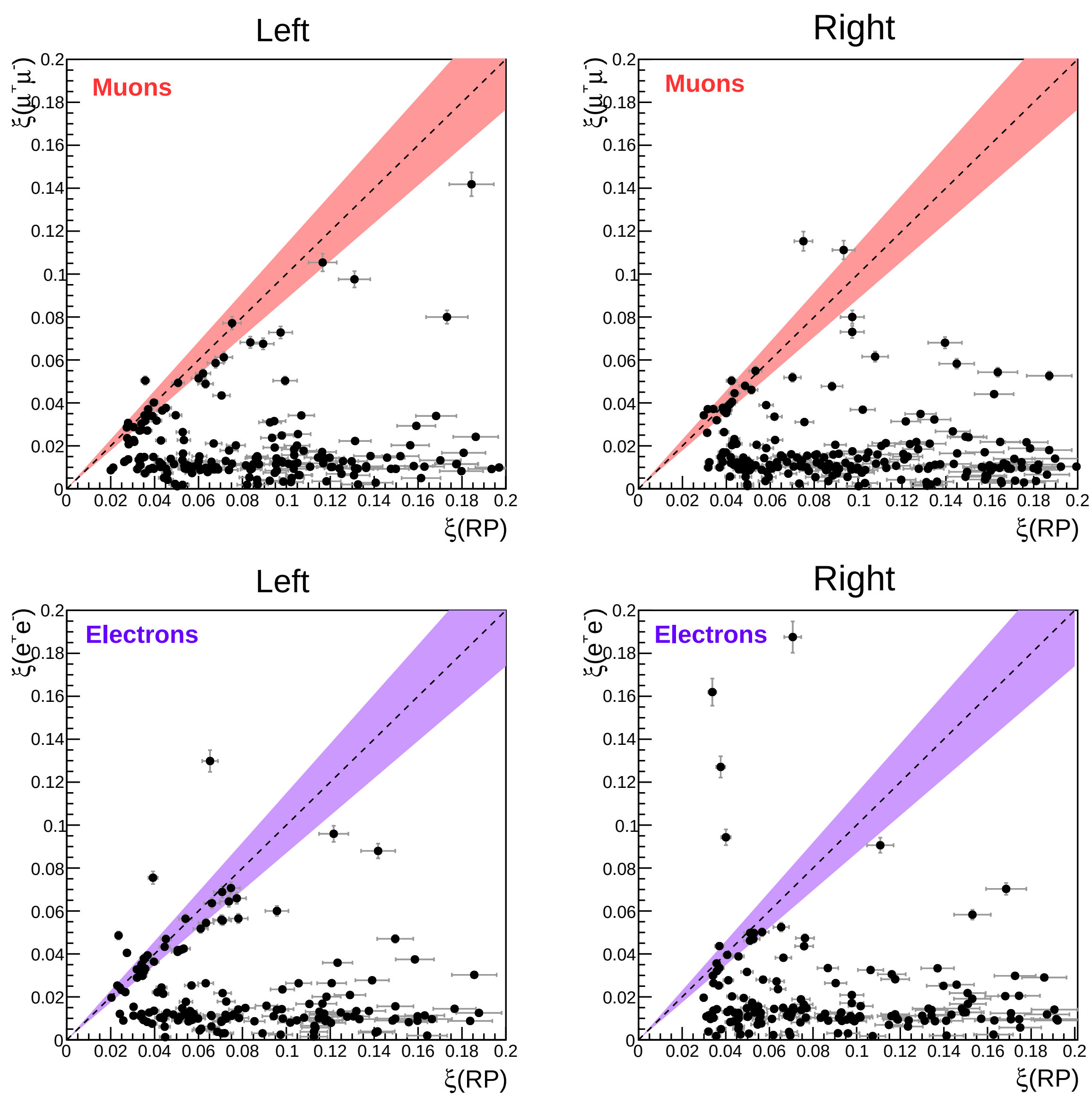

Figure 5.11: Correlation between $\xi(\ell^+\ell^-)$ and ξ measured with the CT–PPS 3D pixel tracker in $N_{tracks} = 1$ sample. The 45 (left) and 56 (right) arms are shown.

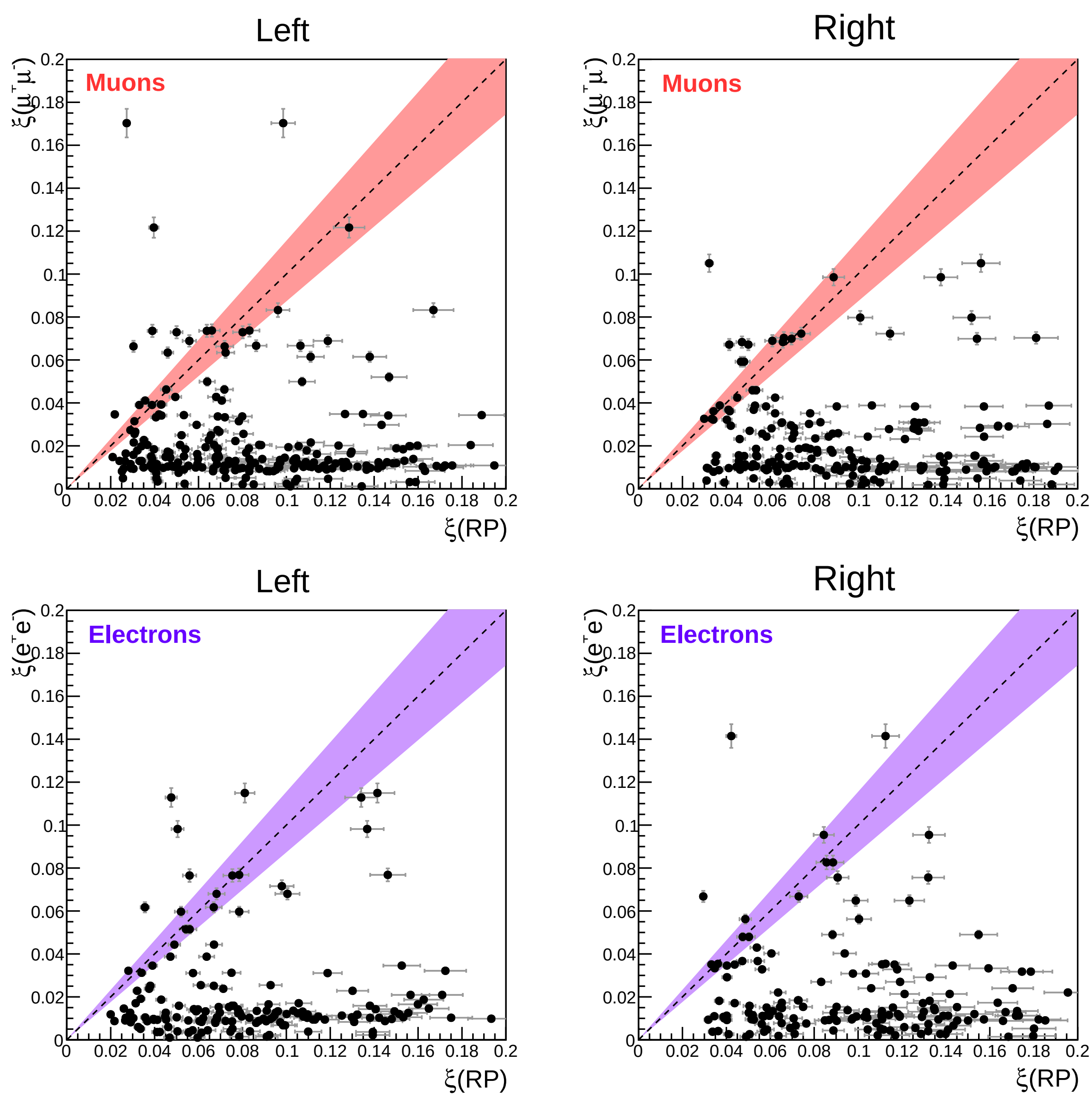

Figure 5.12: Correlation between $\xi(\ell^+\ell^-)$ and ξ measured with the CT–PPS 3D pixel tracker in $N_{tracks} = 2$ sample. The 45 (left) and 56 (right) arms are shown.

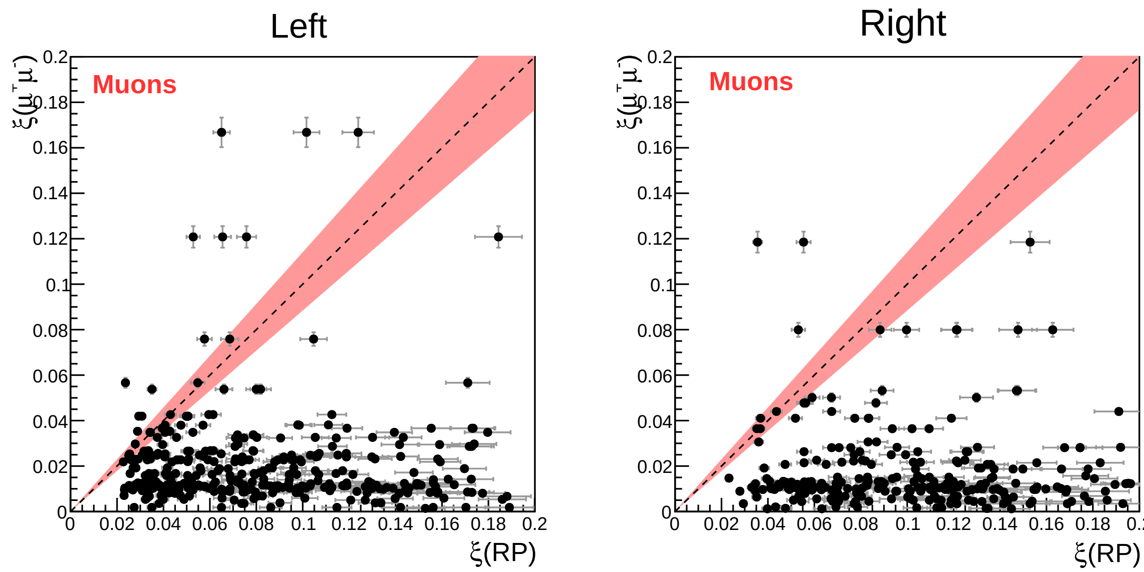

Figure 5.13: Correlation between $\xi(\ell^+\ell^-)$ and ξ measured with the CT–PPS 3D pixel tracker in $N_{tracks} \geq 3$ sample. The 45 (left) and 56 (right) arms are shown.

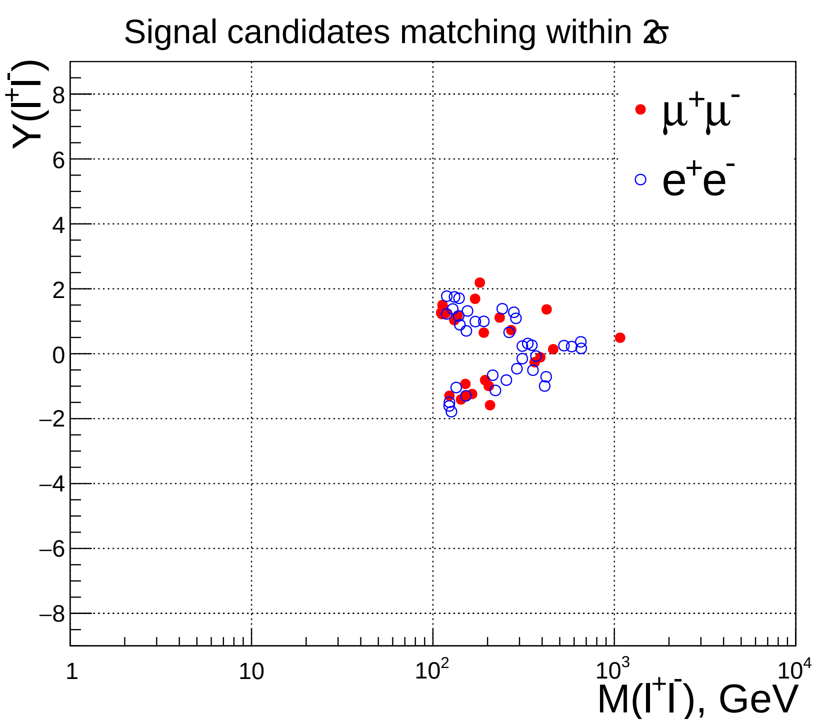

Figure 5.14: Mass versus rapidity distribution of the signal candidates matching within 2σ of the combined uncertainty. Only the events with pixel tracks $N \leq 2$ are shown. Following the CMS convention, the positive-rapidity (negative-rapidity) region corresponds to the 45 (56) LHC sector.

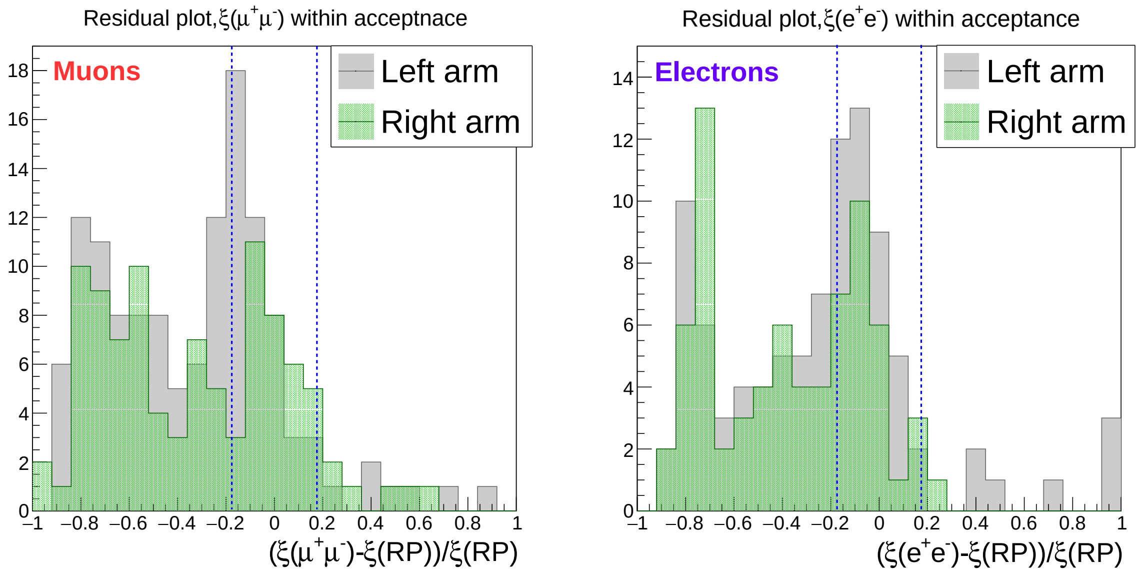

Figure 5.15: Plot of the residuals $(\xi(\ell^+\ell^-) - \xi(RP))/\xi(\mathrm{RP})$, for all events with a proton predicted within the CT–PPS acceptance and ≤ 2 proton tracks reconstructed by the pixel tracker. The blue vertical lines indicate the 2σ matching window used to define the signal region.

5.6 Conclusion

The first look at the 2017 data proves the successful operation of CT–PPS after the upgrade of the tracking system, and confirms the good understanding of its calibration and reconstruction performance. The present study provides a basis for future refinement of the reconstruction methods.

At the time of writing this thesis, activity is ongoing to include non-linear terms in the dispersion estimates, as well as to refine the alignment by introducing fill-by-fill corrections, instead of averaging over the full sample. Another development is the so-called multi-RP reconstruction, which allows reconstruction of scattering angles as well as t, based on the combination of the trajectory measurements by the detector stations in the 210 far and 220 far pots. The multi-RP method is also expected to significantly reduce the uncertainty of the ξ measurement for the single track events.

The 2017 dataset increases the statistics available in 2016 by four times. The total available liminosity in 2016 and 2017 is about 50 fb^{-1}. The data are ready to be analyzed.

Chapter 6

Study of the feasibility of measuring the reaction $pp \to pW^+W^-p$ with CT-PPS

6.1 Introduction

The study of high-energy photon interactions at the LHC opens up the possibility of interesting and novel research. In particular, measurements of the two-photon production of a pair of W-bosons provide sensitivity to the anomalous quartic gauge couplings of the gauge bosons [21,86]. Several measurements have been performed so far [47,87], but none with tagged protons.

The present feasibility study explores the fully hadronic decay channel ($W^+W^- \to q\bar{q}q\bar{q}$), schematically shown in Fig. 6.1, with final state jets boosted and merged into a pair of so-called "fat" jets. The branching fraction of the fully hadronic channel is 45.5%, the highest among all W^+W^- decay modes. The other possible final states are the leptonic ($W^+W^- \to l\nu l\nu$) and semi-leptonic ($W^+W^- \to l\nu q\bar{q}$), representing 43.9% and 10.6% of the total, respectively. The hadronic channel allows full control over the produced system. With the proton measurement, closure of the event kinematics can be achieved, which is useful for both background rejection and the characterization of new phenomena. The main background is expected to be from QCD multijet events [88], with the other sources such as $t\bar{t}$, W+jets and Z+jets production contributing below a few percent.

The conditions of the LHC Run 3 (foreseen in 2021-2023) are assumed, with an expected luminosity of about 300 fb^{-1}.

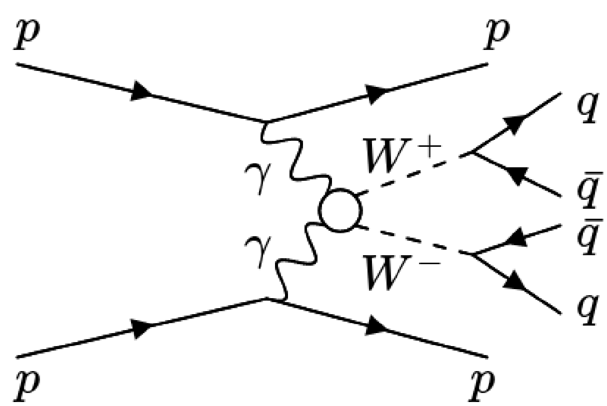

Figure 6.1: Production of W pairs by $\gamma\gamma$ fusion. The fully hadronic decay channel is shown.

6.2 Monte Carlo samples

The FPMC generator [89] was used to simulate the signal ($W^+W^- \to q\bar{q}q\bar{q} \to jets$) via anomalous quartic couplings. FPMC exploits the CompHEP [90] package to generate di-boson production via photon fusion induced by effective Lagrangians due to anomalous couplings between γ and W. The dimension-6 operators in Ref. [91] are the lowest-dimension operators that can produce anomalous couplings. In FPMC the corresponding effective quartic boson couplings are parameterized in terms of a_0^W and a_C^W:

a_0^W/Λ^2 [GeV^{-2}]	σ [pb]
0.5×10^{-6}	2.74×10^{-2}
1.0×10^{-6}	3.44×10^{-2}
2.5×10^{-6}	8.28×10^{-2}
5.0×10^{-6}	0.255

Table 6.1: Cross section predicted by the FPMC generator for each anomalous coupling point for $0.015 < \xi < 0.25$.

$$\mathcal{L}_6^0 = \frac{-e^2}{8}\frac{a_0^W}{\Lambda^2}F_{\mu\nu}F^{\mu\nu}W^{+\alpha}W^-_\alpha, \quad (6.1)$$

$$\mathcal{L}_6^C = \frac{-e^2}{16}\frac{a_C^W}{\Lambda^2}F_{\mu\alpha}F^{\mu\beta}(W^{+\alpha}W^-_\beta + W^{-\alpha}W^+_\beta), \quad (6.2)$$

where Λ denotes the energy scale where new physics is assumed to appear.

Four a_0^W/Λ^2 values were considered for the present study: $0.5 \times 10^{-6}, 1.0 \times 10^{-6}, 2.5 \times 10^{-6}$ and 5.0×10^{-6} GeV^{-2}. The corresponding signal cross sections predicted by FPMC are shown in Tab. 6.1. A constant 90% rapidity gap survival probability factor is included in the simulation.

The QCD multijet background events were generated with PYTHIA8 [62], with the CUETP8M1 [70] tune for parton showering, underlying event, and hadronization.

All samples were processed through the GEANT4-based [63] simulation of the CMS detector. To simulate the effect of pileup for the central variables, additional inelastic events are generated using PYTHIA8 and superimposed on the hard-scattering events. The mean pileup value used in the simulation is 50, as expected in Run 3. The forward proton information in the pileup MC is not saved; data event mixing is used instead, as described below. The scattered protons from the signal MC are propagated through the LHC beam line by means of the CT-PPS optics parametrization described in Sec. 3.3.1. The ξ distributions at generator and reconstructed level are compared in Fig. 6.2.

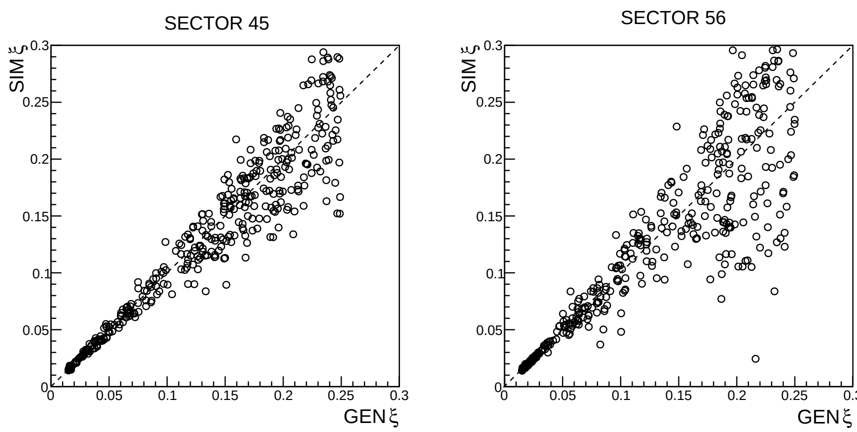

Figure 6.2: The proton ξ reconstructed after the CT-PPS detector simulation versus generator-level proton ξ.

6.3 Jet reconstruction

Because of the high energy of the vector bosons in the events considered, their decay products are merged into a single large-radius jet, leading to a two-jet final state. Jets are reconstructed offline from the reconstructed particles using the anti-k$_t$ jet clustering algorithm [92] with a clustering parameter of $R = \sqrt{(\Delta\eta)^2 + (\Delta\phi)^2} = 0.8$ ("fat" jets) with the FASTJET package [93]. The jet momentum is determined as the vectorial sum of all particle momenta in the jet, and is found from the simulation to be, on average, within 5 to 10% of the true momentum over the whole p_T spectrum and detector acceptance. Additional proton-proton interactions within the same or adjacent bunch crossings can contribute extra tracks and calorimetric energy depositions, increasing the apparent jet momentum. To mitigate this effect, tracks identified as originating from pileup vertices are discarded and an offset correction is applied to correct for the remaining contributions. Jet energy corrections are derived from simulation studies so that the average measured response to jets becomes identical to that of particle level jets. Additional filtering criteria are applied to each jet at the analysis stage to remove jets potentially dominated by instrumental effects or reconstruction failures.

6.3.1 Tagging of W jets

Jet substructure reconstruction algorithms [94] are employed to suppress the SM backgrounds from the hadronization of single quarks and gluons. The two key variables used for jet tagging in the current analysis are the “pruned mass” [94] and the “subjettiness” [95].

- The pruned jet mass m_{pruned} is obtained by removing the softest components of a jet. Jets are reclustered from the original jet constituents by modifying the clustering criteria to remove soft and wide-angle protojets (single particles, or groups of particles already combined in the previous steps). In each recombination step, jet hardness z is defined as $z = \min\{p_T^i, p_T^j\}/p_T^p$, where p_T^i and p_T^j are the transverse momenta of each of the protojets to be combined and p_T^p is that of their combination. The protojet with the lowest p_T^i is ignored if $z < z_{\text{cut}} = 0.1$, and if it is at a distance $\Delta R = \sqrt{(\Delta\eta)^2 + (\Delta\phi)^2}$ larger than $D_{\text{cut}} = m^{\text{orig}}/p_T^{\text{orig}}$ from the axis of the combination of the two protojets, where m^{orig} and p_T^{orig} are the mass and p_T of the original anti-k$_t$ jet. For the jets originating from W decay, the pruned mass is compatible with that of the W boson.

- $N-$subjettiness τ_N is a variable characterizing the jet shape. It corresponds to the p_T-weighted ΔR distance between each jet constituent and its nearest subjet axis:

$$\tau_N = \frac{1}{d_0} \sum_k p_{\text{T},k} \min\{\Delta R_{1,k}, \Delta R_{2,k}, \cdots, \Delta R_{N,k}\}, \tag{6.3}$$

where k runs over all constituent particles. The quantity $d_0 = \sum_k p_{\mathrm{T},k} R_0$ is a normalization factor, where R_0 is the original jet distance parameter. The τ_N value is small for jets with N or fewer subjets, and large if the jet has more than N subjets. The ratio $\tau_{21} = \tau_2/\tau_1$ is used to distinguish between the jets originating from hadronic boson decays and those from QCD processes.

6.4 Selection

Two reconstructed fat jets are required offline, each with $|\eta| < 2.5$. A HLT-like selection is used instead of the trigger simulation, by requiring $p_T^{jet1} > 500$ GeV or $p_T^{jet1} + p_T^{jet2} > 1000$ GeV. These threshold values correspond to the full efficiency turn-on points of the lowest jet p_T triggers currently available in the Run 2 data. No explicit requirement is placed on the dilepton vertex.

The reconstructed protons are required to be within the acceptance range of the CT-PPS 3D pixel tracker in 2017. In terms of ξ this corresponds to the following:

- Sector 45: $0.018 < \xi < 0.20$,
- Sector 56: $0.027 < \xi < 0.24$.

The distributions of the jet pruned mass after preselection are shown in Fig. 6.3, where both distributions are normalized to unity for shape comparison. A clear peak at mass values of about 80 GeV is observed for the signal, corresponding to the mass of the W boson decayed into a fat jet. The QCD multijets from background, on the contrary, produce a smooth spectrum. The τ_{21} distributions for leading and subleading jets are shown in Fig. 6.4. The background distributions tend to peak at τ_{21} values of about 0.65, reflecting the uniform structure of the jet without subjet splitting. The signal τ_{21} shape shows that the jets are very likely to have several subjets. To improve the statistical power of the subjettiness discriminator, following the approach in [96] and [97], the τ_{21}^{DDT} variable is introduced as a modification of τ_{21} decorrelated from the jet p_T and mass:

$$\tau_{21}^{DDT} = \tau_{21} - C \times \ln\left(\frac{m_j^2}{p_T \mu}\right), \tag{6.4}$$

where $\mu = 1$ GeV and the slope factor $C = -0.063$ is obtained from fits of the QCD background MC. The τ_{21}^{DDT} versus pruned mass distributions for leading and subleading jets are shown in Fig. 6.5. The W-tag requirement is defined as pruned mass in the range 68-88 GeV and $\tau_{21}^{DDT} < 0.65$.

As the dijet in signal events is produced in an exclusive reaction, the two jets are expected to be back to back and well balanced in p_T. This feature is used to additionally suppress background. The acoplanarity $a = 1 - \Delta\phi(jet1, jet2)/\pi$ vs p_T^{jet1}/p_T^{jet2} distribution for signal and background is shown in Fig. 6.6 for W-tagged jets passing the preselection. The requirements $a < 0.005$ and $p_T^{jet1}/p_T^{jet2} < 1.08$ are imposed in the analysis.

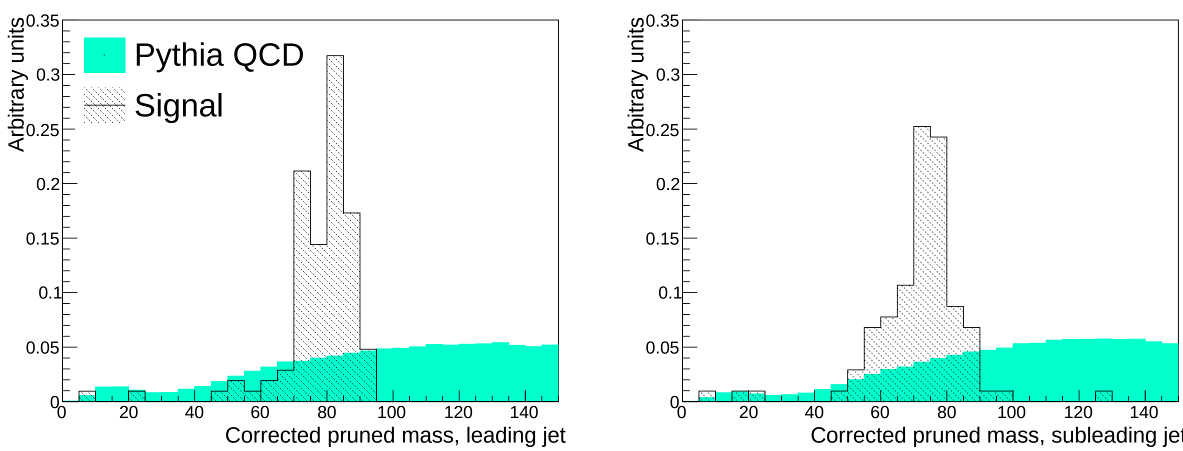

Figure 6.3: Pruned mass distributions for leading (left) and subleading (right) jet in signal and background samples after preselection. The area of each histogram is normalized to unity for shape comparison.

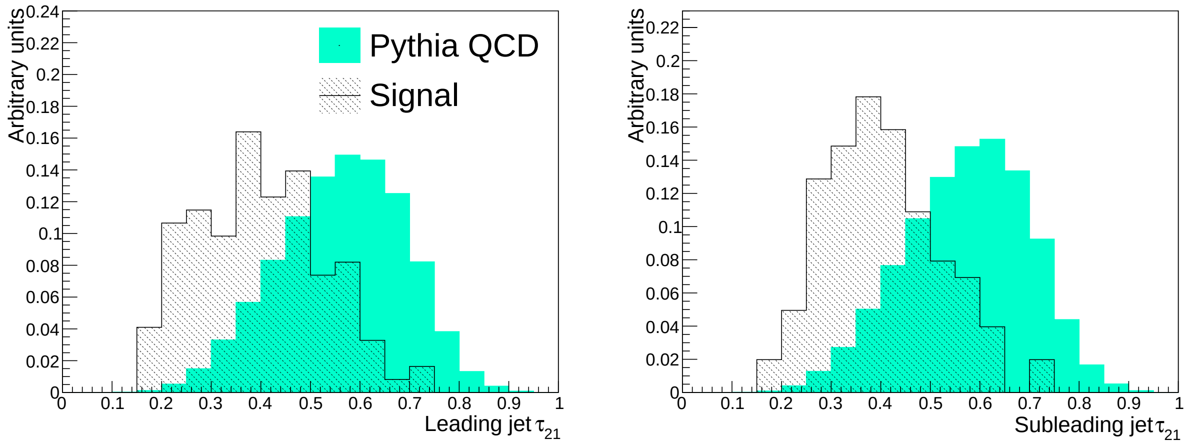

Figure 6.4: Distributions of τ^{21} for the leading (left) and subleading (right) jet in signal and background samples after preselection. The area of each histogram is normalized to unity for shape comparison.

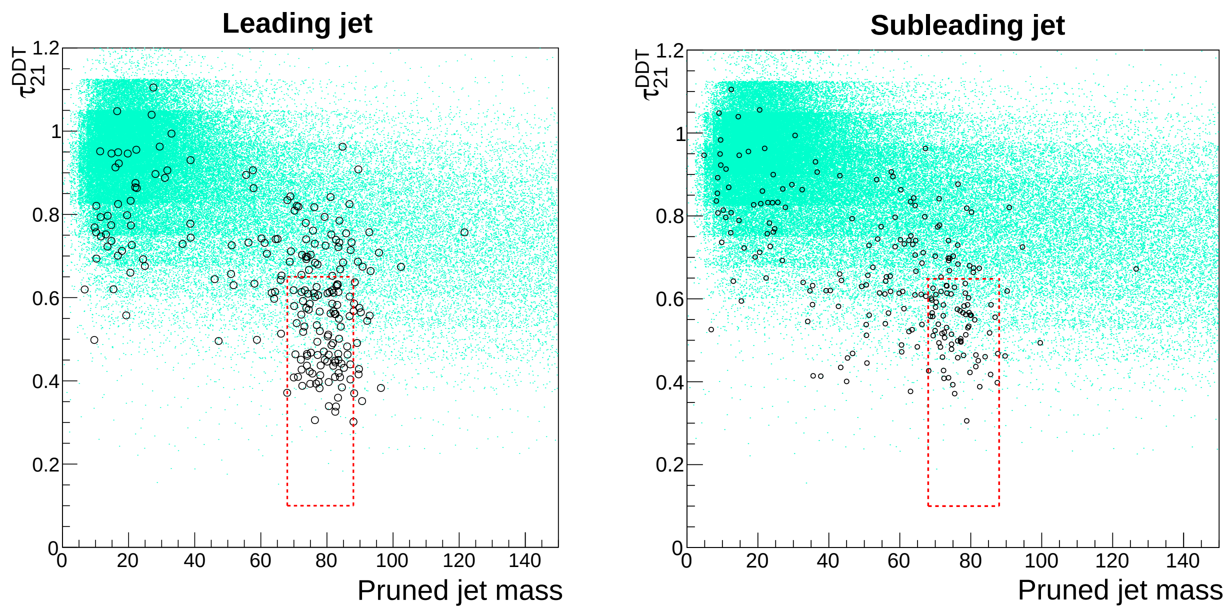

Figure 6.5: Distribution of τ_{21}^{DDT} versus pruned jet mass for the QCD background (green dots) and the anomalous WW signal in FPMC sample with $a_0^W = 2.5 \times 10^{-6}$ (black circles) at the preselection level. The left panel corresponds to the leading jet, the right to the subleading jet. The distributions are drawn as scatter plots with arbitrary normalization. The red lines indicate the cuts used for the signal selection.

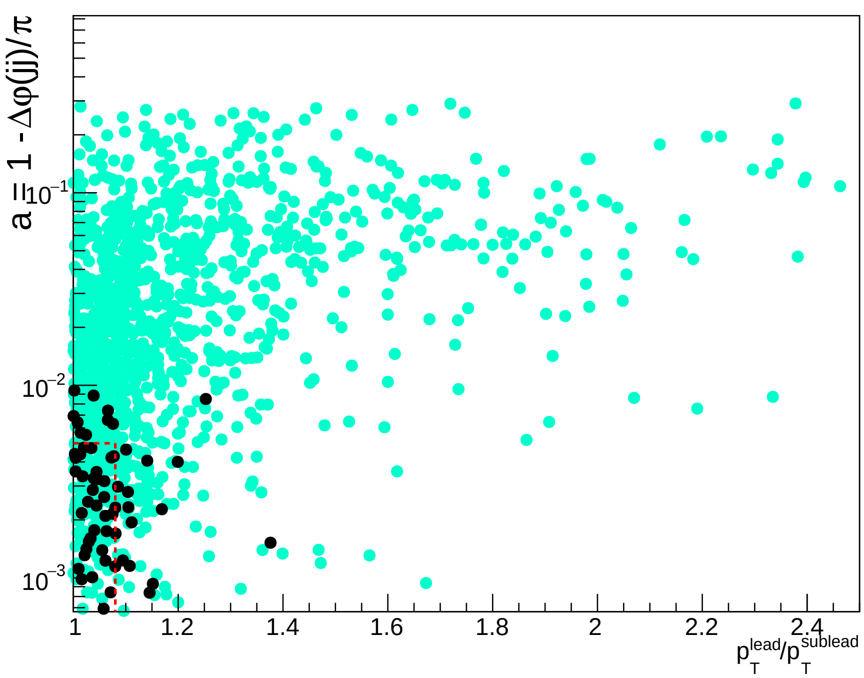

Figure 6.6: Distribution of acoplanarity versus the leading to subleading jet p_T ratio for the QCD background (green dots) and anomalous WW signal in the FPMC sample with $a_0^W = 2.5 \times 10^{-6}$ (black circles) for the W-tagged jets. The distributions are drawn as scatter plots not normalized to luminosity. The red lines indicate the cuts used for the signal selection.

6.5 Proton matching and resolution

As discussed earlier, the kinematics of the centrally produced system in exclusive reactions is defined by the momentum loss ξ of the scattered protons. The mass and rapidity of the central system X can be derived as:

$$M_X = \sqrt{s}\sqrt{\xi(p1)\xi(p2)}, \tag{6.5}$$

$$y_X = 0.5\ln(\xi(p1)/\xi(p2)). \tag{6.6}$$

These values of M_X and y_X can be compared with those obtained with the central CMS apparatus for matching purposes. The matching precision is constrained by the CMS and CT-PPS detector resolutions.

6.5.1 Resolution

The CMS dijet mass and rapidity resolution is derived by comparing generator level jets and the jets reconstructed after detector simulation. Both signal and QCD background samples are studied; the resolutions obtained are comparable. The larger value is chosen for the matching criteria, corresponding to a mass resolution of 3.4% and a y resolution of 5.4%. The CT-PPS mass and rapidity resolutions are estimated by comparing the generated and reconstructed protons in the signal sample. This results in a 7% resolution estimate in mass and 27% in rapidity.

Figure 6.7 shows the distributions of mass and rapidity as measured by the CMS central apparatus and CT–PPS.

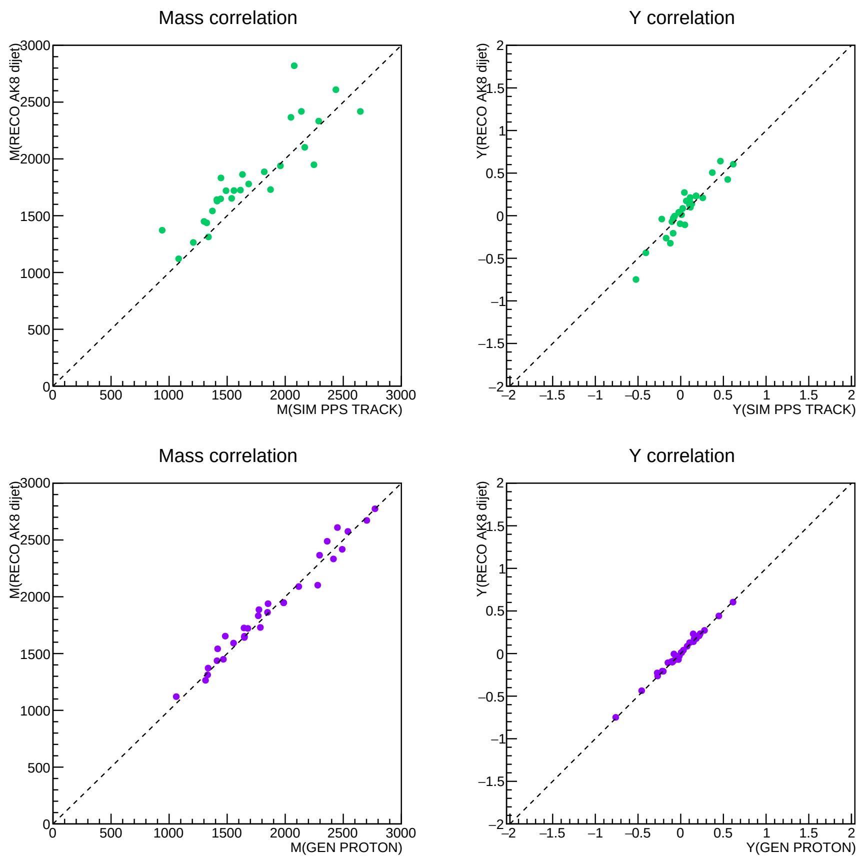

Figure 6.7: Mass (left) and rapidity (right) correlation plots for CMS and CT-PPS measurements. The top row shows mass and rapidity calculated from reconstructed jets in CMS and reconstructed protons in CT-PPS. The bottom row shows the same quantities, but with mass and rapidity derived from generated protons ξ.

6.5.2 Matching criteria

An event is considered matched if it contains at least one pair of protons matched to the dijets in mass and rapidity within twice the combined CMS and CT-PPS resolutions. This is referred to as "2σ" in the following.

6.6 Background estimate

Event mixing is used for the background estimate. In this approach the simulated background MC events (which do not contain any proton simulation) are randomly combined with pileup/beam halo protons measured in the 2017 data. The resulting events are then used to estimate the probability of random matching between the central system and the forward protons. The use of the measured ξ spectrum is preferred over simulation as the inclusive spectrum obtained in this way includes features of the data that are non-trivial to simulate, like beam background and detector noise.

6.6.1 Proton sample and mixing procedure

The inclusive proton ξ spectrum observed in 2017 without any CMS selection is used (Fig. 6.8). The corresponding spectrum in each arm is sampled randomly to evaluate ξ, which is then assigned to a MC background event.

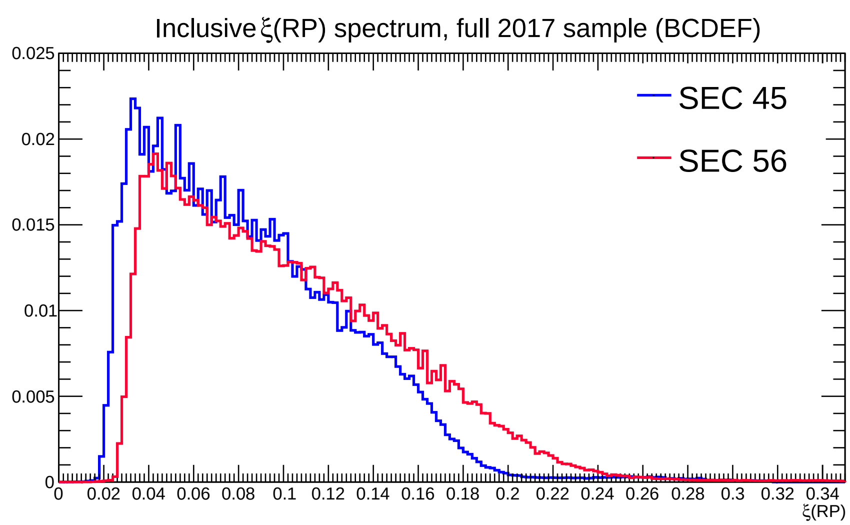

Figure 6.8: Inclusive proton ξ spectrum in the 2017 data obtained with CT-PPS, averaged over all crossing angles.

The background estimate is performed assuming an average pileup of about 50 and multitrack reconstruction in the pixel detectors. Several ξ values may thus be assigned to a given MC event.

The following mixing procedure is employed:

- Two random numbers (N_{trk}^{left} and N_{trk}^{right}) are generated using the pixel track multiplicity distribution for $\langle PU \rangle$=50 as probability density function (Fig. 6.9).
- Random ξ_{left} is generated N_{trk}^{left} times and all resulting values are associated to a given MC event. The same is done for the right arm N_{trk}^{right} times.
- At the analysis stage, the values M_X and y_X are calculated from the proton information for all possible combinations of the left and right arm ξ values.

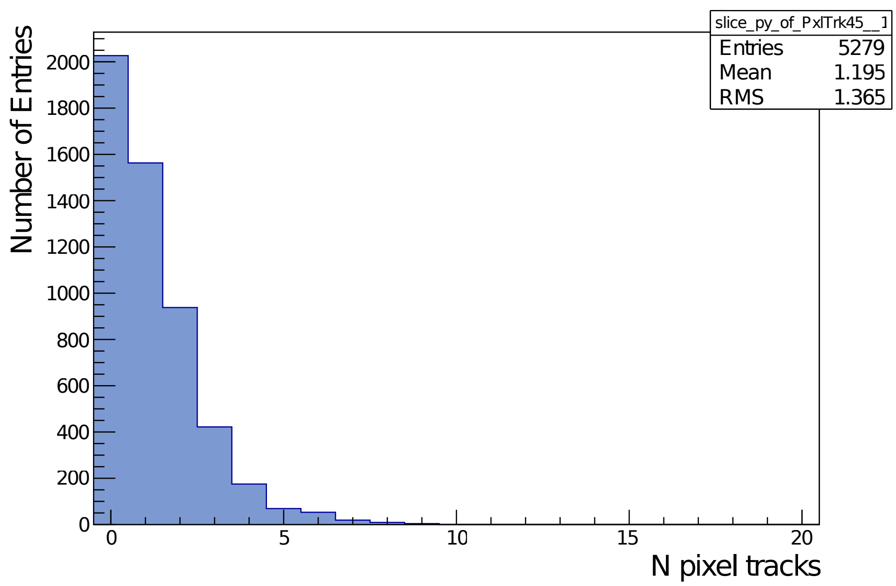

Figure 6.9: CT-PPS pixel track multiplicity distribution in the 2017 data during a period in which average pileup was about 50.

The mass-rapidity correlation plots after the proton mixing are shown in Fig. 6.10. The number of events passing the matching criteria (see Sec. 6.5) after the mixing is used as a background estimate.

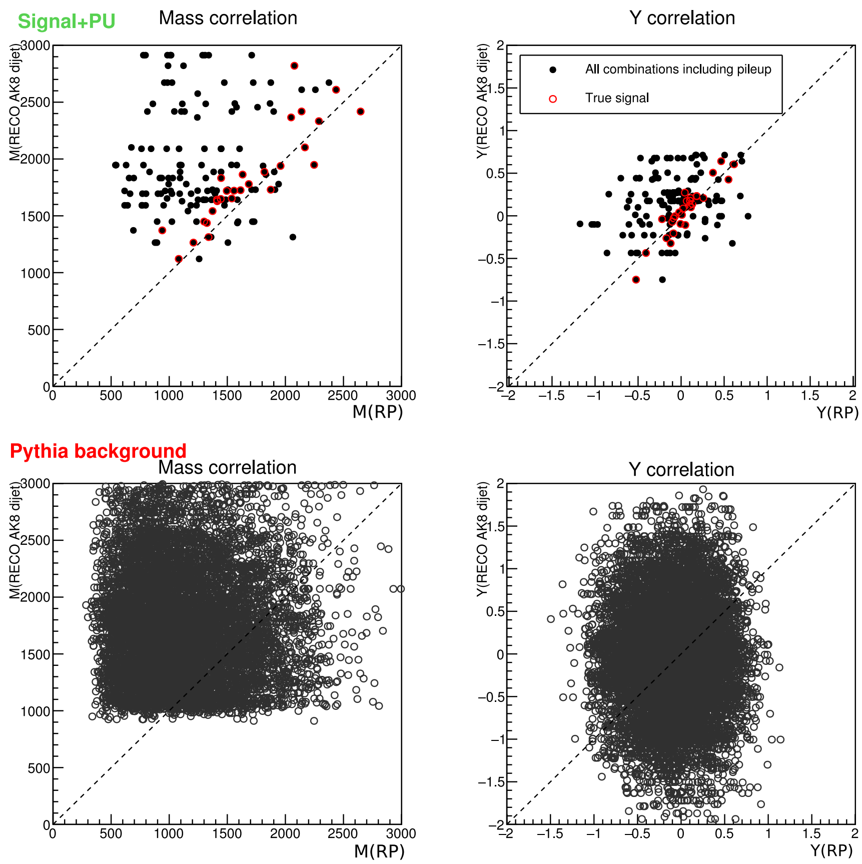

Figure 6.10: Mass (left) and rapidity (right) correlation plots for signal (top row) and QCD background (bottom row) samples after the event mixing.

6.7 Expected number of events in 300 fb^{-1}

The number of signal and background events matching within 2σ in both M and y is summarized in Tab. 6.2. The rapid increase of the yield is partially caused by the stronger boost of the W bosons for larger aQGC parameters, while for low a_0^W/Λ^2 values a significant fraction of the final state jets remains resolved. The signal to background fraction is predicted to exceed 1 for $a_0^W/\Lambda^2 = 2.5 \times 10^{-6}$ and 5.0×10^{-6} GeV^{-2}.

The expected number of Standard Model fully hadronic W^+W^- events that could be observed using the same selection is also estimated, based on a sample generated

Sample	Number of predicted events
QCD background	29 ±15
Signal, $a_0^W/\Lambda^2 = 0.5 \times 10^{-6}$ GeV^{-2}	2 ± 2
Signal, $a_0^W/\Lambda^2 = 1.0 \times 10^{-6}$ GeV^{-2}	17 ± 4
Signal, $a_0^W/\Lambda^2 = 2.5 \times 10^{-6}$ GeV^{-2}	80 ± 13
Signal, $a_0^W/\Lambda^2 = 5.0 \times 10^{-6}$ GeV^{-2}	360 ± 200

Table 6.2: Expected number of events after all signal selection cuts in 300 fb^{-1}.

with FPMC. The expected yield is less then 0.8 events in 300 fb^{-1}, before any requirement on the protons.

6.7.1 Expected limit on a_0^W/Λ^2

The expected limits on the signal yield are derived using the HiggsCombine tool [84] with the Profile Likelihood method, assuming that no signal is observed. Only statistical errors on the number of background MC events are considered. Figure 6.11 shows the expected upper limit along with 1 and 2-σ exclusion bands.

From the theory, the number of the signal events is expected to have a quadratic dependence on the anomalous parameter. A second degree polynomial fit of the MC-predicted numbers of observed events is thus performed to derive the projected limit on a_0^W/Λ^2 from that on the signal yield. The projected limit value thus obtained is $\sim 1.5 \times 10^{-6}$ GeV^{-2}.

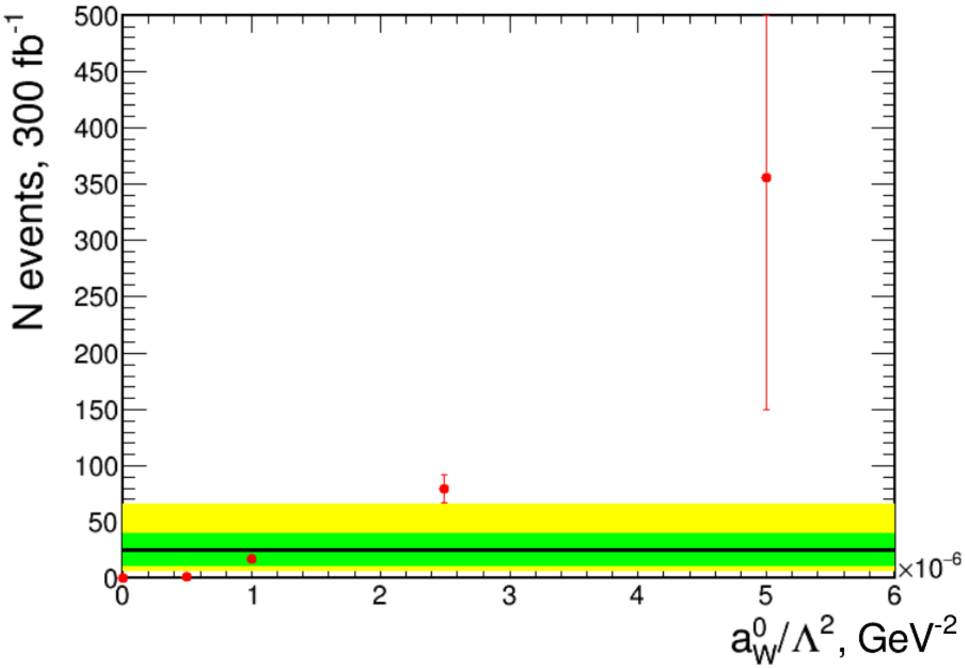

Figure 6.11: Red points are the predicted number of signal events as a function of the a_0^W/Λ^2 parameter. The statistical error bars are shown for the signal. The black line shows the expected upper limit on the signal yield, with the 1σ (green) and 2σ (yellow) exclusion bands, assuming that no signal is observed.

6.8 Conclusion

The present study demonstrates the feasibility of measuring exclusive W^+W^- production in the fully hadronic channel in Run 3 with CT-PPS. It is expected that an exclusion limit of about 1.5 $\times 10^{-6}$ GeV^{-2} on a_0^W/Λ^2 parameter can be achieved, several orders of magnitude better than the currently available estimates [98].

As discussed in Sec. 6.1, more channels are available, which would further enhance the significance of the measurement and potentially allow to improve the sensitivity well below 10^{-6} GeV^{-2}. Another significant improvement can be achieved with the help of precise timing measurements using the CT-PPS double diamond detectors.

While W^+W^- production was the primary focus of the present study, the analysis can be easily extended to include the ZZ and the two Higgs boson channels.

Chapter 7

Summary and outlook

Over the years 2015-2018, CT-PPS has evolved from a freshly assembled prototype to a fully integrated and functional extension of the CMS experiment. Several important milestones were achieved along the way. First of all, CT–PPS has shown that the operation of the near-beam spectrometer in standard high-luminosity conditions is technically possible. Beyond this, about 100 fb^{-1} of data were collected in the period 2016-2018. The analysis of the first part of this dataset is the main focus of the present thesis. The analysis was initially carried out with the aim of validating all aspects of reconstruction, calibration and synchronization of CT–PPS with CMS; indeed the correlation observed between the CMS and CT–PPS measurements of (semi)exclusive dilepton production proves that the spectrometer works as expected. The quality of the early 2016 data made it also possible to obtain a physics result: the first observation of photon-photon collisions at the electroweak scale. This was published as a CMS and TOTEM paper in [25]. The analysis was repeated on the 2017 data, collected with an upgraded spectrometer in which 3D pixel sensors were used for tracking instead of the TOTEM Si strip detectors. The results indicate that the new tracker works according to specifications, with excellent multitrack reconstruction capabilities. The dilepton analysis procedure is now well established and can be used for the validation of the future CT-PPS datasets.

The results obtained with the 2016-2017 data pave the way for future analyses using forward protons. Among these, the search for anomalous quartic gauge couplings. The feasibility study carried out as part of this thesis for the fully hadronic W^+W^- decay channel suggests that it may be possible to improve the current limits by several orders of magnitude. This analysis has the potential to make important contributions to the search of physics beyond the Standard Model.

A final remark is in order. The technical and scientific success of CT-PPS has been made possible by a somewhat unusual event in high-energy physics: two independent collaborations, CMS and TOTEM, have joined forces to pursue a common physics interest. CMS and TOTEM have existed for decades as separate experiments, with different goals, organization, and traditions. It was not a priori obvious that this joint venture would work. It however did, and in 2018, a Memorandum of Understanding between CERN, CMS and TOTEM was signed stating that all TOTEM members can become members of CMS if they so desire, and will remain CMS members after the TOTEM physics program is over. This is a tribute to the hard work of many people, and to their technical, scientific, as well as social competence.

Bibliography

[1] U. Amaldi. Small-angle physics at the intersecting storage rings forty years later. In *Proceedings, 40th Anniversary of the First Proton-Proton Collisions in the CERN Intersecting Storage Rings (ISR): Geneva, Switzerland, January 18, 2011*, 2012.

[2] L. Baksay et al. Measurement of the Proton Proton Total Cross-Section and Small Angle Elastic Scattering at ISR Energies. *Nucl. Phys.*, B141:1–28, 1978. [Erratum: Nucl. Phys.B148,538(1979)].

[3] A. Brandt et al. The small angle spectrometer of experiment UA8 at the SpS collider. *Nucl. Instrum. Meth.*, A327:412–426, 1993.

[4] The ZEUS Collaboration. The ZEUS Leading Proton Spectrometer and its use in the measurement of elastic $\rho 0$ photoproduction at HERA. *Zeitschrift für Physik C Particles and Fields*, 73(2):253–268, Jun 1997.

[5] P. Van Esch et al. The H1 forward proton spectrometer at HERA. *Nucl. Instrum. Meth.*, A446:409–425, 2000.

[6] A. Santoro. Forward Proton Detector on D0 experiment. *Braz. J. Phys.*, 30(2):362–369, 2000.

[7] M. Gallinaro. CDF forward detectors and diffractive structure functions at the Fermilab Tevatron. In *Proceedings, 9th Hadron Physics and 7th Relativistic Aspects of Nuclear Physics (HADRON-RANP 2004): A Joint Meeting on QCD and QGP: Rio de Janeiro, Brazil, March 28-April 3, 2004*, 2004.

[8] S. Bultmann et al. The PP2PP experiment at RHIC: Silicon detectors installed in Roman Pots for forward proton detection close to the beam. *Nucl. Instrum. Meth.*, A535:415–420, 2004.

[9] CMS and TOTEM Collaborations. CMS-TOTEM Precision Proton Spectrometer. CERN-LHCC-2014-021. TOTEM-TDR-003. CMS-TDR-13, Sep 2014.

[10] L. Adamczyk, E. Bana, A. Brandt, M. Bruschi, S. Grinstein, J. Lange, M. Rijssenbeek, P. Sicho, R. Staszewski, T. Sykora, M. Trzebiski, J. Chwastowski, and K. Korcyl. Technical Design Report for the ATLAS Forward Proton Detector. Technical Report CERN-LHCC-2015-009. ATLAS-TDR-024, May 2015.

[11] G. Belanger, F. Boudjema, Y. Kurihara, D. Perret-Gallix, and A. Semenov. Bosonic quartic couplings at LEP-2. *Eur. Phys. J.*, C13:283–293, 2000.

[12] ALEPH Collaboration. Constraints on anomalous QGCs in e^+e^- interactions from 183 to 209 GeV. *Physics Letters B*, 602(1):31 – 40, 2004.

[13] OPAL Collaboration. Constraints on anomalous quartic gauge boson couplings from $\nu\bar{\nu}\gamma\gamma$ and $q\bar{q}\gamma\gamma$ events at CERN LEP2. *Phys. Rev. D*, 70:032005, Aug 2004.

[14] OPAL Collaboration. A Study of $W^+W^-\gamma$ events at LEP. *Phys. Lett.*, B580:17–36, 2004.

[15] OPAL Collaboration. Measurement of the $W^+W^-\gamma$ cross-section and first direct limits on anomalous electroweak quartic gauge couplings. *Phys. Lett.*, B471:293–307, 1999.

[16] L3 Collaboration. The $e^+e^- \to Z\gamma\gamma \to q\bar{q}\gamma\gamma$ reaction at LEP and constraints on anomalous quartic gauge boson couplings. *Phys. Lett.*, B540:43–51, 2002.

[17] L3 Collaboration. Study of the $W^+W^-\gamma$ process and limits on anomalous quartic gauge boson couplings at LEP. *Physics Letters B*, 527(1):29 – 38, 2002.

[18] DELPHI Collaboration. Measurement of the $e^+e^- \to W^+W^-\gamma$ Cross-section and Limits on Anomalous Quartic Gauge Couplings with DELPHI. *Eur. Phys. J.*, C31:139–147, 2003.

[19] D0 Collaboration. Search for anomalous quartic $WW\gamma\gamma$ couplings in dielectron and missing energy final states in $p\bar{p}$ collisions at $\sqrt{s} = 1.96$ TeV. *Phys. Rev.*, D88:012005, 2013.

[20] K. Piotrzkowski. Tagging two photon production at the CERN LHC. *Phys. Rev.*, D63:071502, 2001.

[21] T. Pierzchala and K. Piotrzkowski. Sensitivity to anomalous quartic gauge couplings in photon-photon interactions at the LHC. *Nucl. Phys. Proc. Suppl.*, 179-180:257–264, 2008.

[22] R. S. Gupta. Probing Quartic Neutral Gauge Boson Couplings using diffractive photon fusion at the LHC. *Phys. Rev.*, D85:014006, 2012.

[23] D. d'Enterria, M. Klasen, and K. Piotrzkowski, editors. *High-energy photon collisions at the LHC. Proceedings, International Workshop, Photon-LHC-2008, Geneva, Switzerland, 2008*, volume 179-180, 2008.

[24] V. A. Khoze, M. G. Ryskin, and W. J. Stirling. On radiative QCD backgrounds to exclusive H $\to b\bar{b}$ production at the LHC and a photon collider. *Eur. Phys. J.*, C48:477–488, 2006.

[25] CMS and TOTEM Collaborations. Observation of proton-tagged, central (semi)exclusive production of high-mass lepton pairs in pp collisions at 13 TeV with the CMS-TOTEM precision proton spectrometer. *JHEP*, 07:153, 2018.

[26] CMS Collaboration. The CMS experiment at the CERN LHC. *JINST*, 3:S08004. 361 p, 2008. Also published by CERN Geneva in 2010.

[27] M. Deile, R. Bruce, A. Mereghetti, D. Mirarchi, S. Redaelli, B. Salvachua, B. Salvant, and G. Valentino. Roman Pot Insertions in High-Intensity Beams for the CT–PPS Project at LHC. (CERN-ACC-2016-251):TUPMW021. 4 p, 2016.

[28] P. Aspell, V. Avati, W. Bialas, J. Kaspar, J. Kopal, J. Petäjäjärvi, E. Radicioni, J. Rouet, W. Snoeys, and P. Vichoudis. The VFAT Production Test Platform for the TOTEM Experiment. 2008.

[29] F. Ravera. The CT–PPS tracking system with 3D pixel detectors. *Journal of Instrumentation*, 11:C11027, November 2016.

[30] `http://www.imb-cnm.csic.es/index.php/en/`.

[31] TOTEM Collaboration. Diamond detectors for the TOTEM timing upgrade. *Journal of Instrumentation*, 12(03):P03007, 2017.

[32] R Arcidiacono. A new timing detector for the CT–PPS project. *Nuclear Instruments and Methods in Physics Research Section A: Accelerators, Spectrometers, Detectors and Associated Equipment*, 845, 05 2016.

[33] N. Cartiglia et al. Beam test results of a 16 ps timing system based on ultra-fast silicon detectors. *Nucl. Instrum. Meth.*, A850:83–88, 2017.

[34] TOTEM Collaboration. The TOTEM electronics system. *Topical Workshop on Electronics for Particle Physics*, pages 205–210, 01 2007.

[35] G. Antchev, T. Kiss, and W. Snoeys. The TOTEM roman pot motherboard. In *Electronics for particle physics. Proceedings, Topical Workshop, TWEPP-08, Naxos, Greece, 15-19 September 2008*, pages 446–449, 2008.

[36] P. Aspell, G. Anelli, P. Chalmet, J. Kaplon, K. Kloukinas, H. Mugnier, and W. Snoeys. VFAT2: A front-end "system on chip" providing fast trigger information and digitized data storage for the charge sensitive readout of multi-channel silicon and gas particle detectors. In *2008 IEEE Nuclear Science Symposium Conference Record*, pages 1489–1494, Oct 2008.

[37] `http://www.ti.com/lit/an/snla165/snla165.pdf`.

[38] J. Troska, S. Detraz, S. S. El. Nasr-Storey, P. Stejskal, C. Sigaud, C. Soos, and F. Vasey. Prototype pixel optohybrid for the CMS phase 1 upgraded pixel detector. *Journal of Instrumentation*, 7(01):C01113, 2012.

[39] F. Anghinolfi, P. Jarron, A.N. Martemiyanov, E. Usenko, H. Wenninger, M.C.S. Williams, and A. Zichichi. NINO: an ultra-fast and low-power front-end amplifier/discriminator ASIC designed for the multigap resistive plate chamber. *Nuclear Instruments and Methods in Physics Research Section A: Accelerators, Spectrometers, Detectors and Associated Equipment*, 533(1):183 – 187, 2004. Proceedings of the Seventh International Workshop on Resistive Plate Chambers and Related Detectors.

[40] J. Kaspar. Alignment of CT–PPS detectors in 2016, before TS2. CERN-TOTEM-NOTE 2017-001, 2017.

[41] TOTEM Collaboration. Performance of the TOTEM detectors at the LHC. *Int. J. Mod. Phys. A*, 28:1330046, 2013.

[42] F. Nemes. LHC optics determination with proton tracks measured in the CT–PPS detectors in 2016, before TS2. CERN-TOTEM-NOTE CERN-TOTEM-NOTE-2017-002, 2017.

[43] H. Grote and F. Schmidt. MAD-X: An upgrade from MAD8. In *2003 Particle Accelerator Conference*, Portland, Oregon, May 2003. econf C03-05-12.

[44] TOTEM Collaboration. LHC optics measurement with proton tracks detected by the Roman pots of the TOTEM experiment. *New J. Phys.*, 16:103041, 2014.

[45] J. Kaspar. *Elastic scattering at the LHC*. PhD thesis, Prague, Inst. Phys., 2011. CERN-THESIS-2011-214.

[46] J. de Favereau de Jeneret, V. Lemaitre, Y. Liu, S. Ovyn, T. Pierzchala, K. Piotrzkowski, X. Rouby, N. Schul, and M. Vander Donckt. High energy photon interactions at the LHC. 2009.

[47] CMS Collaboration. exclusive two-photon production of $\mathrm{W^+W^-}$ in pp collisions at $\sqrt{s} = 7$ TeV and constraints on anomalous quartic gauge couplings. *JHEP*, 07:116, 2013.

[48] CMS Collaboration. Evidence for exclusive $\gamma\gamma \to W^+W^-$ production and constraints on anomalous quartic gauge couplings in pp collisions at $\sqrt{s} = 7$ and 8 TeV. *JHEP*, 08:119, 2016.

[49] ATLAS Collaboration. Measurement of exclusive $\gamma\gamma \to W^+W^-$ production and search for exclusive Higgs boson production in pp collisions at $\sqrt{s} = 8$ TeV using the ATLAS detector. *Phys. Rev. D*, 94:032011, 2016.

[50] S. Atag, S. C. Inan, and I. Sahin. Extra dimensions in photon-induced two lepton final states at the CERN-LHC. *Phys. Rev. D*, 80:075009, 2009.

[51] I. Sahin and S. C. Inan. Probe of unparticles at the LHC in exclusive two lepton and two photon production via photon-photon fusion. *JHEP*, 09:069, 2009.

[52] S. C. Inan. Exclusive excited leptons search in two lepton final states at the CERN-LHC. *Phys. Rev. D*, 81:115002, 2010.

[53] CDF Collaboration. Observation of exclusive electron-positron production in hadron-hadron collisions. *Phys. Rev. Lett.*, 98:112001, 2007.

[54] CDF Collaboration. Search for exclusive Z boson production and observation of high mass $p\bar{p} \to \gamma\gamma \to p + \ell\ell + \bar{p}$ events in $p\bar{p}$ collisions at $\sqrt{s} = 1.96$ TeV. *Phys. Rev. Lett.*, 102:222002, 2009.

[55] CMS Collaboration. Exclusive photon-photon production of muon pairs in proton-proton collisions at $\sqrt{s} = 7$ TeV. *JHEP*, 01:052, 2012.

[56] CMS Collaboration. Search for exclusive or semi-exclusive photon pair production and observation of exclusive and semi-exclusive electron pair production in pp collisions at $\sqrt{s} = 7$ TeV. *JHEP*, 11:080, 2012.

[57] ATLAS Collaboration. Measurement of exclusive $\gamma\gamma \to \ell^+\ell^-$ production in proton-proton collisions at $\sqrt{s} = 7$ TeV with the ATLAS detector. *Phys. Lett. B*, 749:242, 2015.

[58] ATLAS Collaboration. Measurement of the exclusive $\gamma\gamma \to \mu^+\mu^-$ process in proton-proton collisions at $\sqrt{s} = 13$ TeV with the ATLAS detector. *Phys. Lett. B*, 777:303, 2018.

[59] G. Ruggiero, V. Avati, G. Antchev, M. Deile, K. Eggert, V. Eremin, J. Kaspar, H. Niewiadomski, J. Petjjrvi, E. Radicioni, F. Ravotti, E. Radermacher, W. Snoeys, W. Spearman, and J. Wu. Characteristics of edgeless silicon detectors for the Roman pots of the TOTEM experiment at the LHC. *Nucl. Instrum. Meth. A*, 604:242, 2009.

[60] N. Metropolis, A. W. Rosenbluth, M. N. Rosenbluth, A. H. Teller, and E. Teller. Equation of state calculations by fast computing machines. *The Journal of Chemical Physics*, 21(6):1087–1092, 1953.

[61] W. K. Hastings. Monte carlo sampling methods using markov chains and their applications. *Biometrika*, 57(1):97–109, 1970.

[62] T. Sjöstrand, S. Mrenna, and P. Z. Skands. A brief introduction to PYTHIA 8.1. *Comput. Phys. Commun.*, 178:852, 2008.

[63] S. Agostinelli et al. GEANT4 — a simulation toolkit. *Nucl. Instrum. Meth. A*, 506:250, 2003.

[64] J. A. M. Vermaseren. Two photon processes at very high energies. *Nucl. Phys. B*, 229:347, 1983.

[65] S. P. Baranov, O. Dünger, H. Shooshtari, and J. A. M. Vermaseren. LPAIR: A generator for lepton pair production. In *Workshop on Physics at HERA Hamburg, Germany, October 29-30, 1991*, page 1478, 1991.

[66] T. Sjöstrand, L. Lonnblad, and S. Mrenna. PYTHIA 6.2: Physics and manual. 2001.

[67] G. Gil da Silveira, L. Forthomme, K. Piotrzkowski, W. Schfer, and A. Szczurek. Central $\mu^+\mu^-$ production via photon-photon fusion in proton-proton collisions with proton dissociation. *JHEP*, 02:159, 2015.

[68] J. Alwall, R. Frederix, S. Frixione, V. Hirschi, F. Maltoni, O. Mattelaer, H. S. Shao, T. Stelzer, P. Torrielli, and M. Zaro. The automated computation of tree-level and next-to-leading order differential cross sections, and their matching to parton shower simulations. *JHEP*, 07:079, 2014.

[69] R. Frederix and S. Frixione. Merging meets matching in MC@NLO. *JHEP*, 12:061, 2012.

[70] CMS Collaboration. Event generator tunes obtained from underlying event and multiparton scattering measurements. *Eur. Phys. J. C*, 76:155, 2016.

[71] Y. Li and F. Petriello. Combining QCD and electroweak corrections to dilepton production in FEWZ. *Phys. Rev. D*, 86:094034, 2012.

[72] J. D. Bjorken. A full-acceptance detector for SSC physics at low and intermediate mass scales: an expression of interest to the SSC. *International Journal of Modern Physics A*, 07(18):4189–4257, 1992.

[73] L. A. Harland-Lang, V. A. Khoze, and M. G. Ryskin. The photon PDF in events with rapidity gaps. *Eur. Phys. J. C*, 76:255, 2016.

[74] CMS Collaboration. The CMS trigger system. *JINST*, 12:P01020, 2017.

[75] O. Kortner. Muon Identification at ATLAS and CMS. 2007.

[76] CMS Collaboration. Performance of electron reconstruction and selection with the CMS detector in proton-proton collisions at $\sqrt{s} = 8$ TeV. *JINST*, 10:P06005, 2015.

[77] T. Speer, K. Prokofiev, R. Frhwirth, W. Waltenberger, and P. Vanlaer. Vertex Fitting in the CMS Tracker. CMS-NOTE-2006-032, CERN, Geneva, Feb 2006.

[78] CMS Collaboration. Performance of CMS muon reconstruction in pp collision events at $\sqrt{s} = 7$ TeV. *JINST*, 7:P10002, 2012.

[79] CDF Collaboration. Observation of exclusive charmonium production and $\gamma + \gamma$ to $\mu^+\mu^-$ in $p\bar{p}$ collisions at $\sqrt{s} = 1.96$ TeV. *Phys. Rev. Lett.*, 102:242001, 2009.

[80] M. Dyndal and L. Schoeffel. The role of finite-size effects on the spectrum of equivalent photons in proton-proton collisions at the LHC. *Phys. Lett. B*, 741:66, 2015.

[81] L. A. Harland-Lang, V. A. Khoze, and M. G. Ryskin. Exclusive physics at the LHC with SuperChic 2. *Eur. Phys. J. C*, 76:9, 2016.

[82] P. Lebiedowicz and A. Szczurek. Exclusive production of heavy charged Higgs boson pairs in the $pp \to ppH^+H^-$ reaction at the LHC and a future circular collider. *Phys. Rev. D*, 91:095008, 2015.

[83] CMS Collaboration. CMS luminosity measurements for the 2016 data-taking period. CMS Physics Analysis Summary CMS-PAS-LUM-17-001, 2017.

[84] https://cms-hcomb.gitbooks.io/combine/content/.

[85] F. Garwood. Fiducial limits for the poisson distribution. *Biometrika*, 28(3-4):437–442, 1936.

[86] E. Chapon, C. Royon, and O. Kepka. Anomalous quartic $WW\gamma\gamma$, $ZZ\gamma\gamma$, and trilinear $WW\gamma$ couplings in two-photon processes at high luminosity at the LHC. *Phys. Rev. D*, 81:074003, Apr 2010.

[87] ATLAS Collaboration. Measurement of exclusive $\gamma\gamma \to W^+W^-$ production and search for exclusive higgs boson production in pp collisions at $\sqrt{s} = 8$ TeV using the atlas detector. *Phys. Rev. D*, 94:032011, Aug 2016.

[88] CMS Collaboration. Search for massive resonances decaying into WW, WZ, ZZ, qW, and qZ with dijet final states at $\sqrt{s} = 13$ TeV. *Phys. Rev.*, D97(7):072006, 2018.

[89] M. Boonekamp, A. Dechambre, V. Juranek, O. Kepka, M. Rangel, C. Royon, and R. Staszewski. FPMC: A Generator for forward physics, 2011.

[90] E. Boos, V. Bunichev, M. Dubinin, L. Dudko, V. Ilyin, A. Kryukov, V. Edneral, V. Savrin, A. Semenov, and A. Sherstnev. CompHEP 4.4: Automatic computations from Lagrangians to events. *Nucl. Instrum. Meth.*, A534:250–259, 2004.

[91] G. Bélanger and F. Boudjema. $\gamma\gamma \to \mathrm{W^+W^-}$ and $\gamma\gamma \to \mathrm{ZZ}$ as tests of novel quartic couplings. *Physics Letters B*, 288(1):210 – 220, 1992.

[92] M. Cacciari, G. P. Salam, and G. Soyez. The anti-k_t jet clustering algorithm. *JHEP*, 04:063, 2008.

[93] M. Cacciari, G. P. Salam, and G. Soyez. FastJet User Manual. *Eur. Phys. J.*, C72:1896, 2012.

[94] CMS Collaboration. Identification techniques for highly boosted W bosons that decay into hadrons. *JHEP*, 12:017, 2014.

[95] J. Thaler and K. Van Tilburg. Identifying Boosted Objects with N-subjettiness. *JHEP*, 03:015, 2011.

[96] J. Dolen, P. Harris, S. Marzani, S. Rappoccio, and N. Tran. Thinking outside the ROCs: Designing Decorrelated Taggers (DDT) for jet substructure. *JHEP*, 05:156, 2016.

[97] CMS Collaboration. Search for WW in semileptonic final states: low mass extension. CMS-PAS-B2G-16-004, CERN, Geneva, 2016.

[98] https://twiki.cern.ch/twiki/bin/view/CMSPublic/PhysicsResultsSMPaTGC.